Domain Decomposition Based Hybrid Methods for Solving Real-Life Electromagnetic Scattering and Radiation Problems

by
Onur Bakir

A dissertation submitted in partial fulfillment
of the requirements for the degree of
Doctor of Philosophy
(Electrical Engineering)
in The University of Michigan
2012

Doctoral Committee:

Professor Eric Michielssen, Chair
Professor Christopher S. Ruf
Professor Kamal Sarabandi
Assistant Professor Mona Jarrahi

to my family and friends

ACKNOWLEDGEMENTS

I would like to thank my advisor, Professor Eric Michielssen for giving me the opportunity to work with him and supporting my studies at the University of Michigan. I would like to thank to the members of my dissertation committee Kamal Sarabandi, Mona Jarrahi, and Christopher Ruf for their time reading this dissertation and their valuable comments. Also, I would like to mention Professors Fawwaz Ulaby and Anthony Grbic who were in my preliminary exam.

I would like to express my gratitude to Professor Vakur Ertürk who was my advisor during my graduate studies at Bilkent University. His inspiration, motivation, and mentorship helped me to get this far.

I would like to thank to my colleagues Felipe Valdes and Francesco Andriulli at Michielssen research group. I would like to extend special thanks to Hakan Bağcı who was a post-doc in our group, now a Professor at KAUST for his help, knowledge, and friendship in the first years of my studies. I would like to thank to all my colleagues in the Radiation Laboratory (Radlab), University of Michigan. I would like to mention some of them here (in alphabetical order) Michael Benson, Mariko Burgin, Fikadu Dagefu, Xueyang Duan, Danial Ehyaie, Adel Elsherbini, Yuriy Goykhman, Yohan Kim, Victor Lee, Pelumi Osaba, Amit Patel, Carl Pfeiffer, Scott Rudolph, Alireza Tabatabaeenejad,

Mehrnoosh Vahidpour, and Jackie Vitaz not only for being colleagues but also good friends.

During these 5.5 years in Ann Arbor I had the chance to meet a lot of great people, made wonderful friends. I would like to thank all of them for their friendship and support during these years. I would like to mention some of them here (in alphabetical order): Seçkin Akgül, Mohammad Alm, Hanife Broome, George Broome, Haydee Izaguirre, Özlem Küçüloğlu, Sandy Lahoud, Civan Orakçılar, Amit Patel, Aly Tou, and Öyküm Yeşildere.

Next, I would like to thank to Oğuz Atan, Özer Aydemir, Alırıza Bozbulut, Ali Buğdaycı, Kamer Kaya, Oğuz Kurt, Mustafa Sakalsız, Niyazi Şenlik, Servet Şenlik, and Tansu Şenyurt, who I met at college (Bilkent University) and become friends since, for their friendship and support.

Finally, I would like to thank to my family for their love and support in all these years.

TABLE OF CONTENTS

LIST OF FIGURES

LIST OF TABLES

CHAPTER 1
Introduction

1.1 Motivation

Many engineering problems, including the analysis of radar scattering from air- and spacecraft, the design of antennas and microwave circuits, the characterization of electromagnetic (EM) interactions with biological tissue, and the study of electromagnetic compatibility and interference phenomena, call for the analysis of time-harmonic electromagnetic interactions with electrically large and geometrically intricate structures. In each problem, one seeks the solution of Maxwell's equations for the given radiation and scattering system. Since the exact analytical solutions to Maxwell's equations are available only for canonical geometries such as spheres, spheroids, and infinite cylinders, computational electromagnetics (CEM), encouraged by the advent of powerful computers, became the most important approach to solve real-life time-harmonic EM scattering and radiation problems. Various numerical methods are developed for the formulation and solution of these problems [1-10]. However, problems with increasing complexity and the trend towards using higher operating frequencies encourage the development of new methods in CEM. Each of these existing CEM methods has their strengths and weaknesses when applied to certain type of problems. Hybrid techniques combine two or more methods to retain their strengths and overcome their weaknesses, which yields greater flexibility in modeling complex structures.

The following discussion briefly overviews two of the major methods in CEM: integral equation (IE) and finite element (FE) methods. It is merely indented to provide a background for a hybrid method introduced later in this thesis. For a more complete survey on CEM methods, the reader is referred to [5, 7, 11] and the references there in. IE methods formulate the EM scattering and radiation problem as integral equations in terms of unknown equivalent surface or volumetric current densities according to equivalence theorem [12]. IEs can be classified into two sub-groups based on this distinction: surface (S) and volume (V) IEs. VIE methods are suitable for modeling arbitrarily inhomogeneous dielectric structures, whereas SIE methods can only be applied to piecewise homogeneous dielectric structures (possibly including perfect electrically conducting (PEC) objects or surfaces) [1-6]. To numerically solve SIEs and VIEs, surfaces and volumes are discretized using 2D (e.g. flat or curvilinear triangular elements) and 3D (e.g. hexahedral or tetrahedral elements) elements, respectively. Then, the unknown currents are expanded in terms of linearly independent basis functions supported on these elements. Using the popular method of moments (MOM) procedure [1], IEs are converted into linear systems of equations of order N, where N is the number of basis functions used to expand surface (for SIEs) or volume (for VIEs) currents. The classical (i.e. nonaccelerated) iterative solution of adequately preconditioned MOM systems requires $O(N^2)$ memory and $O(N^2)$ CPU resources, respectively. During the past decade, several accelerators that reduce these memory and CPU requirements have been proposed; examples include, but are not limited to, the multi-level fast multipole algorithm (MLFMA) [13, 14], the conjugate gradient fast Fourier transform [15] and pre-corrected fast Fourier transform [16] techniques, and the adaptive integral method (AIM) [17-19]; the latter two are closely related. In this thesis a memory efficient extension of classical AIM, named fast Gaussian gridding (FGG) – AIM, is developed for SIEs [20] and VIEs. This efficiency is achieved by incorporating

fast Gaussian gridding (FGG) [21, 22], a recently developed scheme for computing nonuniform FFTs (NUFFTs) with low memory requirements, into the AIM framework.

In the last decade, SIE solvers that use high order representations of the surface and/or current density become increasingly popular due to their high fidelity modeling capabilities [23]. They aim to reduce two major sources of errors in the numerical solution of SIEs, namely, errors due to finite approximation of the surface and current density. For a given accuracy high-order solvers are computationally more efficient then their low-order counterparts, since they require less number of basis functions to expand the current density to reach the same accuracy [14, 24]. However, these methods are usually not generalized for composite structures with arbitrary metal-dielectric junctions. Donepudi et al. [24] presented a high order, MLFMA accelerated SIE solver for composite dielectric and PEC structure; unfortunately their method does not consider open PEC surfaces and the treatment of the junction problem is not discussed. In [25] Kim et al. presented a high order, AIM accelerated volume and combined volume-surface IE solver for the same problem. However, in their method metallic and dielectric objects are assumed to be removed from each other. In this thesis a high order, AIM-FGG accelerated SIE solver is developed for general composite dielectric-PEC structures with arbitrary surface junctions [26].

FE methods formulate the EM radiation and scattering problem as partial differential equations (PDEs) derived by starting directly from the Maxwell's equations. These equations are solved by discretizing the solution domain into smaller elements, and expanding the unknown field quantities on these elements. Their solution leads to sparse matrix systems which can be solved efficiently [8, 10]. FE methods have the ability to model arbitrarily inhomogeneous composite dielectric-PEC structures. However, they require artificial truncation of the otherwise infinite solution domain by enforcing approximate radiation conditions at the truncation boundary, which leads to numerical

error accumulation. A popular alternative is to combine FE and SIE methods to exploit the strengths of each, i.e. the modeling flexibility of FE and the rigor of SIE methods. The resulting hybrid is often referred as finite element boundary integral (FE-BI) method [10, 27, 28]. In this hybrid, SIEs formulated on the truncation boundary serve as boundary conditions for FE system. SIEs discretized via the MOM are coupled to the FE system through various formulations [29-31]. The matrix vector multiplications pertinent to the BI portion of the hybrid FE-BI systems can be accelerated via the aforementioned acceleration methods for IEs [32, 33]. The above mentioned AIM-FGG acceleration is also extended to FE-BI solvers in this thesis.

Even though there exist well-established FE and IE methods and their hybrids, solving real-life scattering and radiation problems still stays as a challenge. Difficulty often arises when geometrically intricate devices with sub-wavelength features have to be modeled on large platforms such as antenna systems mounted on spacecrafts. Meshes generated for this type of structures will have large variations in element sizes and eventually lead to badly-conditioned system matrices. In the last decade domain decomposition (DD) strategies have become increasingly popular to address this challenge. Instead of tackling the entire computational domain directly, DD method starts with partitioning the computational domain into several sub-domains which allows the separation of small- and large- scale features of the structure. EM scattering from each domain is characterized separately and a global solution is obtained by coupling these solutions by enforcing electric and/or magnetic field boundary conditions on domain boundaries. Often, auxiliary unknowns are defined on domain boundaries to interface domains with each other. DD method has more popularity in FE methods [30, 34-40], while recently some IE based methods are proposed [41-44].

One example to these challenging real-life problems is the EM analysis of plasma engulfed re-entry vehicles. Space vehicles often are affected by communication blackout

upon re-entering the Earth's atmosphere [45]. The blackout arises when the vehicle interacts with the atmosphere around it, giving rise to dense plasmas that are impenetrable by EM waves [46]. The vehicle itself often is covered in a thin and inhomogeneous plasma shell, the density of which decreases rapidly with distance from the vehicle surface. This plasma shell hinders the operation of antennas mounted on the side of the vehicle. As the vehicle moves through space, it also leaves behind a large plasma plume. This plume hinders the operation of antennas mounted on the back of the vehicle. The nature and density of the plasma shell and wake heavily depend on operational and environmental conditions and vary rapidly with the vehicle's position along its trajectory. To analyze the occurrence of communication blackout and facilitate the design of robust navigation systems, fast simulators capable of accurately characterizing the operation of antennas mounted on plasma-engulfed vehicles are called for.

The majority of past efforts aimed at analyzing antennas in plasma environments have relied on finite difference time domain solvers and were limited to relatively simple antennas and platforms [47]. Unfortunately they do not permit modeling of antennas on realistic structures. Recently a ray tracing technique was used to analyze antennas on plasma engulfed re-entry vehicles [48]. Albeit very powerful, this approach does not allow for a detailed modeling of the antennas and/or complex plasma structures that may arise in a turbulent wake.

In this thesis a new full-wave hybrid technique is developed to address the aforementioned challenges in analyzing scattering and radiation from plasma-engulfed space vehicles. Different solvers are combined to be used in the plasma shell and the wake region. A DD-FE-BI solver is used to model EM fields in the plasma near the vehicle as this permits the analysis of highly inhomogeneous plasma distributions near the vehicle. A VIE solver is used to model EM fields in the plasma wake behind the

vehicle; this choice of solver is motivated by the (relatively) slow variations of the plasma parameters in the wake, and the computational benefits associated with accurately modeling wave propagation over large distances using integral as opposed to differential equation methods. The resulting hybrid DD-FE-BI-VIE is solved iteratively and the matrix vector multiplications pertinent to the BI-VIE coupled system are accelerated with AIM-FGG.

1.2 Advances Proposed by This Work

This thesis is aimed at developing fast, DD based hybrid methods for the solution of real life EM scattering and radiation problems. The following contributions are presented in this thesis:

- A high-order SIE solver, using divergence conforming Graglia-Wilton-Peterson basis functions [49], for composite dielectric and PEC structures with arbitrary surface junctions.
- A memory efficient extension of classical AIM, named AIM-FGG, for the acceleration this high-order SIE-solver.
- AIM-FGG accelerated VIE and FE-BI solvers. Roof-top basis functions defined on hexahedral elements are used to discretize VIEs, curl conforming basis functions defined on tetrahedral elements are used to discretize PDEs in FE method, and zeroth order basis functions (RWGs) defined on flat triangles are used to discretize BIs.
- An AIM-FGG accelerated hybrid DD-FE-BI-VIE solver, combining above mentioned VIE and FE-BI solvers, and AIM-FGG acceleration. This solver is capable of modeling highly complex, composite dielectric-PEC structures. The

development of this solver is motivated by the challenges in analyzing scattering and radiation from plasma-engulfed space vehicles.

1.3 Organization of Chapters

The remainder of this thesis is organized as follows. Chapter 2 presents the formulation of the high order SIE solver for analyzing EM scattering and radiation from composite dielectric and PEC structures with arbitrary surface junctions. Surface modeling with curvilinear triangular elements, GWP basis functions, and a procedure for resolving the dependencies of the GWP basis functions intersecting at the surface junctions are detailed in this chapter. Chapter 3 describes the proposed AIM-FGG hybrid for the acceleration of high order MOM-based SIE solvers for composite dielectric and PEC structures. In Chapter 4, we detail a VIE solver and its acceleration with a classical FFT scheme and the proposed AIM-FGG hybrid. The rooftop basis functions and hexahedral discretization elements used in the VIE solver are also described in this Chapter. An AIM-FGG accelerated FE-BI solver is presented in Chapter 5. In Chapter 6, we detail the proposed AIM-FGG accelerated DD-FE-BI-VIE solver. Conclusions and future work are outlined in Chapter 7.

CHAPTER 2
Surface Integral Equations for Piecewise Homogeneous Composite Metallic-Dielectric Structures

2.1 Introduction

Method of Moments (MOM) based surface integral equation (SIEs) solvers are widely used for analyzing time-harmonic EM interactions with composite metallic and dielectric structures. The literature abounds with SIE methods for isolated metallic and dielectric structures [refs]. However, these methods are usually not generalized for composite structures with arbitrary metal-dielectric junctions. In the earlier studies on this topic metallic and dielectric objects are often assumed to be removed from each other [ref] or the junction treatment is not discussed [ref]. In [24] a high-order SIE approach, which uses curvilinear triangular patches to represent the surfaces, and high order Graglia-Wilton-Peterson (GWP) basis functions [49] to expand the surface currents, is presented. However in this approach open metallic surfaces are not considered and the junction treatment is not discussed. Recently, [50] and [51] introduced systematic procedures to treat the general metal-dielectric junction problem and presented results for low-order SIEs solvers in which flat triangular patches and Rao-Wilton-Glisson (RWG) basis functions are used for surface modeling and current expansion, respectively.

This chapter describes an extension to the high-order SIE approach in [24] to handle open metallic surfaces and general metal-dielectric junctions using the procedures prescribed in [50, 51]. The remainder of this chapter is organized as follows: Section 2.2 reviews the well known electric, magnetic, and combined-field integral equations (EFIE, MFIE, and CFIE) for perfect electrically conducting surfaces (PEC) and Poggio-Miller-Chang-Harrrington-Wu-Tsai (PMCHWT) formulation for dielectric interfaces for a single domain object. Their generalization to multi domain composite structures is elucidated in Section 2.3. Discretization of the surfaces using curvilinear and flat triangular elements, and high-order basis function expansion of the unknown surface currents are explained in Section 2.4.1. MOM solution of the SIEs and the treatment of general metal-dielectric junctions are detailed in Section 2.4.2 and 2.4.3, respectively. Finally, numerical results that serve to validate the presented formulation are presented in Section 2.5.

2.2 Integral Equations for a Single Domain Object

Consider a homogeneous penetrable object with surface S_1 residing in an unbounded background medium. S_1 divides the entire space D into two (exterior and interior) homogeneous domains D_1 and D_2 as shown in Fig. 2.1(a). Let ε_p, μ_p, and $\eta_p = \sqrt{\mu_p / \varepsilon_p}$ denote the permittivity, permeability, and wave impedance of D_p, $p = 1, 2$. The object (D_2) is excited from inside and outside by impressed electric and magnetic current sources $\{\mathbf{J}_p^i, \mathbf{M}_p^i\}$, $p = 1, 2$ with angular frequency ω. These currents generate the incident electric and magnetic fields $\{\mathbf{E}_p^i, \mathbf{H}_p^i\}$ in an unbounded homogeneous medium with constitutive parameters $\{\varepsilon_p, \mu_p\}$. The objective is to find the total electric and magnetic fields $\{\mathbf{E}_p, \mathbf{H}_p\}$ in D_p, $p = 1, 2$. The classical approach is to separate the original problem into external and internal equivalent problems by

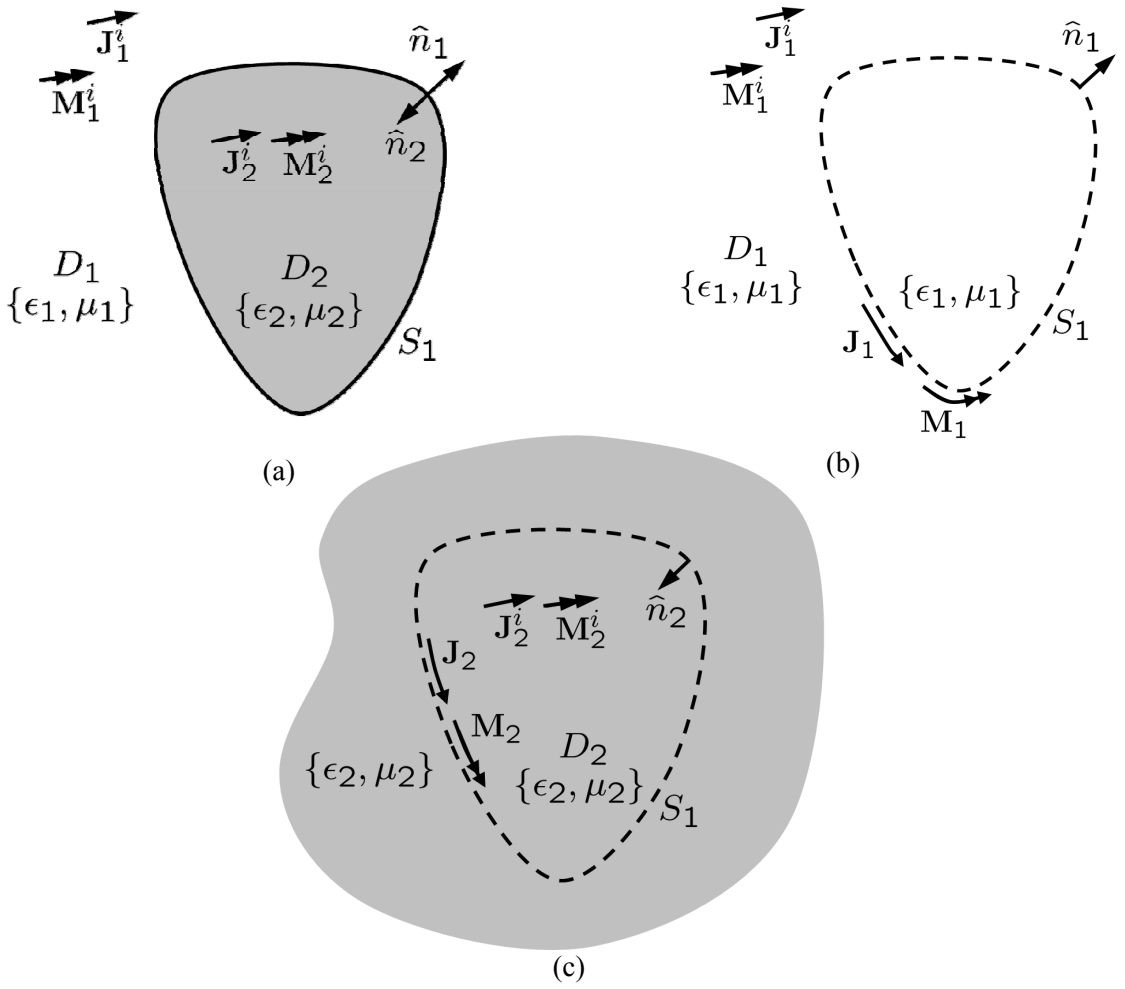

Figure 2.1: (a) Original Problem. (b) External equivalent problem. (c) Internal equivalent problem.

introducing unknown surface electric and magnetic currents $\{\mathbf{J}_1, \mathbf{M}_1\}$ and $\{\mathbf{J}_2, \mathbf{M}_2\}$, respectively, on S_1. These currents are chosen such that

$$\mathbf{J}_p(\mathbf{r}) = \hat{\mathbf{n}}_p \times \mathbf{H}_p(\mathbf{r}), \quad \mathbf{M}_p(\mathbf{r}) = \mathbf{E}_p \times \hat{\mathbf{n}}_p(\mathbf{r}) \quad \mathbf{r} \in S_1 \tag{2.1}$$

where $\hat{\mathbf{n}}_p$ is the unit normal on S_1 pointing towards D_p, $p = 1, 2$. $\{\mathbf{J}_p, \mathbf{M}_p\}$ generate electric and magnetic fields

$$\mathbf{E}_p^s(\mathbf{r}) = \frac{1}{2}\hat{\mathbf{n}}_p \times \mathbf{M}_p - \eta_p \mathcal{L}_p \mathbf{J}_p + \mathcal{K}_p \mathbf{M}_p, \tag{2.2}$$

$$\mathbf{H}_p^s(\mathbf{r}) = \frac{1}{2}\mathbf{J}_p \times \hat{\mathbf{n}}_p - \mathcal{K}_p \mathbf{J}_p - \mathcal{L}_p \mathbf{M}_p / \eta_p \tag{2.3}$$

in an unbounded homogeneous medium with $\{\varepsilon_p, \mu_p\}$, $p = 1, 2$, where the integral operators $\mathcal{L}_p$ and $\mathcal{K}_p$ are defined as

$$\mathcal{L}_p \mathbf{X} = \int_{S_p} \left[jk_p \mathbf{X}(\mathbf{r}') + \frac{j}{k_p} \nabla\nabla' \cdot \mathbf{X}(\mathbf{r}') \right] g_p(\mathbf{r} - \mathbf{r}')\, ds', \tag{2.4}$$

$$\mathcal{K}_p \mathbf{X} = \int_{S_p} \mathbf{X}(\mathbf{r}) \times \nabla g_p(\mathbf{r} - \mathbf{r}')\, ds'. \tag{2.5}$$

In (2.4)-(2.5), $g_p(\mathbf{r} - \mathbf{r}') = e^{-jk_p|\mathbf{r}-\mathbf{r}'|} / (4\pi|\mathbf{r} - \mathbf{r}'|)$ and $k_p = \omega\sqrt{\varepsilon_p \mu_p}$ are the Green's function and the wavenumber of the medium p, $\mathcal{K}_p$ is evaluated in Cauchy principle value sense, and $\mathbf{X}$ stands for $\mathbf{J}_p$ or $\mathbf{M}_p$. In the external equivalent problem, $\{\mathbf{J}_1, \mathbf{M}_1\}$ radiate together with the impressed sources $\{\mathbf{J}_1^i, \mathbf{M}_1^i\}$ to generate the original fields

$$\mathbf{E}_1(\mathbf{r}) = \mathbf{E}_1^s(\mathbf{r}) + \mathbf{E}_1^i(\mathbf{r}), \quad \mathbf{r} \in D_1 \tag{2.6}$$

$$\mathbf{H}_1(\mathbf{r}) = \mathbf{H}_1^s(\mathbf{r}) + \mathbf{H}_1^i(\mathbf{r}), \quad \mathbf{r} \in D_1 \tag{2.7}$$

in D_1 and zero fields in D_2. Similarly for the internal equivalent problem $\{\mathbf{J}_2, \mathbf{M}_2\}$ radiate together with the impressed sources $\{\mathbf{J}_2^i, \mathbf{M}_2^i\}$ to generate total fields

$$\mathbf{E}_2(\mathbf{r}) = \mathbf{E}_2^s(\mathbf{r}) + \mathbf{E}_2^i(\mathbf{r}), \quad \mathbf{r} \in D_2 \tag{2.8}$$

$$\mathbf{H}_2(\mathbf{r}) = \mathbf{H}_2^s(\mathbf{r}) + \mathbf{H}_2^i(\mathbf{r}), \quad \mathbf{r} \in D_2 \tag{2.9}$$

inside D_2 and zero fields inside D_1. Then, the integral equations on S_1 is obtained by enforcing the boundary conditions, i.e. the continuity of the tangential electric and magnetic fields,

$$\hat{\mathbf{n}}_1 \times \mathbf{E}_1(\mathbf{r}) = \hat{\mathbf{n}}_1 \times \mathbf{E}_2(\mathbf{r}), \quad \mathbf{r} \in S_1 \tag{2.10}$$

$$\hat{\mathbf{n}}_1 \times \mathbf{H}_1(\mathbf{r}) = \hat{\mathbf{n}}_1 \times \mathbf{H}_2(\mathbf{r}), \quad \mathbf{r} \in S_1 \tag{2.11}$$

which also imply that $\mathbf{J}_1 = -\mathbf{J}_2$ and $\mathbf{M}_1 = -\mathbf{M}_2$. Substitution of (2.2), (2.6) and (2.8) into (2.10), and (2.3), (2.7) and (2.9) into (2.11) yields the well known Poggio-Miller-Chang-Harrrington-Wu-Tsai (PMCHWT) equations [52]

$$\hat{\mathbf{n}}_1 \times \left[\left(\eta_1 \mathcal{L}_1 + \eta_2 \mathcal{L}_2 \right) \mathbf{J}_1 - \left(\mathcal{K}_1 + \mathcal{K}_2 \right) \mathbf{M}_1 \right] = \hat{\mathbf{n}}_1 \times \left[\mathbf{E}_1^i \left(\mathbf{r} \right) - \mathbf{E}_2^i \left(\mathbf{r} \right) \right] \quad \mathbf{r} \in S_1 \tag{2.12}$$

$$\hat{\mathbf{n}}_1 \times \left[\left(\mathcal{K}_1 + \mathcal{K}_2 \right) \mathbf{J}_1 + \left(\mathcal{L}_1 / \eta_1 + \mathcal{L}_2 / \eta_2 \right) \mathbf{M}_1 \right] = \hat{\mathbf{n}}_1 \times \left[\mathbf{H}_1^i \left(\mathbf{r} \right) - \mathbf{H}_2^i \left(\mathbf{r} \right) \right] \quad \mathbf{r} \in S_1 \tag{2.13}$$

which can be solved simultaneously for $\left\{ \mathbf{J}_1, \mathbf{M}_1 \right\}$.

Now consider the case when D_2 represents a non-penetrable (PEC) object. Fields inside D_2 are zero, hence only the exterior problem is considered in the analysis. The boundary conditions on a PEC surface dictate that $\hat{\mathbf{n}}_1 \times \mathbf{E}_1 = 0$ and $\hat{\mathbf{n}}_1 \cdot \mathbf{H}_1 = 0$. From the former boundary condition it is understood that magnetic currents vanish on a metallic surface, $\mathbf{M}_1 = 0$. Under these conditions (2.12) and (2.13) will reduce to well known electric and magnetic field integral equations (EFIE and MFIE)

$$\hat{\mathbf{n}}_1 \times \eta_1 \mathcal{L}_1 \mathbf{J}_1 = \hat{\mathbf{n}}_1 \times \mathbf{E}_1^i \left(\mathbf{r} \right) \left(\text{EFIE} \right) \quad \mathbf{r} \in S_1 \tag{2.14}$$

$$\frac{1}{2} \mathbf{J}_1 + \hat{\mathbf{n}}_1 \times \mathcal{K}_1 \mathbf{J}_1 = \hat{\mathbf{n}}_1 \times \mathbf{H}_1^i \left(\mathbf{r} \right) \left(\text{MFIE} \right) \quad \mathbf{r} \in S_1. \tag{2.15}$$

To eliminate the interior resonance problem with the closed PEC objects (like D_2) the combined field integral equation (CFIE) can be applied by linearly combining (2.14) and (2.15) as

$$\text{CFIE} = \alpha \hat{\mathbf{n}}_1 \times \text{EFIE} + \eta_1 \left(1 - \alpha \right) \text{MFIE}. \tag{2.16}$$

where $\alpha \in \mathbb{R}$ is a parameter ranging between 0 and 1. The MFIE and CFIE can only be applied to closed PEC surfaces, while the EFIE applies to open surfaces as well.

2.3 Generalization to composite objects with multiple domains

2.3.1 Geometry and notation

Consider a general composite structure (Fig. 2.2(a)) comprising open and closed PEC surfaces and piecewise homogenous dielectric domains residing in an unbounded homogeneous background medium. Let M be the total number of PEC or dielectric domains (including the background medium). Let Ω_{PEC} and Σ_{PEC} represents the set of closed PEC domains and open or closed PEC surfaces, respectively. Let S_{pq} (or S_{qp}) represent the surface separating D_p and D_q, clearly $S_{pq} = S_{qp}$, $p, q = 1,...,M$. It should be noted that $S_{pq} \in \varnothing$ if D_p and D_q do not share an common interface; and S_{pp} represents open PEC surfaces in D_p. Each domain is bounded by the union of surfaces

$$S_p = \bigcup_{q=1}^{M} S_{pq} \tag{2.17}$$

Let N_s^p, and $\hat{\mathbf{n}}_{pq}$ represent the dimension of the non-empty set $q = 1,...,M : S_{pq} \in \varnothing$, and the unit normal vector on S_{pq} pointing towards D_p.

2.3.2 Equivalent problem in each domain

First step in constructing SIEs for composite structures is to set up an equivalent problem in each domain D_p, $p \in 1,...,M : D_p \notin \Omega_{PEC}$ in a similar fashion to the single domain case (Fig. 2.2(b)-(e)). Suppose that the structure is excited with electric and magnetic fields $\left\{\mathbf{E}_p^i, \mathbf{H}_p^i\right\}$ generated by impressed sources $\left\{\mathbf{J}_p^i, \mathbf{M}_p^i\right\}$ residing in one or more non-metallic domains D_p, $p \in 1,...,M : D_p \notin \Omega_{PEC}$. In response to the excitation, equivalent magnetic and electric currents $\left\{\mathbf{J}_{pq}, \mathbf{M}_{pq}\right\}$ are induced on surfaces S_{pq}, $p, q = 1,...,M$. It should be noted that $\mathbf{J}_{pq} = \mathbf{M}_{pq} = 0$ if $S_{pq} \in \varnothing$ or $D_p \in \Omega_{PEC}$, $\mathbf{M}_{qp} = 0$ if $S_{pq} \in \Sigma_{PEC}$, and $\left\{\mathbf{J}_{pq}, \mathbf{M}_{pq}\right\}$ are not necessarily equal to $\left\{\mathbf{J}_{qp}, \mathbf{M}_{qp}\right\}$.

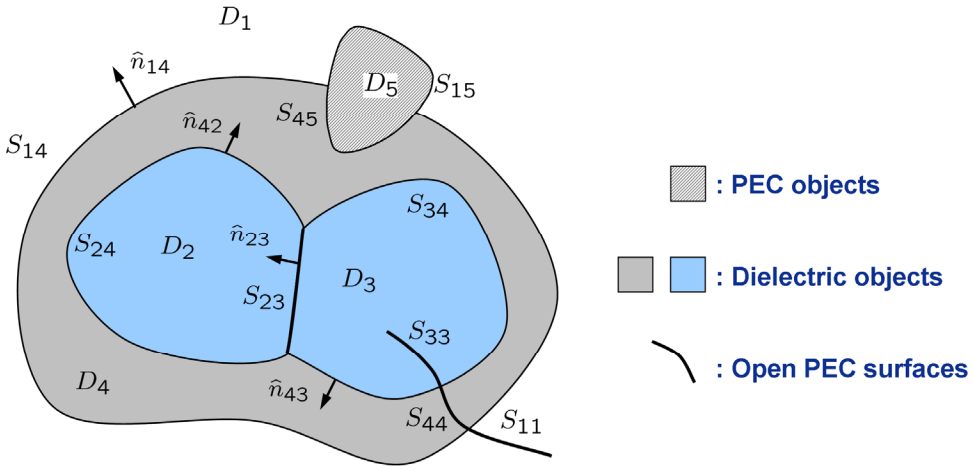

(a) Original multi-domain problem

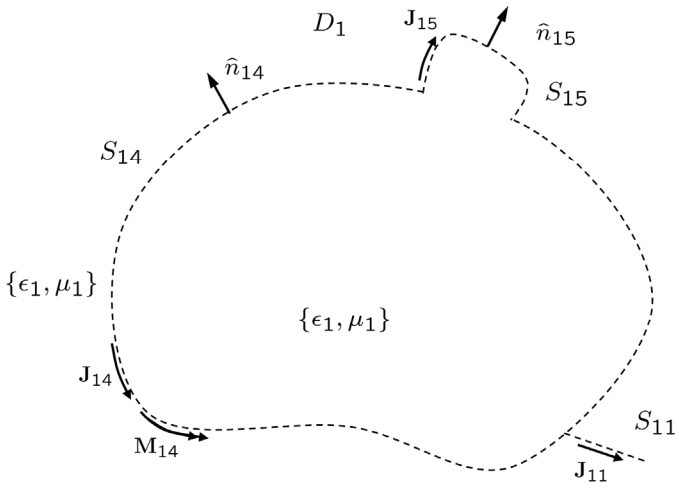

$$S_1 = S_{11} \cup S_{14} \cup S_{15}, \quad S_{11}, S_{15} \in \Sigma_{PEC}$$

(b) Equivalent problem for D_1

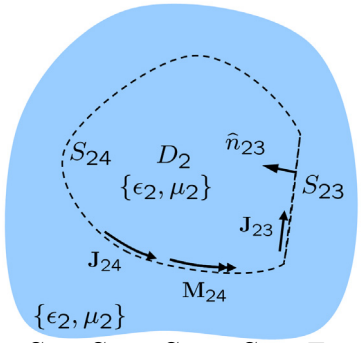

$$S_2 = S_{23} \cup S_{24}, \quad S_{23} \in \Sigma_{PEC}$$

(c) Equivalent problem for D_2

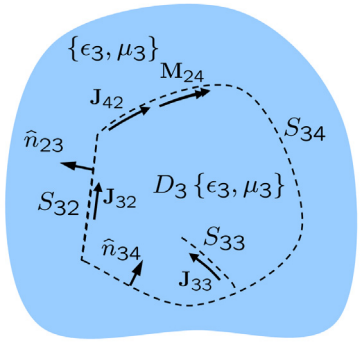

$$S_3 = S_{32} \cup S_{33} \cup S_{34}, \quad S_{32}, S_{33} \in \Sigma_{PEC}$$

(d) Equivalent problem for D_3

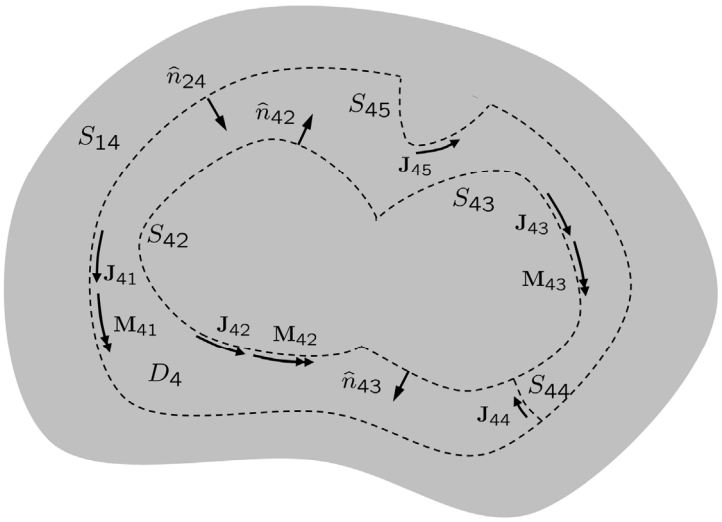

(e) Equivalent problem for D_4

Figure 2.2: An example composite structure with five domains $M = 5$ one of which is a PEC object $\Omega_{PEC} = \{D_5\}$. In this example $\Sigma_{PEC} = S_{11} \cup S_{33} \cup S_{44} \cup S_{15} \cup S_{45} \cup S_{23}$. Equivalent problems for D_p, $p = 1,...,4,$ are shown in (b)-(e), respectively.

Equivalent problem for each D_p can be stated as finding $\{\mathbf{J}_{pq}, \mathbf{M}_{pq}\}$, $q = 1,...,M$ that radiate together with $\{\mathbf{J}^i_p, \mathbf{M}^i_p\}$ to generate the original fields inside D_p and zero fields outside. More formally, the equivalent problem for D_p can be represented as SIEs in terms of the unknowns $\{\mathbf{J}_{pq}, \mathbf{M}_{pq}\}$

$$\frac{1}{2}\mathbf{M}_{pq}(\mathbf{r}) + \hat{\mathbf{n}}_{pq} \times \sum_{q=1}^{M} \left(\eta_p \mathcal{L}_p \mathbf{J}_{pq} - \mathcal{K}_p \mathbf{M}_{pq} \right) = \hat{\mathbf{n}}_{pq} \times \mathbf{E}^i_p(\mathbf{r}), \quad \mathbf{r} \in S_{pq} \tag{2.18}$$

$$\frac{1}{2}\mathbf{J}_{pq}(\mathbf{r}) + \hat{\mathbf{n}}_{pq} \times \sum_{q=1}^{M} \left(\mathcal{K}_p \mathbf{J}_{pq} + \mathcal{L}_p \mathbf{M}_{pq} / \eta_p \right) = \hat{\mathbf{n}}_{pq} \times \mathbf{H}^i_p(\mathbf{r}), \quad \mathbf{r} \in S_{pq}. \tag{2.19}$$

(2.18) and (2.19) can be derived using the current-field relations

$$\mathbf{M}_{pq}(\mathbf{r}) = \mathbf{E}_p(\mathbf{r}) \times \hat{\mathbf{n}}_{pq}, \quad \mathbf{J}_{pq}(\mathbf{r}) = \hat{\mathbf{n}}_{pq} \times \mathbf{H}_p(\mathbf{r}) \quad \mathbf{r} \in S_{pq}. \tag{2.20}$$

Combining (2.18) and (2.19) from equivalent problems for D_p and D_q using PMCHWT approach yields the following integral equations on a dielectric surface $S_{pq} \notin \Sigma_{PEC}$

$$\hat{\mathbf{n}}_{pq}\times\left[\sum_{q=1}^{M}\left(\eta_p\mathcal{L}_p\mathbf{J}_{pq}-\mathcal{K}_p\mathbf{M}_{pq}\right)+\sum_{p=1}^{M}\left(\eta_q\mathcal{L}_q\mathbf{J}_{qp}-\mathcal{K}_q\mathbf{M}_{qp}\right)\right] = \hat{\mathbf{n}}_{pq}\times\left[\mathbf{E}_p^i(\mathbf{r})+\mathbf{E}_q^i(\mathbf{r})\right] \tag{2.21}$$

$$\hat{\mathbf{n}}_{pq}\times\left[\sum_{q'=1}^{M}\left(\mathcal{K}_p\mathbf{J}_{pq'}+\mathcal{L}_p\mathbf{M}_{pq'}/\eta_p\right)+\sum_{p'=1}^{M}\left(\mathcal{K}_q\mathbf{J}_{qp'}+\mathcal{L}_q\mathbf{M}_{qp'}/\eta_q\right)\right] = \hat{\mathbf{n}}_{pq}\times\left[\mathbf{H}_p^i(\mathbf{r})+\mathbf{H}_q^i(\mathbf{r})\right] \tag{2.22}$$

where $\mathbf{r}\in S_{pq}$, and $\mathbf{J}_{pq}=-\mathbf{J}_{qp}$, $\mathbf{M}_{pq}=-\mathbf{M}_{qp}$. On open PEC surfaces $S_{pq}\in\Sigma_{PEC}$ the EFIE is formulated as

$$\hat{\mathbf{n}}_{pq}\times\left[\sum_{q'=1}^{M}\left(\eta_p\mathcal{L}_p\mathbf{J}_{pq}-\mathcal{K}_p\mathbf{M}_{pq}\right)\right]=\hat{\mathbf{n}}_{pq}\times\mathbf{E}_p^i(\mathbf{r})\quad \mathbf{r}\in S_{pq}. \tag{2.23}$$

Whereas on surfaces bounding closed PEC domains CFIE is used to avoid internal resonance problems, that is

$$\begin{aligned}&\alpha\hat{\mathbf{n}}_{pq}\times\hat{\mathbf{n}}_{pq}\times\left[\sum_{q'=1}^{M}\left(\eta_p\mathcal{L}_p\mathbf{J}_{pq'}-\mathcal{K}_p\mathbf{M}_{pq'}\right)\right]\\ &\eta_p(1-\alpha)\frac{1}{2}\mathbf{J}_{pq}+\eta_p(1-\alpha)\hat{\mathbf{n}}_{pq}\times\left[\sum_{q'=1}^{M}\left(\mathcal{K}_p\mathbf{J}_{pq'}+\mathcal{L}_p\mathbf{M}_{pq'}/\eta_p\right)\right]\\ &=\alpha\hat{\mathbf{n}}_{pq}\times\hat{\mathbf{n}}_{pq}\times\mathbf{E}_p^i(\mathbf{r})+\eta_p(1-\alpha)\hat{\mathbf{n}}_{pq}\times\mathbf{H}_p^i(\mathbf{r})\quad \mathbf{r}\in S_{pq}\end{aligned} \tag{2.24}$$

2.4 Numerical Solution of Integral Equations

2.4.1 High order Geometry Modeling and Basis Functions

To numerically solve (2.18) and (2.19), surfaces S_{pq}, $p,q=1,...,M:S_{pq}\notin\varnothing$ are discretized using a mesh of N_{pq} triangular elements $\Lambda_{pq}^n\left(=\Lambda_{qp}^n\right)$ as

$$S_{pq}\cong\bigcup_{n=1}^{N_{pq}}\Lambda_{pq}^n. \tag{2.25}$$

Triangular elements can categorized as flat or curvilinear. Flat triangular elements are defined by three nodes and they conform exactly to flat surfaces but they provide only an approximation to curved surfaces which cause errors in the solution. These geometrical approximation errors can be reduced (in some cases completely removed) by using curvilinear (high order) triangular elements [53]. In this work only 6-node curvilinear elements are used although the method can easily be generalized to higher order elements.

Equivalent currents $\left\{\mathbf{J}_{pq}, \mathbf{M}_{pq}\right\}$ on the discretized surface are expanded in terms of r^{th} order divergence conforming GWP [49, 53] basis functions as

$$\mathbf{J}_{pq}\left(\mathbf{r}\right) \cong \sum_{n=1}^{N_{pq}} \sum_{e=1}^{N^b} I_{pq}^{ne} \mathbf{S}_{pq}^{ne}\left(\mathbf{r}\right) \qquad p,q \in \{1,...,M\} : S_{pq} \neq \varnothing \tag{2.26}$$

$$\mathbf{M}_{pq}\left(\mathbf{r}\right) \cong \sum_{n=1}^{N_{pq}} \sum_{e=1}^{N^b} K_{pq}^{ne} \mathbf{S}_{pq}^{ne}\left(\mathbf{r}\right) \qquad p,q \in \{1,...,M\} : S_{pq} \notin \Sigma_{PEC},\ S_{pq} \neq \varnothing \tag{2.27}$$

where $\mathbf{S}_{pq}^{ne}\left(\mathbf{r}\right) = \mathbf{S}_{qp}^{ne}\left(\mathbf{r}\right)$ represents the e^{th} basis function on defined on element Λ_{pq}^{n}, N^b is the number of basis functions defined on each element $N^b = \left(r+1\right)\left(r+3\right)$, and $\left\{I_{pq}^{ne}, K_{pq}^{ne}\right\}$ are the corresponding unknown electric and magnetic current coefficients. Using high-order basis functions significantly reduce the errors introduced by the finite expansion of the current. GWP basis functions are interpolatory in nature, i.e. $\left\{I_{pq}^{ne}, K_{pq}^{ne}\right\}$ represent one vector component of the tangential electric and magnetic fields at an interpolation point $\mathbf{r}_{pq}^{ne}$ in Λ_{pq}^{n}. r^{th} order GWP functions interpolate $r+1$ points along the triangle edges and $r\left(r+1\right)$ points in each triangular element. Zeroth order GWP basis functions are equivalent to the half RWG basis functions [54]. Fig 2.3 (a) and (b) depicts zeroth and first order GWP functions defined on flat and curvilinear triangles, respectively.

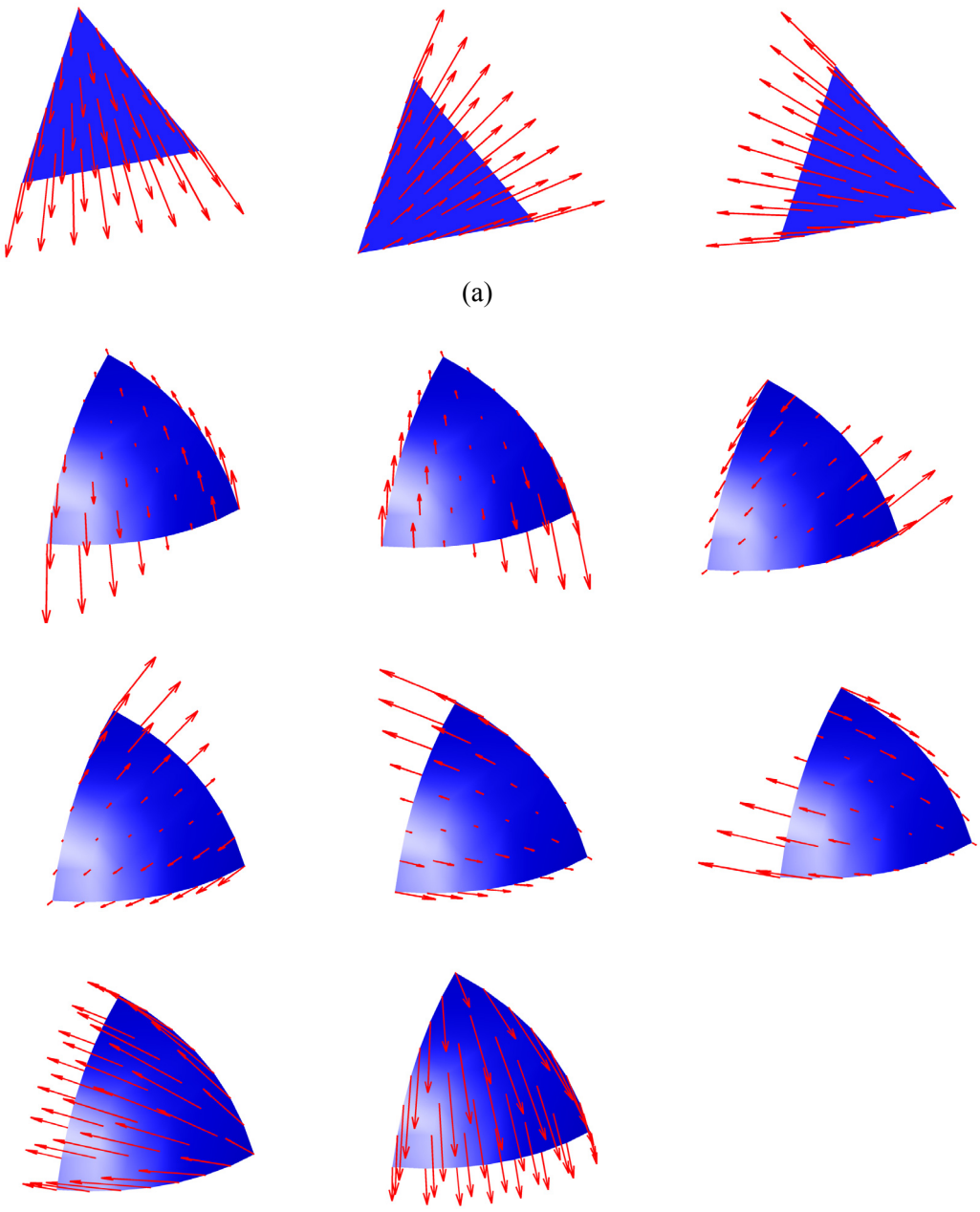

Figure 2.3: Generic illustration of (a) zeroth and (b) first-order GWP basis functions defined on flat and curvilinear triangular elements. $N=(0+1)(0+3)=3$ zeroth order and $N=(1+1)(1+3)=8$ first order basis functions are supported on each element.

2.4.2 MOM System of Equations

In this section a new notation for indexing basis functions is introduced to simplify the formulation that follows. The new notation replaces the pair (n,e) with a single index $k = nN^b + e$

$$\mathbf{S}_{pq}^{k} = \mathbf{S}_{pq}^{ne}, \quad I_{pq}^{k} = I_{pq}^{ne}, \quad K_{pq}^{k} = K_{pq}^{ne} \tag{2.28}$$

where $n = 1,...,N_{pq} - 1,\ e = 1,...,N^b,$ and $1 \le k \le N_{pq}N^b$.

Double summations in (2.26) and (2.27) can easily be rearranged as a single summation with the new notation. Substitution of (2.26) and (2.27) with the new notation into (2.18) and (2.19), and Galerkin testing the resulting equations yields the matrix equation

$$\sum_{q'=1}^{M} \mathbf{Z}_{pqq'}\mathbf{U}_{qq'} + \sum_{p'=1}^{M} \mathbf{Z}_{qpp'}\mathbf{U}_{pp'} = \mathbf{V}_{pq} + \mathbf{V}_{qp} \tag{2.29}$$

In (2.29) $\mathbf{U}_{pq}$ and $\mathbf{V}_{pq}$ are the $N_{pq}N^b -$ vectors of unknown current coefficients and tested incident fields, and $\mathbf{Z}_{pqq'}$ is the $2N_{pq}N^b \times 2N_{pq'}N^b$ MOM impedance matrix

$$\mathbf{U}_{pq} = \begin{bmatrix} \mathbf{I}_{pq} \\ \mathbf{K}_{pq} \end{bmatrix}_{2N_{pq}N^b \times 1} \quad \mathbf{V}_{pq} = \begin{bmatrix} \mathbf{V}_{pq}^{E} \\ \mathbf{V}_{pq}^{H} \end{bmatrix}_{2N_{pq}N^b \times 1} \quad \mathbf{Z}_{pqq'} = \begin{bmatrix} \mathbf{Z}_{pqq'}^{EE} & \mathbf{Z}_{pqq'}^{EH} \\ \mathbf{Z}_{pqq'}^{HE} & \mathbf{Z}_{pqq'}^{HH} \end{bmatrix}_{2N_{pq}N^b \times 2N_{pq'}N^b} \tag{2.30}$$

Their entries are

$$\mathbf{I}_{pq}(k) = I_{pq}^{k}, \quad k = 1,...,N_{pq}N^b \tag{2.31}$$

$$\mathbf{K}_{pq}(k) = K_{pq}^{k}, \quad k = 1,...,N_{pq}N^b \tag{2.32}$$

$$\mathbf{V}_{pq}^{E}(k) = \int_{S_{pq}} \mathbf{S}_{pq}^{k}(\mathbf{r}) \cdot \mathbf{E}_{p}^{i}(\mathbf{r})\, ds, \quad k = 1,...,N_{pq}N^b \tag{2.33}$$

$$\mathbf{V}_{pq}^{H}(k) = \int_{S_{pq}} \mathbf{S}_{pq}^{k}(\mathbf{r}) \cdot \mathbf{H}_{p}^{i}(\mathbf{r})\, ds \quad k = 1,...,N_{pq}N^b \tag{2.34}$$

$$\mathbf{Z}_{pqq'}^{EE}(k,k') = \left\langle \mathbf{S}_{pq}^{k}(\mathbf{r}), \eta_p \mathcal{L}_p\left(\mathbf{S}_{pq'}^{k'}\right) \right\rangle_{S_{pq}} \quad k = 1,...,N_{pq}N^b,\ k' = 1,...,N_{pq'}N^b \tag{2.35}$$

$$\mathbf{Z}_{pqq'}^{EH}\left(k,k'\right)=-\left\langle \mathbf{S}_{pq}^{k}\left(\mathbf{r}\right),\mathcal{K}_{p}\left(\mathbf{S}_{pq'}^{k'}\right)\right\rangle_{S_{pq}},\quad k=1,...,N_{pq}N^{b},\ k'=1,...,N_{pq'}N^{b} \tag{2.36}$$

$$\mathbf{Z}_{pqq'}^{HE}\left(k,k'\right)=-\mathbf{Z}_{pqq'}^{EH}\left(k,k'\right) \tag{2.37}$$

$$\mathbf{Z}_{pqq'}^{HH}\left(k,k'\right)=\mathbf{Z}_{pqq'}^{EE}\left(k,k'\right)\big/\eta_{j}^{2} \tag{2.38}$$

where the inner product $\left\langle\ \right\rangle_{S_{pq}}$ is defined as

$$\left\langle \mathbf{a}\left(\mathbf{r}\right),\mathbf{b}\left(\mathbf{r}\right)\right\rangle_{S_{pq}}=\int\limits_{S_{pq}}\mathbf{a}\left(\mathbf{r}\right)\mathbf{b}\left(\mathbf{r}\right)ds \tag{2.39}$$

The entries of these matrices are given explicitly by

$$\begin{aligned}\mathbf{Z}_{pqq'}^{EE}\left(k,k'\right)&=j\omega\mu_{p}\int\limits_{S_{pq}}\int\limits_{S_{pq'}}\mathbf{S}_{pq}^{k}\left(\mathbf{r}\right)\cdot\mathbf{S}_{pq'}^{k'}\left(\mathbf{r}\right)g_{p}\left(\mathbf{r}-\mathbf{r}'\right)ds'ds\\&\quad+\frac{1}{j\omega\varepsilon_{p}}\int\limits_{S_{pq}}\int\limits_{S_{pq'}}\nabla\cdot\mathbf{S}_{pq}^{k}\left(\mathbf{r}\right)\nabla\cdot\mathbf{S}_{pq'}^{k'}\left(\mathbf{r}\right)g_{p}\left(\mathbf{r}-\mathbf{r}'\right)ds'ds\end{aligned} \tag{2.40}$$

$$\mathbf{Z}_{pqq'}^{EH}\left(k,k'\right)=-\int\limits_{S_{pq}}\mathbf{S}_{pq}^{k}\left(\mathbf{r}\right)\times\hat{\mathbf{n}}_{pq}\cdot\nabla\times\int\limits_{S_{pq'}}\mathbf{S}_{pq'}^{k'}\left(\mathbf{r}\right)g_{p}\left(\mathbf{r}-\mathbf{r}'\right)ds'ds \tag{2.41}$$

Similarly, MOM systems for EFIE and CFIE are given by

$$\sum_{q'=1}^{M}\begin{bmatrix}\mathbf{Z}_{pqq'}^{EE} & \mathbf{Z}_{pqq'}^{EH}\end{bmatrix}\begin{bmatrix}\mathbf{I}_{pq'}\\ \mathbf{K}_{pq'}\end{bmatrix}=\mathbf{V}_{p}^{E} \tag{2.42}$$

and

$$\begin{aligned}\sum_{q'=1}^{M}\begin{bmatrix}\frac{1}{2}\mathbf{I}_{pqq'}+\alpha\mathbf{Z}_{pqq'}^{EE}+\eta_{p}\left(1-\alpha\right)\mathbf{Z}_{pqq'}^{HE} & \alpha\mathbf{Z}_{pqq'}^{EH}+\eta_{p}\left(1-\alpha\right)\mathbf{Z}_{pqq'}^{HH}\end{bmatrix}\begin{bmatrix}\mathbf{I}_{pq'}\\ \mathbf{K}_{pq'}\end{bmatrix}\\=\alpha\mathbf{V}_{pq}^{E}+\eta_{j}\left(1-\alpha\right)\mathbf{V}_{pq}^{H},\end{aligned} \tag{2.43}$$

respectively. In (2.43) $\mathbf{I}_{pqq'}$ is a $N_{pq}\times N_{pq'}$ matrix with entries

$$\mathbf{I}_{pqq'}\left(k,k'\right)=\begin{cases}1 & \text{for } q=q',\ k'=k\\ 0 & \text{otherwise}\end{cases} \tag{2.44}$$

2.4.3 Independent Unknowns and Junction Treatment

To solve for all $\mathbf{U}_{pq} \quad p,q = 1,....,M : \; S_{pq} \notin \varnothing$, a global system of equations must be assembled by combining (2.29) for dielectric surfaces, (2.42) for open PEC surfaces, and (2.43) for surfaces bounding PEC domains. It should be noted that so far in the formulation every basis function is paired with a different coefficient in (2.29) (also in (2.42) and (2.43)). However these coefficients do not constitute an independent set. That is, a straight-forward assembly of these equations will lead to a rank deficient system. This section presents a systematic procedure to remove the dependent coefficients. Removing a coefficient can be interpreted as combining rows and columns of an initially rank deficient system matrix.

Rule 1: If two triangular elements Λ_{pq}^{n} and Λ_{pq}^{m} share a common edge, the interpolation points on this edge are shared by the basis functions defined on these elements, i.e. $\mathbf{r}_{pq}^{k} = \mathbf{r}_{pq}^{l}$. Initially two independent set of coefficients $\left\{I_{pq}^{k}, K_{pq}^{k}\right\}$ and $\left\{I_{pq}^{l}, K_{pq}^{l}\right\}$ are paired with these basis functions. To ensure the current continuity from one triangle to the other, the redundant set is removed from the independent unknown list and basis functions corresponding to these unknowns are paired with the coefficients

$$I_{pq}^{l} = -I_{pq}^{k}, \qquad K_{pq}^{l} = -K_{pq}^{k}. \tag{2.45}$$

Rule 2: At an interface between two dielectric domains D_p and D_q, initially two independent set of unknowns $\left\{I_{pq}^{k}, K_{pq}^{k}\right\}$ and $\left\{I_{qp}^{k}, K_{qp}^{k}\right\}$ are defined. To enforce the conditions $\mathbf{J}_{qp} = -\mathbf{J}_{pq}$, $\mathbf{M}_{qp} = -\mathbf{M}_{pq}$ explicitly, one set is removed from the independent unknown list and the basis functions corresponding to these unknowns are paired with the coefficients

$$I_{qp}^{k} = -I_{pq}^{k}, \qquad K_{qp}^{k} = -K_{pq}^{k}. \tag{2.46}$$

Hence, only one set of independent unknown current coefficients represent the currents on $S_{pq} = S_{qp}$.

Rule 3: For a PEC surface $S_{pq} \in \Sigma_{PEC}$ magnetic currents are zero $\mathbf{M}_{pq} = 0,$ so $K_{pq}^{k},\ n = 1,...,N_{pq},\ k = 1,...,N_{pq}N^{b}$ are removed from the independent unknown list. Also if the PEC surface S_{pq} is at an interface where two dielectric domains intersect, independent unknowns I_{pq}^{k} and I_{qp}^{k} on both sides of S_{pq} are kept intact.

Rule 4: At a junction where only dielectric surfaces intersect Rules 1 and 2 are systematically applied. As a result only a single set of unknowns remains in the independent unknown list.

Rule 5: At a junction where only PEC surfaces intersect Rules 1 and 3 are systematically applied. If the junction is totally immersed in a single domain one of the independent unknowns must be removed to satisfy the Kirchhoff's current law. Let $\left\{I_{pp}^{k}, I_{pp}^{k+1},..,I_{pp}^{k+n-1}\right\}$ represent the remaining set of unknowns at such a junction after applying Rules 1 and 3. Then the final set of independent unknowns will be

$$\left\{I_{pp}^{k}, I_{pp}^{k+1},...,-\sum_{\alpha=1}^{n-1} I_{pp}^{k+\alpha}\right\}. \tag{2.47}$$

Rule 6: At a general PEC-dielectric junction Rules 1, 2, and 3 are applied. Since magnetic currents vanish on PEC surfaces, all magnetic current coefficients must be removed, including the ones on dielectric surfaces (to satisfy the continuity).

Fig. 2.4 depicts how these rules are applied for various dielectric-PEC surface junction examples. Note that the original index notation (n,e) is used in the examples to discriminate between different elements and local basis function indices.

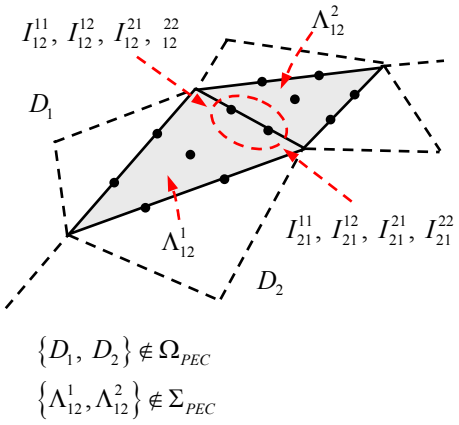

	Initial	Rule 1	Rule 2
I_{12}^{11}	a_1	a_1	a_1
I_{12}^{12}	a_2	a_2	a_2
I_{12}^{21}	a_3	$-a_1$	$-a_1$
I_{12}^{22}	a_4	$-a_2$	$-a_2$
I_{21}^{11}	a_5	a_5	$-a_1$
I_{21}^{12}	a_6	a_6	$-a_2$
I_{21}^{21}	a_7	$-a_5$	a_1
I_{21}^{22}	a_8	$-a_6$	a_2

(a) Dielectric interface -- 1st order basis functions

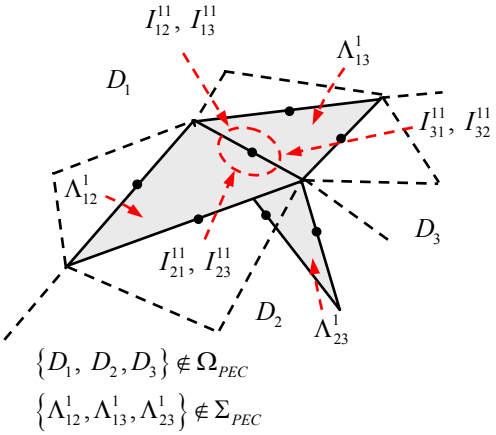

	Initial	Rule 1	Rule 2
I_{12}^{11}	a_1	a_1	a_1
I_{13}^{11}	a_2	$-a_1$	$-a_1$
I_{21}^{11}	a_3	a_3	$-a_1$
I_{23}^{11}	a_4	$-a_3$	a_1
I_{31}^{11}	a_5	a_5	a_1
I_{32}^{11}	a_6	$-a_5$	$-a_1$

(b) Intersection of three dielectric domains/surfaces – 0th order basis functions

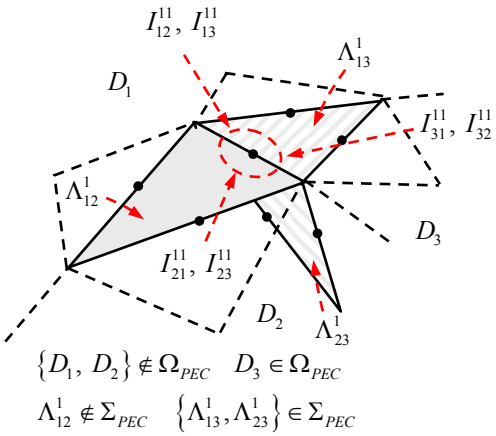

	Initial	Rule 1	Rule 2&3
I_{12}^{11}	a_1	a_1	a_1
I_{13}^{11}	a_2	$-a_1$	$-a_1$
I_{21}^{11}	a_3	a_3	$-a_1$
I_{23}^{11}	a_4	$-a_3$	a_1
I_{31}^{11}	a_5	a_5	0
I_{32}^{11}	a_6	$-a_5$	0

(c) Intersection of PEC and dielectric surfaces – 0th order basis functions

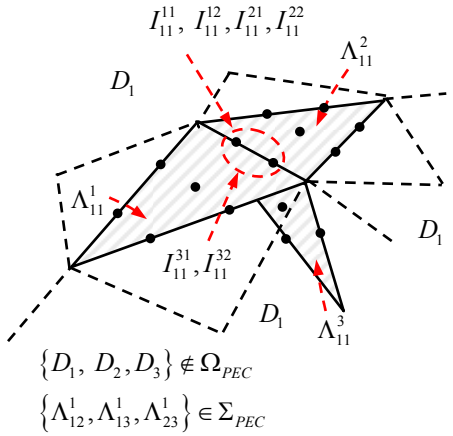

	Initial	Rule 1
I_{11}^{11}	a_1	a_1
I_{11}^{12}	a_2	a_2
I_{11}^{21}	a_3	a_3
I_{11}^{22}	a_4	a_4
I_{11}^{31}	a_5	$a_1 - a_3$
I_{11}^{32}	a_6	$a_2 - a_4$

(d) Intersection of three PEC surfaces immersed into a single domain -- 1st order basis functions

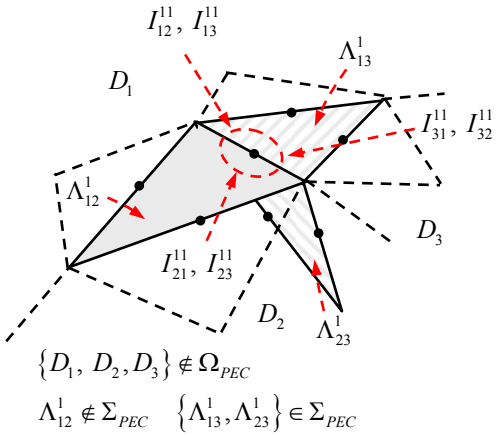

	Initial	Rule 1	Rule 2
I_{12}^{11}	a_1	a_1	a_1
I_{13}^{11}	a_2	$-a_1$	$-a_1$
I_{21}^{11}	a_3	a_3	$-a_1$
I_{23}^{11}	a_4	$-a_3$	a_1
I_{31}^{11}	a_5	a_5	a_5
I_{32}^{11}	a_6	$-a_5$	$-a_5$

(e) Intersection of three dielectric domains with two PEC surfaces – 0th order basis functions

Figure 2.4: Unknown resolution procedure for various PEC-dielectric junction cases.

2.4.4 Global System of Equations

After resolving the independent set of unknowns in $\mathbf{U}_{pq}\ \ p,q=1,....,M$: by following the rules described above, (2.29) can be assembled together to yield the global system of equations

$$\mathbf{ZU} = \mathbf{V} \tag{2.48}$$

where

$$\mathbf{Z} = \sum_{p=1}^{M} \sum_{q=1}^{M} \mathbf{R}_{pq}^{T} \sum_{q'=1}^{M} \mathbf{Z}_{pqq'} \mathbf{R}_{pq'} \tag{2.49}$$

$\mathbf{V}$ is the right hand side vector

$$\mathbf{V} = \sum_{p=1}^{M} \sum_{q=1}^{M} \mathbf{R}_{pq}^{T} \mathbf{V}_{pq}. \tag{2.50}$$

and $\mathbf{U}$ is the $N-$vector of independent unknowns, where N represents the total number of independent unknowns. Here, $\mathbf{R}_{pq} \quad p,\ q = 1,....,M : S_{pq} \notin \varnothing$ is a highly sparse selection matrix of dimension $\left(2N_{pq}N^{b}\right) \times N,$ mapping the independent unknowns to the original set of current coefficients on S_{pq}. The transpose matrix $\mathbf{R}_{pq}^{T}$ performs the inverse of this mapping. Each row of $\mathbf{R}_{pq}$ has a possible single non-zero entry of either 1 or -1. The only exception occurs when the structure comprises open PEC surface junctions immersed in a single domain. In that case rows with multiple entries (of either 1 or -1) can appear in $\mathbf{R}_{pq}$. (2.49) can be represented in a more compact way as

$$\mathbf{Z} = \sum_{p=1}^{M} \mathbf{R}_{p}^{T} \mathbf{Z}_{p} \mathbf{R}_{p} \tag{2.51}$$

where $\mathbf{Z}_{p}$ and $\mathbf{R}_{p}$ are the $N_{s}^{p} \times N_{s}^{p}$ and $N_{s}^{p} \times 1$ block matrices comprising the blocks $\mathbf{Z}_{pqq'}$ and $\mathbf{R}_{pq} \quad q,\ q' = 1,...,M :\ S_{pq},\ S_{pq'} \notin \varnothing,$ respectively. Let N_{p} represent the number of elements in S_{p}

$$N_{p} = \sum_{q=1}^{M} N_{pq} \tag{1.52}$$

Then, the total dimensions of $\mathbf{Z}_{p}$ and $\mathbf{R}_{p}$ are $N_{p}N^{b} \times N_{p}N^{b}$ and $N_{p}N^{b} \times N,$ respectively.

When N is large, (2.48) can only be solved iteratively, a process that requires the repeated multiplication of $\mathbf{Z}$ by trial solution vectors. It should be noted that although the matrices $\mathbf{Z}_{p}$ are dense, the global system matrix $\mathbf{Z}$ can be sparse for multi domain

structures. The sparsity of $\mathbf{Z}$ depends only on the topology of the structure. The memory and CPU requirements of MOM-based iterative solvers therefore scale as

$$O\left(\sum_{p=1}^{M}\left(N_p N^b\right)^2\right) \tag{1.53}$$

and

$$N_{iter} O\left(\sum_{p=1}^{M}\left(N_p N^b\right)^2\right), \tag{1.54}$$

respectively. Here N_{iter} is the number of iterations required for the solution to reach a given accuracy; typically $N_{\text{iter}} \ll N$, especially when D is electrically large and uniformly discretized. For a single object problem these requirements reduce to classical $O\left(N^2\right)$ and $N_{iter} O\left(N^2\right)$ memory and CPU requirements for dense matrix systems. In this work the solver is implemented using the popular message passing interface (MPI) programming model, and executed on clusters of processors to reduce these computational requirements.

2.5 Numerical Results

This section presents numerical results that demonstrate the high-order accuracy of the solver and validate the solver for various metal-dielectric junction cases. First, scattering from PEC and dielectric spheres is analyzed and the results are compared to those obtained using exact analytical methods, i.e. Mie series solutions. The parallelization efficiency of the solver is demonstrated via CPU time statistics. Next, various objects with arbitrary metal-dielectric junctions are analyzed and the junction resolution rules are validated. In the examples mesh density is represented by average edge length of the triangular elements δ. A transpose free quasi minimal residual (TFQMR) iterative scheme [55] is used to solve MOM matrix equations. Unless

otherwise stated a diagonal pre-conditioner is used in all simulations, tolerance of TFQMR is set to 10^{-6}, and N_{iter} represents number of iterations required to reach this tolerance in the examples. The surface meshes are generated using a commercially available software package NX-IDEAS. All simulations are carried out on a cluster of dual-core 2.8 GHz AMD Opteron 2220 SE processors at the Center for Advanced Computing, University of Michigan.

2.5.1 PEC Sphere

The first test geometry is a PEC sphere of radius 1 m. The sphere is illuminated by a plane wave

$$\mathbf{E}^i = \hat{\mathbf{p}} e^{-jk_0 \hat{\mathbf{k}}\mathbf{r}}, \tag{2.55}$$

with $\hat{\mathbf{p}} = \hat{\mathbf{x}}$ and $\hat{\mathbf{k}} = \hat{\mathbf{z}}$, and frequency $f =$ 300 MHz. A CFIE solver with $\alpha = 0.6$ is used to compute the RCS of the sphere and the results are compared to the Mie series solution. Three simulations are performed for different orders of surface discretization elements and basis functions: (i) flat elements with zeroth order (RWG) basis functions (case A), (ii) curvilinear elements with first order basis functions (case B), and (iii) an exact representation of the sphere surface (obtained by mapping flat elements onto the sphere) with second order basis functions (case C). Fig. 2.5(a) shows the bistatic RCS of the sphere in E-plane ($\phi = 0°$) and H-plane ($\phi = 90°$) obtained for Case A, B, and C. The accuracy of the solutions are measured quantitatively by computing the relative root-mean-square (RMS) error in the bistatic RCS

$$\text{RMS Error} = \frac{\sqrt{\sum_{i=1}^{N_s} \left| \sigma(\theta_i, \phi_i) - \sigma^{ref}(\theta_i, \phi_i) \right|^2}}{\sqrt{\sum_{i=1}^{N_s} \sigma^{ref}(\theta_i, \phi_i)^2}} \tag{2.56}$$

where σ and σ^{ref} represent the bistatic RCS obtained by the proposed solver and Mie series solution. In (5.31) N_s represents the total number of observation angles (θ_i) in E- $(\phi_i = 0°)$ and H- $(\phi_i = 90°)$ planes at which RCS is sampled. Average edge length δ, number of unknowns N and iterations N_{iter}, and the RMS error in the simulations are given in Table 2.1 As expected higher order simulations are yielding more accurate results for almost the same N. To demonstrate the parallel efficiency of the solver, matrix-vector multiplication time (total wall-time for the iterative solver divided by the number of matrix-vector multiplications) versus number of processors is plotted in Fig. 2.5(b). The solver has excellent parallel scalability for all cases. Fig. 2.5(b) also shows that matrix-vector multiplication is faster in high-order solvers. This result is due to the data structures designed to store the MOM impedance matrix. Access time to these data structures depends strongly to the number of elements instead of the order of basis functions.

	δ	N	N_{iter}	RMS Error
Case A	$0.1\lambda_0$	4,371	53	1.14×10^{-2}
Case B	$0.2\lambda_0$	4,360	91	1.4×10^{-3}
Case C	$0.25\lambda_0$	4,074	224	4.59×10^{-4}

Table 2.1: Average edge length δ (in terms of wavelength), number of unknowns and iterations, and RMS error in RCS results in three simulations performed for the PEC sphere.

2.5.2 Dielectric Sphere

In the second example scattering from a dielectric sphere of radius 1 m and relative permittivity $\varepsilon_r = \varepsilon/\varepsilon_0 = 2.5 - j0.5$ is analyzed. Three simulations are carried out with the same surface discretization-basis function combinations described in Section 2.5.1. The sphere is illuminated with a $\hat{\mathbf{p}} = \hat{\mathbf{x}}$ polarized plane-wave propagating in $\hat{\mathbf{k}} = \hat{\mathbf{z}}$ direction at

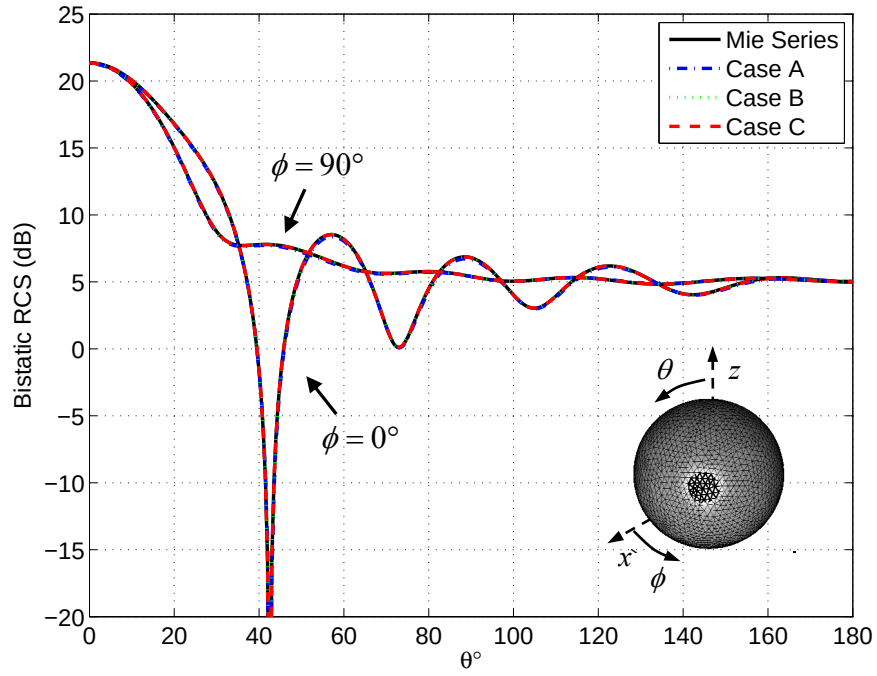

(a)

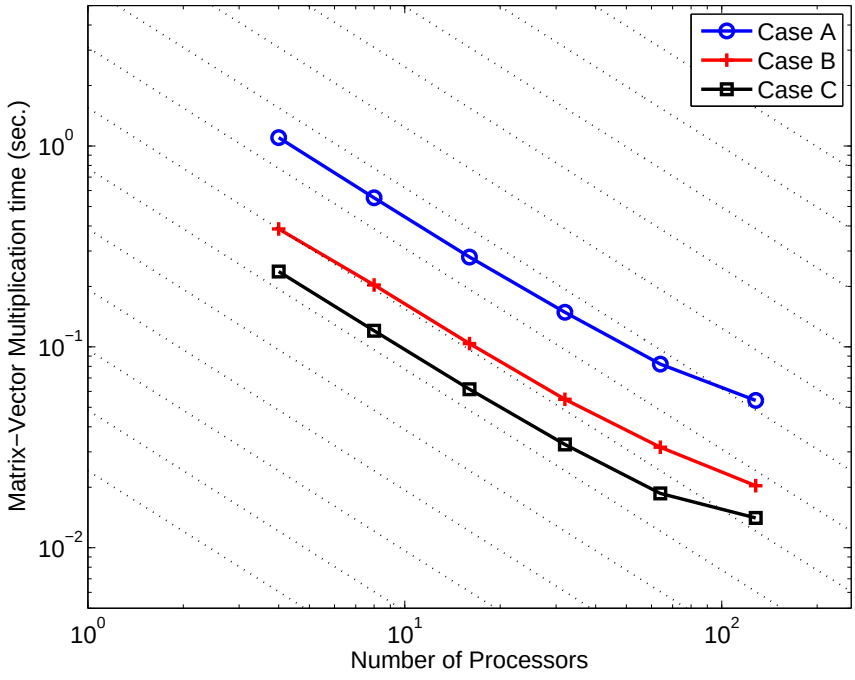

(b)

Figure 2.5: (a) Bistatic RCS of a PEC sphere of radius 1 m. An $\hat{\mathbf{x}}$ – polarized plane wave propagating in z – direction illuminates the sphere. (b) Average wall-clock time per iteration vs. number of processors.

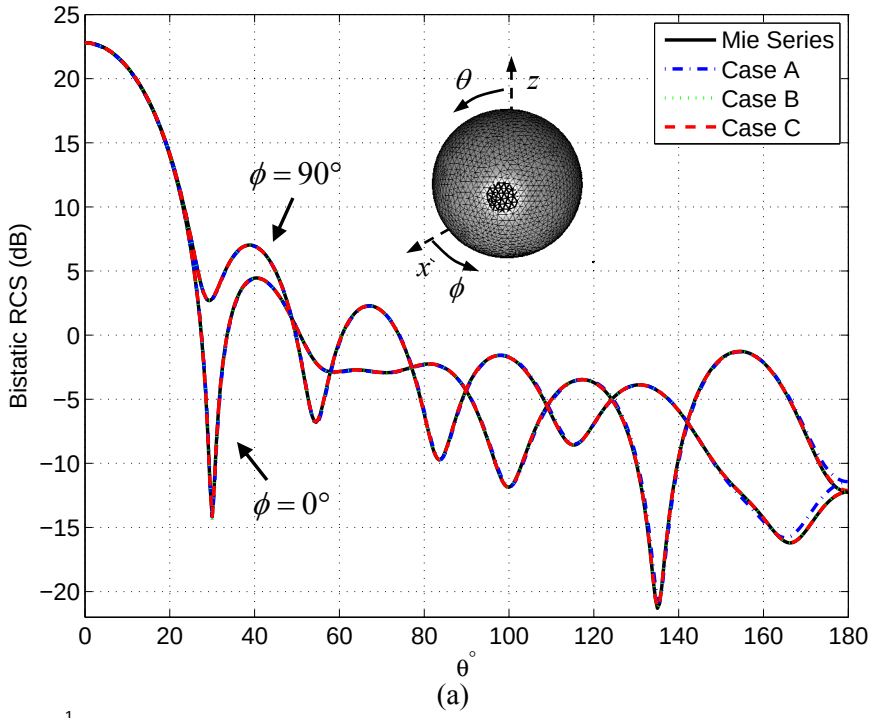

(a)

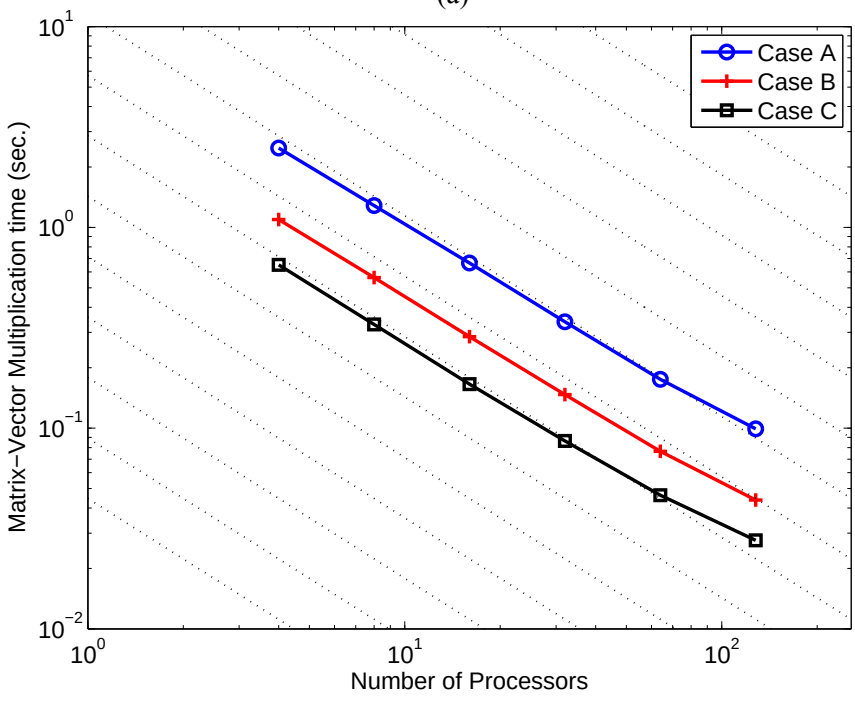

(b)

Figure 2.6: (a) Bistatic RCS of a dielectric sphere of radius 1 m and relative permittivity $\varepsilon_r = 2 - j0.5$. An $\hat{\mathbf{x}}$ – polarized plane wave propagating in z – direction illuminates the sphere. (b) Average wall-clock time per iteration vs. number of processors.

$f = 300$ MHz. Fig. 2.6(a) shows the bistatic RCS of the sphere in E-plane ($\phi = 0°$) and H-plane ($\phi = 90°$) obtained for case A, B, and C. Table 2.2 shows δ, N, N_{iter}, and the RMS error in RCS in the simulations. Similar to PEC sphere example, solver has excellent parallel scalability for all cases as shown in Fig. 2.6(b).

	δ	N	N_{iter}	RMS Error
Case A	$0.1\lambda_0$	8,742	215	6.8×10^{-3}
Case B	$0.2\lambda_0$	8,720	423	1.46×10^{-3}
Case C	$0.25\lambda_0$	8,148	1047	3.92×10^{-4}

Table 2.2: Average edge length in the mesh, number of unknowns and iterations, and RMS error in RCS results in three simulations performed for the dielectric sphere.

2.5.3 High-order Accuracy and Efficiency

The high-order behavior of the proposed solver is further demonstrated via analysis of scattering from a dielectric sphere of radius 1 m with $\varepsilon_r = 2.5$, which is illuminated by a $\hat{\mathbf{p}} = \hat{\mathbf{x}}$ polarized plane wave propagating in $\hat{\mathbf{k}} = \hat{\mathbf{z}}$ direction at $f = 75$ MHz. Three sets of simulations are performed: In each set, the simulation is repeated while the discretization density is increased for a given order of discretization elements and basis functions. The RMS error of the RCS values computed in these simulations is plotted in Fig. 2.5. The figure clearly demonstrates the high-order convergence of the proposed scheme.

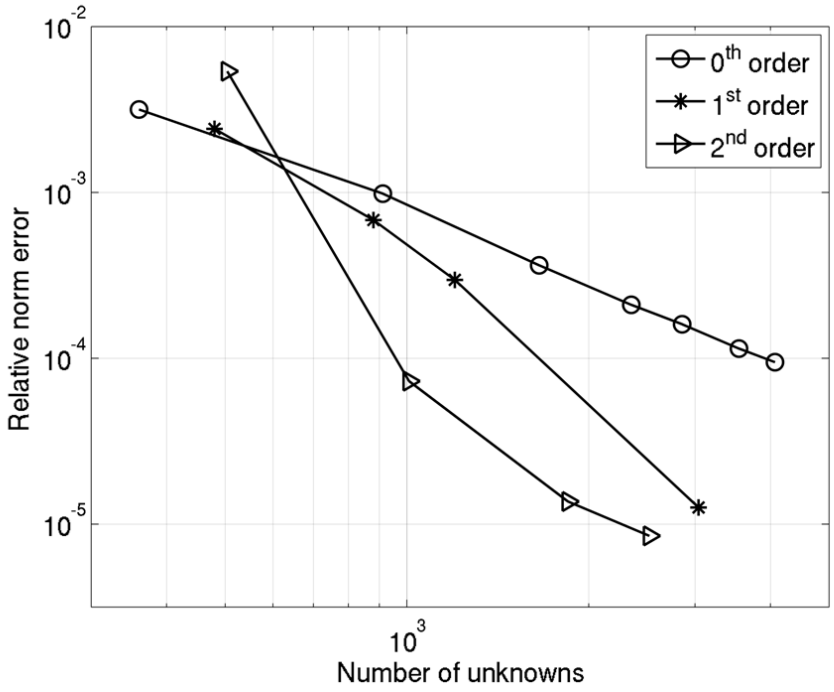

Figure 2.7: Relative norm error in bistatic RCS (with respect to Mie series solution) for different orders of basis functions and discretization densities.

2.5.4 Multi Domain Dielectric Sphere

To validate the rules for resolving unknowns at purely dielectric surface junctions, scattering from a dielectric sphere of radius 1.25 m with $\varepsilon_r = 2 - j0.5$ is analyzed and the results are compared to the Mie series solution. The incident field is a $\hat{\mathbf{p}} = \hat{\mathbf{x}}$ polarized plane wave propagating in $\hat{\mathbf{k}} = \hat{\mathbf{z}}$ direction at $f = 300$ MHz. Two simulations are performed for different decompositions of the sphere. In the first case (A) the sphere is modeled as two dielectric hemispheres (Fig. 2.6(b)), where as in the second case (B) a two layer sphere with an inner radius of 1.0 m is considered (Fig. 2.6(c)). In both cases $M = 3,$ surfaces are discretized with curvilinear (six node) elements, and second order basis functions are used. Fig. 2.6(a) shows the bistatic RCS of the sphere in E-plane ($\phi = 0°$) and H-plane ($\phi = 90°$) obtained for case A, B. Results are both in an excellent

agreement with the Mie series solution. Table 2.2 shows N, N_{iter}, and the RMS error in the simulations.

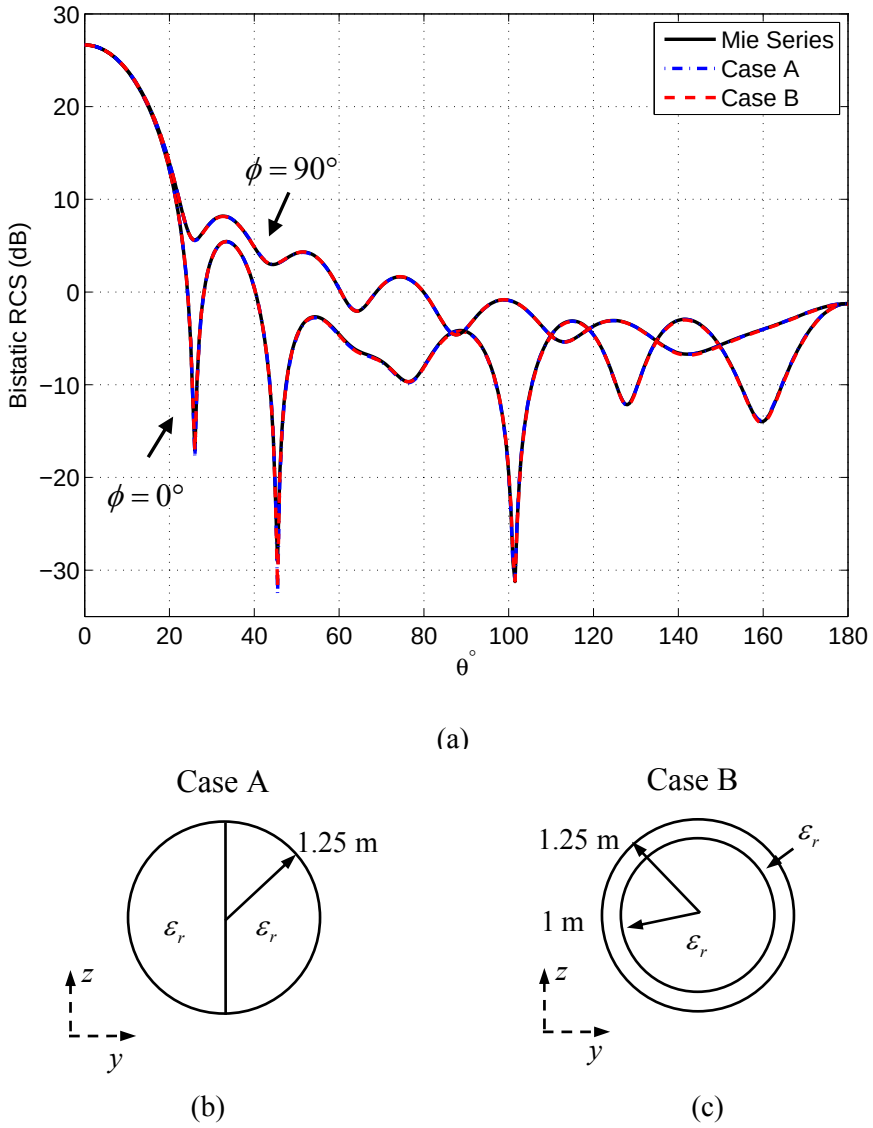

Figure 2.8: (a) Bistatic RCS of a homogeneous dielectric sphere of radius 1.25 m and relative permittivity $\varepsilon_r = 2.5 - j0.5$. A $\hat{\mathbf{p}} = \hat{\mathbf{x}}$ polarized plane-wave propagating in the $\hat{\mathbf{k}} = \hat{\mathbf{z}}$ direction at frequency $f = 300$ MHz illuminates the sphere. The geometry is decomposed into multiple domains in two different ways as illustrated in (b) and (c), denoted as Case A and B.

	N	N_{iter}	RMS Error
Case A	21,072	1,094	7.28×10^{-4}
Case B	27,552	1,821	5.42×10^{-4}

Table 2.3: Number of unknowns and iterations, and RMS error in RCS results in the simulations performed for the multi domain dielectric sphere.

2.5.5 PEC Disk

In this example the scattering from a PEC disk of radius 0.5 m is analyzed to validate some of the PEC-dielectric junction unknown resolution rules. The disk is illuminated by a $\hat{\mathbf{p}} = \hat{\mathbf{x}}$ polarized plane wave propagating in $\hat{\mathbf{k}} = \hat{\mathbf{z}}$ direction at $f = 300$ MHz. Simulations are performed for two equivalent models of the PEC disk geometry as shown in Figs. 2.9 (b) and (c). In the first case the disk is modeled in a regular way, whereas in the second it is enclosed in a dummy dielectric sphere of the same radius, with free-space permittivity. In both cases surfaces are discretized with curvilinear (six node) elements, and first order basis functions are used. Fig. 2.9 (a) shows the comparison of the bistatic RCS in E-plane ($\phi = 0°$) and H-plane ($\phi = 90°$) obtained for cases A and B. δ, N, and N_{iter} for these simulations are given in Table 2.4.

	δ	N	N_{iter}
Case A	$0.2\lambda_0$	1,530	2,089
Case B	$0.2\lambda_0$	24,980	566

Table 2.4: Average element length in the mesh, number of unknowns and iterations for the PEC disk example.

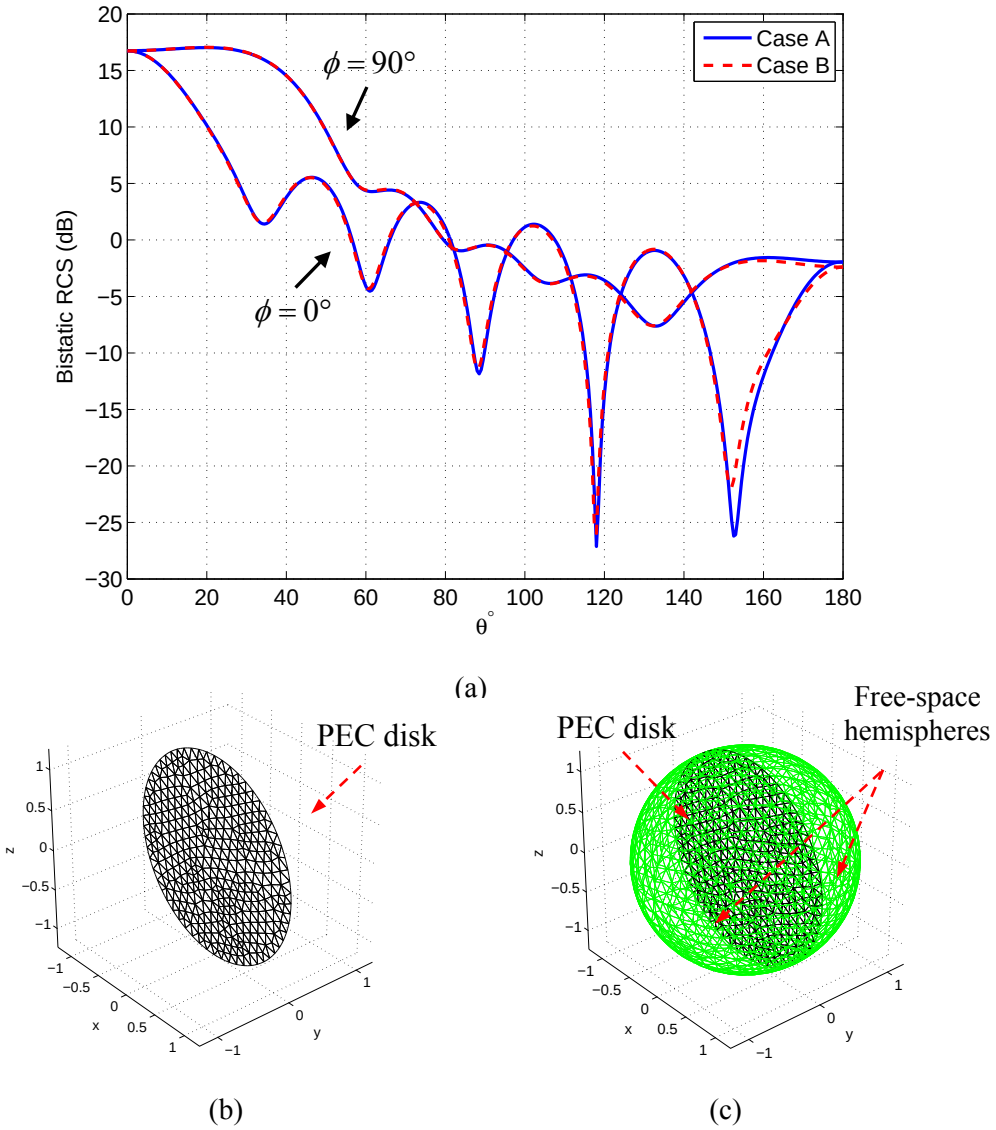

Figure 2.9: (a) Bistatic RCS of a PEC disk of radius 1 m in the *xz* plane. First the structure itself (b) is simulated (denoted as Case A in the results), then two dummy free-space hemispheres are placed next to the original structure to test the dielectric-metallic junctions (denoted as Case B in the results).

2.5.6 Hemispherical PEC Shell Conforming to a Dielectric Sphere

Junction unknown resolution rules are further validated by analyzing the scattering from a composite structure comprising a hemispherical PEC shell conforming to a dielectric sphere of radius 1 m with $\varepsilon_r = 2.5 - j0.5$. Similar to previous examples the structure is illuminated by a $\hat{\mathbf{p}} = \hat{\mathbf{x}}$ polarized plane wave propagating in $\hat{\mathbf{k}} = \hat{\mathbf{z}}$ direction at $f = 300$ MHz. Simulations are performed for two equivalent models of the geometry as depicted in Figs. 2.10 (b) and (c). In the first case the dielectric sphere is represented by a single domain, whereas in the second it is decomposed into two hemispheres. In both cases surfaces are discretized with curvilinear elements, and first order basis functions are used. δ, N, and N_{iter} in the simulations are given in Table 2.5. The bistatic RCS of the sphere in E-plane ($\phi = 0°$) and H-plane ($\phi = 90°$) is depicted in Fig. 2.10. The relative norm of the difference between two RCS results is 1.6×10^{-4}. Relative norm difference formula can be obtained by letting σ and σ^{ref} in (5.31) represent the RCS results of case A and B, respectively.

	δ	N	N_{iter}
Case A	$0.2\lambda_0$	15,936	1,261
Case B	$0.2\lambda_0$	17,420	1,338

Table 2.5: Average element length, number of unknowns and iterations for the hemispherical PEC shell conforming to a dielectric sphere example.

2.5.7 PEC Hemisphere

Next consider a PEC hemisphere of radius 1 m. The structure is illuminated by a $\hat{\mathbf{p}} = \hat{\mathbf{x}}$ polarized plane wave propagating in $\hat{\mathbf{k}} = \hat{\mathbf{z}}$ direction at $f = 300$ MHz. Simulations are performed for two equivalent models of the geometry as depicted in Figs. 2.11 (b)

and (c) . In the first case the structure is modeled in a regular way, whereas in the second it is attached to a dummy dielectric sphere with the same radius and free-space permittivity. In both cases surfaces are discretized with curvilinear elements, and first order basis functions are used. A hybrid PMCHWT-EFIE solver is used to compute the RCS results. δ, N, and N_{iter} in the simulations are given in Table 2.6. The bistatic RCS of the sphere in E-plane ($\phi = 0°$) and H-plane ($\phi = 90°$) is depicted in Fig. 2.11 (a). The relative norm of the difference (defined in the previous example) between two RCS results is 1.6×10^{-4}.

	δ	N	N_{iter}
Case A	$0.2\lambda_0$	5,250	1,100
Case B	$0.2\lambda_0$	12,250	951

Table 2.6: Average element length, number of unknowns and iterations for the PEC hemisphere example.

2.5.8 Tri-Plate PEC Junction

Finally a tri-plate PEC junction configuration analyzed and the monostatic RCS results are compared to the published results in [51]. The structure comprises three rectangular PEC plates of dimension $0.5\ \text{m} \times 1\ \text{m}$ intersecting at the common (long) edge as shown in Fig. 11 (b). The vertical plate forms a $90°$ angle with the other two horizontal plates. Flat elements and zeroth order basis functions are used in the simulation, and the excitation frequency $f = 300$ MHz.. RCS of the structure for $\hat{\theta}\hat{\theta}-$ and $\hat{\phi}\hat{\phi}-$ polarizations are in a very good agreement with [51] as shown in Fig. 11 (a).

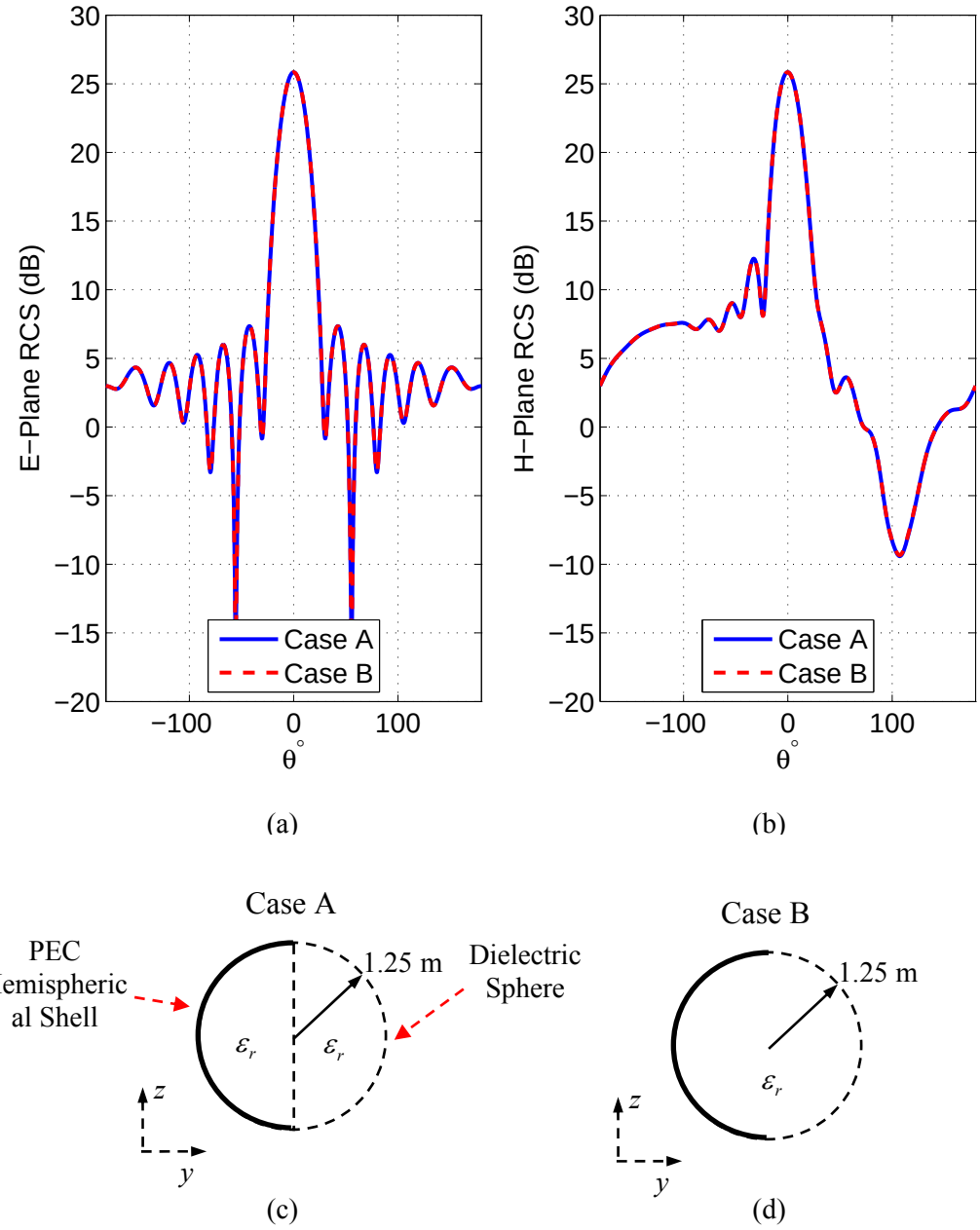

Figure 2.10: Bistatic RCS of a hemispherical PEC shell conforming to a dielectric sphere of radius 1 m and permittivity $\varepsilon_r = 2.5 - j0.5$ in (a) E- and (b) H- planes. The geometry is decomposed into multiple domains in two different ways as illustrated in (c) Case A and (d) Case B. PEC surfaces and dielectric interfaces are denoted by thick and dashed lines, respectively.

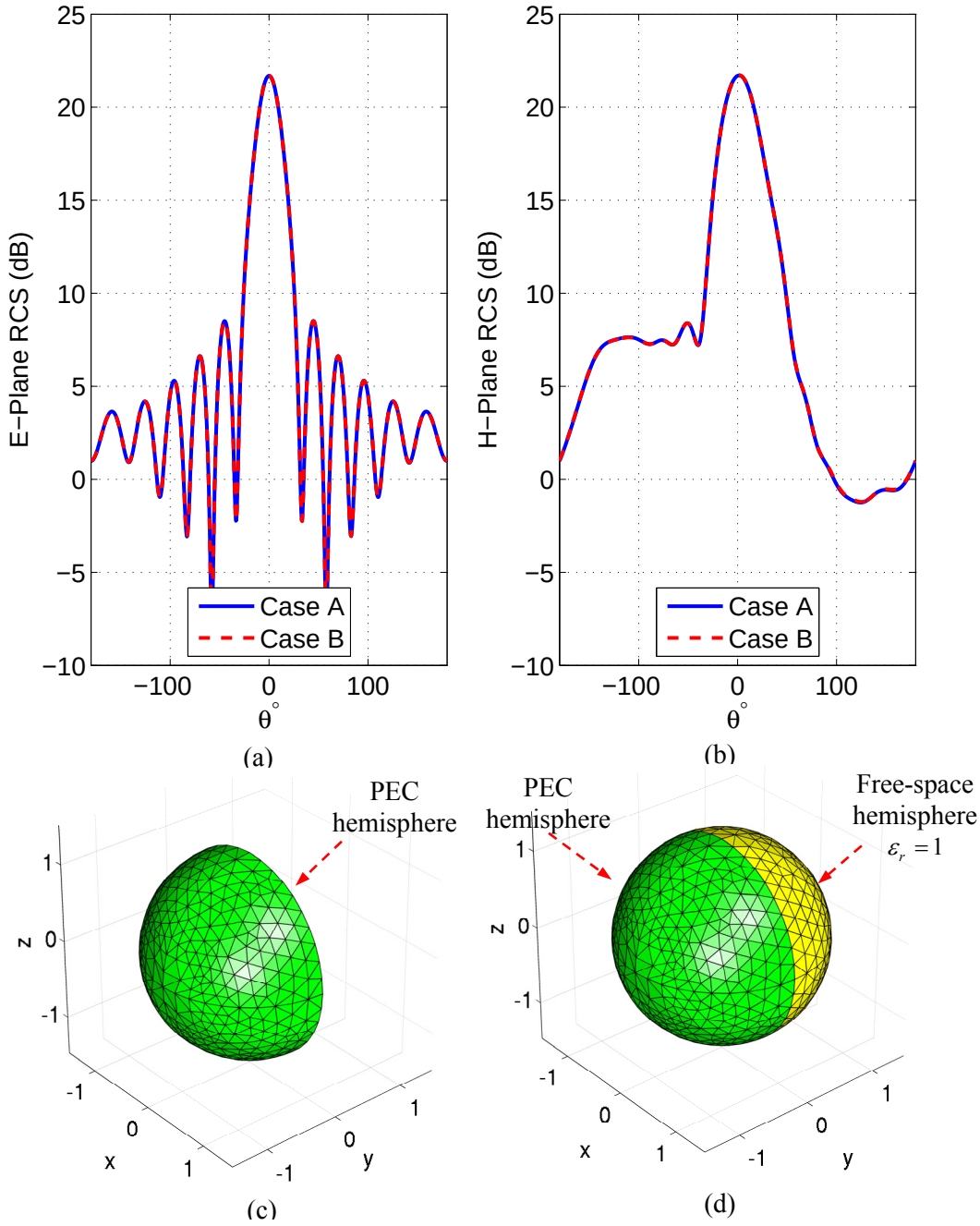

Figure 2.11: Bistatic RCS of a PEC hemisphere of radius 1 m in (a) E- and (b) H- planes. Two cases are considered: First the structure itself (c) is simulated (denoted as Case A), then a dummy free-space hemisphere is placed next to the original structure to test the dielectric-metallic junctions.

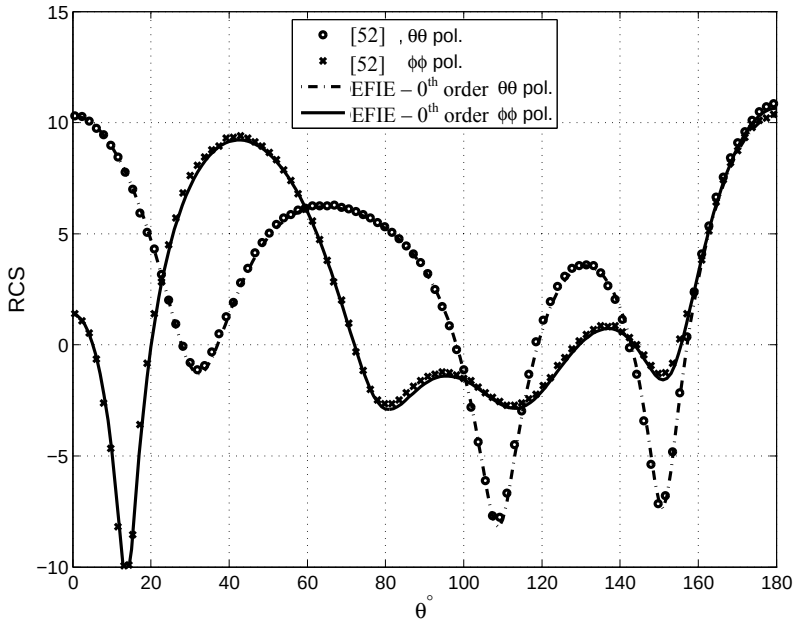

(a)

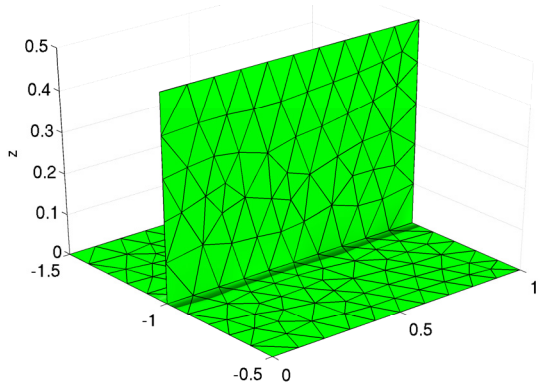

(b)

Figure 2.12: (a) Monostatic RCS of a tri-plate structure (b) Tri-plate structure.

CHAPTER 3
Adaptive Integral Method with Fast Gaussian Gridding

3.1 Introduction

The adaptive integral method (AIM) uses an auxiliary set of discrete sources residing on a uniform grid to represent "far-fields" generated by actual currents [17]. This representation permits the use of fast Fourier transforms (FFTs) to accelerate matrix-vector multiplications required in the iterative solution of the MOM systems such as the one described in Chapter 2. The AIM reduces the iterative solution's memory and CPU requirements to $O(N_c \log N_c)$ and $O(N_c) + \gamma O(N)$, respectively. Here, N_c is the number of nodes on the auxiliary grid enclosing the scatterer; for volumetric and quasi-planar scatterers, where the basis functions occupy most of the space enclosed by the AIM grid, $N_c \propto N$; for arbitrarily shaped three-dimensional (3D) surface scatterers $N_c \propto N^{1.5}$. Conventional methods to map basis functions onto the uniform AIM grid include moment [17] and far-field [18, 56] matching. The first and the second terms in the above memory requirement estimate are due to the storage of matrices/vectors needed for FFTs and the AIM mapping coefficients, respectively. When using the aforementioned mapping methods, γ scales as $O(\mathcal{M}^3)$ with $\mathcal{M}$ being the number of AIM mapping coefficients per source/basis function along each dimension; $\mathcal{M}$, along with the grid spacing, controls the accuracy of the AIM [17]. When large $\mathcal{M}$ are needed to ensure high accuracies, the $\gamma O(N)$ mapping component of the scheme's memory requirements often

overtakes the $O(N_c)$ FFT component, eventually ruling out the usage of the AIM on electrically large problems. While this storage bottleneck in principle can be avoided by computing moment or far-field matching mapping coefficients on the fly (i.e., during each iteration), in practice such is seldom done as the computational overhead is very high. (Note: there exist other FFT-based techniques [57-60] that use auxiliary grids to accelerate matrix-vector multiplications in iterative integral equation solvers. To the authors' knowledge, they all suffer from the same drawback as the above-referenced AIMs in that they require storage of mapping coefficients to not to compromise the scheme's CPU requirements.)

Here, we incorporate fast Gaussian gridding (FGG) [21, 22], a recently developed scheme for computing nonuniform FFTs (NUFFTs) with low memory requirements, into the AIM framework. In the proposed AIM-FGG hybrid, γ is of $O(1)$, that is, it no longer scales as $O(\mathcal{M}^3)$ as in classical AIM schemes. NUFFT [61] or unequally spaced FFT [62] algorithms combine interpolation/convolution schemes with regular FFTs to rapidly compute discrete Fourier transforms when the space and/or spectral domain data are unequally spaced. Outside CEM [63, 64], NUFFTs find applications in medical and radar imaging [65-68]. FGG drives its memory-efficiency from Gaussian-based interpolation schemes. Contrary to moment or far-field matching procedures, which produce discrete source constellations with spatial spectra that closely match the original currents' spectrum at low frequencies or on the Ewald sphere, the FGG was not designed with the AIM in mind and therefore produces spectra with errors that are rather uniformly distributed. The accuracy of the AIM-FGG hybrid therefore is typically somewhat less than that of an AIM solver that uses moment or far-field matching. For many applications, however, the dramatic memory savings of the method far outweigh this drawback.

This Chapter details the proposed AIM-FGG technique for accelerating the MOM-based solution of integral equations pertinent to the analysis of scattering from 3D composite structures. Section 3.2 summarizes AIM operations, details the FGG for mapping sources onto uniform AIM grids, and compares the latter to moment and field matching methods commonly used for the same purpose. Finally, numerical results that serve to validate and demonstrate the efficiency of the proposed acceleration are presented in Section 3.3.

3.2 Classical AIM

AIM reduces the memory and CPU requirements of MOM-based iterative integral equation (IE) solvers to $O(N_{\text{iter}}N_{\text{c}}\log N_{\text{c}})$, and $O(N_{\text{c}})+O(\gamma N)$, respectively. Here N_{c} is the number of nodes on the auxiliary AIM grid that encloses the structure D. The AIM achieves this efficiency by accelerating all matrix-vector multiplications pertinent to $\mathbf{Z}_p$, $p=1,...,M$ through exploitation of $g_p(\mathbf{r})$'s spatial translational invariance. Here, for the sake of simplicity in the formulation that follows a single penetrable object with surface S will be considered $(M=2)$, and the notation for the basis functions will be changed to $\mathbf{S}_n^e,\ n=1,...,N_1,\ e=1,...,N^b$.

When using the AIM, MOM matrices $\mathbf{Z}_p,\ p=1,\ 2$ are separated into near- and far-field components as

$$\mathbf{Z}_p=\mathbf{Z}_p^{\text{near}}+\mathbf{Z}_p^{\text{far}}. \tag{3.1}$$

The AIM accelerates matrix-vector multiplications involving $\mathbf{Z}_p^{\text{far}}$ by using point sources on the auxiliary AIM grid. Let $A_n^e(\mathbf{r})$ denote the integral

$$A_n^e(\mathbf{r})=\int_S \psi_n^e(\mathbf{r}')g_p(\mathbf{r}-\mathbf{r}')ds' \tag{3.2}$$

where $\psi_n^e(\mathbf{r}')$ represents $I_n^e \nabla' \cdot \mathbf{S}_n^e(\mathbf{r}')$, $K_n^e \nabla' \cdot \mathbf{S}_n^e(\mathbf{r}')$ or any Cartesian component of $I_n^e \mathbf{S}_n^e(\mathbf{r}')$ and $K_n^e \mathbf{S}_n^e(\mathbf{r}')$. Using an N^q point quadrature rule, (3.2) is approximated as

$$A_n^e(\mathbf{r}) \cong \sum_{i=1}^{N^q} \left[\psi_n^e\right]_i g(\mathbf{r} - \mathbf{r}_n^i), \tag{3.3}$$

with $\left[\psi_n^e\right]_i = \psi_n^e\left(\mathbf{r}_n^i\right) w_n^i$; here, and in (3.3), $\mathbf{r}_n^i = \hat{\mathbf{x}} x_n^i + \hat{\mathbf{y}} y_n^i + \hat{\mathbf{z}} z_n^i$ and w_n^i, $i = 1, ..., N_q$, are quadrature points and weights for the n^{th} triangle on surface S, respectively. The convolution theorem implies that (3.2) is equivalent to

$$A_n^e(\mathbf{r}) = \Im^{-1}\{\tilde{A}_n^e(\mathbf{k})\} = \Im^{-1}\left\{\Im\{g_p(\mathbf{r})\}\Im\{\psi_n^e(\mathbf{r})\}\right\} \tag{3.4}$$

where $\Im$ represents the continuous 3D Fourier transform. The Green function, evaluated on the uniform grid, is represented as a three level Toeplitz matrix which enables the use of 3D FFTs to perform these Fourier transforms efficiently. Evaluating (3.4) numerically using FFTs requires mapping of the nonuniform samples $\left[\psi_n^e\right]_i$, $i = 1, ..., N_q$, onto auxiliary sources residing on the uniform AIM grid and zero padding the AIM grid (at least doubling its size in each dimension) to avoid aliasing errors. The conventional methods used to perform this mapping, their shortcomings, and the proposed FGG are described later in this subsection.

The following three-step recipe summarizes the AIM: (i) $I_n^e \nabla' \cdot \mathbf{S}_n^e(\mathbf{r}')$ and all three Cartesian components of $I_n^e \mathbf{S}_n^e(\mathbf{r}')$ are mapped onto the uniform AIM grid for all n and e. (ii) The fields $\mathcal{L}_p \mathbf{J}_p$ and $\mathcal{L}_p \mathbf{M}_p$, $p = 1, 2$ on the grid due to these auxiliary AIM sources are computed using global FFTs. After $\mathcal{L}_p \mathbf{J}_p$ and $\mathcal{L}_p \mathbf{M}_p$ are computed, $\mathcal{K}_p \mathbf{J}_p$ and $\mathcal{K}_p \mathbf{M}_p$ are approximated using finite differences evaluated on the AIM grid [69]. (iii) Finally, $\mathcal{L}_p \mathbf{J}_p$ and $\mathcal{L}_p \mathbf{M}_p$ along with $\mathcal{K}_p \mathbf{J}_p$ and $\mathcal{K}_p \mathbf{M}_p$ are mapped back onto the basis functions and testing integrals are computed. In (3.1), $\mathbf{Z}_p^{\text{near}}$ is a sparse matrix that stores pre-corrected near-field interactions; its entries are computed using the formulation described in Chapter 2 and corrected for errors introduced by the use of the global FFTs

used in the matrix-vector multiplications involving $\mathbf{Z}_p^{\text{far}}$. The $O(N_{\text{iter}} N_{\text{c}} \log N_{\text{c}})$ computational cost is due to all global FFTs, and dominates the $O\left(N_{\text{iter}} N\right)$ cost of the matrix vector multiplications pertinent to $\mathbf{Z}_p^{\text{near}}$; the $O(N_{\text{c}}) + \gamma O(N)$ memory requirements are due to the storage of fields and currents on the AIM grid and the mapping coefficients required in steps (i) and (iii).

The parameter γ depends on the actual method used for computing the AIM mapping coefficients. Two commonly used methods are moment and field matching. The moment matching (MM) method [17] maps each actual source onto the auxiliary AIM grid by solving a linear system of equations that equates the source's moments to those of the closest $\mathcal{M}^3$ AIM sources -- $\mathcal{M}$ is the linear dimension of the AIM sub-grid a source maps onto. Field matching achieves the same by equating far-field signatures [18, 56]. Typically, when using MM and field matching, mapping coefficients are computed once and stored in memory because computing them on the fly during the iterative solution process would be too time consuming. The mapping of each source using pre-computed coefficients requires $\mathcal{M}^3$ multiplications and additions. Due to the storage of these coefficients γ scales as $O\left(N^b \mathcal{M}^3\right)$ in these methods. For large M and N^b (higher order basis functions) this storage dominates that of fields on the AIM grid – this is especially so for quasi-planar and volumetric scatterers. Below, a memory efficient technique to perform AIM mappings is described.

3.3 Fast Gaussian Gridding

This subsection elucidates the incorporation of the FGG into the AIM framework. Interested readers are referred to [22] for a detailed description of the FGG. The usage of FGG in AIM is justified by observing that steps (i) and (ii) of the AIM lead to an approximation of the uniformly sampled Fourier transform of $\mathbf{J}(\mathbf{r})$ and $\mathbf{M}(\mathbf{r})$ that is

highly accurate for spatial frequencies in or near the Ewald sphere (implying highly accurate "far-field" representations). This operation also can be performed by NUFFT algorithms, even though they deliver spectra that are accurate even beyond the Ewald sphere (which is of no use for AIM purposes). FGG is an NUFFT algorithm that is particularly memory efficient; it achieves this efficiency leveraging a Gaussian-based interpolation/convolution technique as described next. The AIM-FGG hybrid convolves the nonuniform surface current samples $\left[\psi_n^e\right]_i$ with a 3D Gaussian, then samples the resulting continuous (and periodic) function on the AIM uniform grid points to obtain FGG auxiliary sources. That is, the $\left[\psi_n^e\right]_i$ are interpolated/spread onto the uniform grid using a Gaussian kernel; it will be demonstrated below that this can be achieved efficiently by storing only four exponentials per source. The FFTs of the auxiliary sources thus obtained result in the Fourier transform of the original sources multiplied by that of the Gaussian convolution kernel. An approximation to the original transform is obtained upon dividing the transform of the FGG auxiliary sources by the transform of the Gaussian. Step (iii) of the AIM is also performed by FGG, this time to obtain the nonuniform samples (at points dictated by the testing integral) of $\mathcal{L}_p$ and $\mathcal{K}_p$ from the uniform samples in transform domain. In the remainder of this subsection a more formal and mathematical description of AIM-FGG is presented.

Let $H(\mathbf{r})$ represent the separable function

$$H(\mathbf{r}) = h(x, T_x, \tau_x)h(y, T_y, \tau_y)h(z, T_z, \tau_z), \tag{3.5}$$

where

$$h(t, T, \tau) = \sum_{l=-\infty}^{\infty} e^{-(t-lT)^2/4\tau} \tag{3.6}$$

is a periodic one dimensional Gaussian function, T_x, T_y, and T_z are $H(\mathbf{r})$'s periodicity and τ_x, τ_y, and τ_z are measures of its width along x, y, and z. Note that Gaussians are

highly peaked and T_x, T_y, and T_z are set to the extent of the AIM grid. That is, only a single period of the periodic Gaussian function has to be considered. The spreading of the actual sources is expressed by the convolution

$$\hat{\psi}_s(\mathbf{r}) = \psi_s(\mathbf{r}) * \left[H(\mathbf{r}) \Pi_{3D}(\mathbf{r}) \right], \tag{3.7}$$

where

$$\psi_s(\mathbf{r}) = \sum_{n=1}^{N_1} \sum_{e=1}^{N^b} \sum_{i=1}^{N_q} \left[\psi_n^e \right]_i \delta(\mathbf{r} - \mathbf{r}_n^i). \tag{3.8}$$

In (3.7), the 3D Gaussian $H(\mathbf{r})$ is truncated by the rectangular function $\Pi_{3D}(\mathbf{r})$

$$\Pi_{3D}(\mathbf{r}) = \Pi\left(\frac{x}{\mathcal{M}\Delta x} \right) \Pi\left(\frac{y}{\mathcal{M}\Delta y} \right) \Pi\left(\frac{z}{\mathcal{M}\Delta z} \right), \tag{3.9}$$

where $\Delta x, \Delta y,$ and Δz represent the AIM grid sizes along $x, y,$ and z, respectively, and

$$\Pi(t) = \begin{cases} 1 & -0.5 < t \le 0.5 \\ 0 & otherwise \end{cases}. \tag{3.10}$$

The values of the AIM sources are obtained by sampling $\hat{\psi}_s(\mathbf{r})$ at the regular grid points $\mathbf{r} = \hat{\mathbf{x}} n_x \Delta x + \hat{\mathbf{y}} n_y \Delta y + \hat{\mathbf{z}} n_z \Delta z$, where (n_x, n_y, n_z) represent discrete coordinates on the grid. Note that due to the truncation of the Gaussian, each source does not spread across the entire AIM grid but is limited to the closest $\mathcal{M}$ nodes in each dimension. Just like other NUFFT algorithms the main source of error in the FGG results from spatial truncation and spectral aliasing due to the finite rate at which $\hat{\psi}_s(\mathbf{r})$ is sampled [70]. For each $\mathcal{M}$ the optimum values of τ_x, τ_y, and τ_z to minimize this error are easily found by a numerical search.

In the FGG scheme computing the convolution in (3.7) requires the storage of only 4 mapping coefficients per nonuniform sample point $\mathbf{r}_n^i$. These coefficients are obtained by factorizing the Gaussians in (3.7) as

$$e^{-\left(n_x\Delta x-x_k^i\right)^2/4\tau_x}e^{-\left(n_y\Delta y-y_k^i\right)^2/4\tau_y}e^{-\left(n_z\Delta z-z_k^i\right)^2/4\tau_z}=$$
$$e^{-\left(\left(x_k^i\right)^2/4\tau_x+\left(y_k^i\right)^2/4\tau_y+\left(z_k^i\right)^2/4\tau_z\right)}\left(e^{x_k^i\Delta x/\tau_x}\right)^{n_x}\left(e^{y_k^i\Delta y/\tau_y}\right)^{n_y}\left(e^{z_k^i\Delta z/\tau_z}\right)^{n_z}e^{-(n_x\Delta x)^2/4\tau_x}e^{-\left(n_y\Delta y\right)^2/4\tau_y}e^{-(n_z\Delta z)^2/4\tau_z}. \quad (3.11)$$

The exponentials $e^{-\left(\left(x_k^i\right)^2/4\tau_x+\left(y_k^i\right)^2/4\tau_y+\left(z_k^i\right)^2/4\tau_z\right)}$, $e^{x_k^i\Delta x/\tau_x}$, $e^{y_k^i\Delta y/\tau_y}$, and $e^{z_k^i\Delta z/\tau_z}$ are the mapping-coefficients that are computed and stored for each point $\mathbf{r}_n^i$. The last three exponentials in (3.11) are the same for all $\mathbf{r}_n^i$, so they are computed only once. After carefully arranging the loops, the spreading from $\mathbf{r}_n^i$, to the closest $\mathcal{M}^3$ nodes is achieved with minimum number of arithmetical operations ($\mathcal{M}^3$ multiplications and additions) using these coefficients. Then, a 3D FFT is performed on the interpolated AIM sources. The spectrum of these sources is corrected for the smoothing introduced by the Gaussians to retrieve the original spectrum. This correction is basically a deconvolution operation performed by dividing the spectrum of the sources by (an approximation to) $H(\mathbf{r})$'s spectrum

$$\tilde{H}\left(\tilde{\mathbf{k}}\right)=\tilde{h}\left(\tilde{k}_x,T_x,\tau_x\right)\tilde{h}\left(\tilde{k}_y,T_y,\tau_y\right)\tilde{h}\left(\tilde{k}_z,T_z,\tau_z\right), \quad (3.12)$$

where

$$\tilde{h}(k,T,\tau)=\frac{\sqrt{4\pi\tau}}{T}e^{-(2\pi k/T)^2\tau}, \quad (3.13)$$

and $\tilde{\mathbf{k}}=\left(\tilde{k}_x,\tilde{k}_y,\tilde{k}_z\right)$, $\tilde{k}_x=1,2,...,N_x$, $\tilde{k}_y=1,2,...,N_y$, and $\tilde{k}_z=1,2,...,N_z$. Here, N_x, N_y and N_z are the number of nodes on the AIM grid in each dimension ($N_c=N_x\times N_y\times N_z$).

The entire FGG algorithm can be captured as follows: (i) For each element $n=1,...,N_1$ and quadrature point $i=1,...,N_q$, compute and store the mapping coefficients $\left(C_1,\ C_{2x},\ C_{2y},\ C_{2z}\right)$,

$$C_1=e^{-\left(\left(x_k^i-\xi_{k,x}^i\right)^2/4\tau_x+\left(y_k^i-\xi_{k,y}^i\right)^2/4\tau_y+\left(z_k^i-\xi_{k,z}^i\right)^2/4\tau_z\right)}, \quad (3.14)$$

$$C_{2x}=e^{\left(x_k^i-\xi_{k,x}^i\right)\Delta x/\tau_x},\ \mathrm{C}_{2y}=e^{\left(y_k^i-\xi_{k,y}^i\right)\Delta y/\tau_y},\ \text{and}\ \mathrm{C}_{2z}=e^{\left(z_k^i-\xi_{k,z}^i\right)\Delta z/\tau_z}, \quad (3.15)$$

where $\boldsymbol{\xi}_k^i = \left(\xi_{k,x}^i, \xi_{k,y}^i, \xi_{k,z}^i\right)$ are the discrete coordinates of the grid point closest to $\mathbf{r}_n^i$. Also compute and store the exponentials:

$$C_{3x}(p) = e^{-(p\Delta x)^2/4\tau_x},\ \mathrm{C}_{3y}(p) = e^{-(p\Delta y)^2/4\tau_y}, \text{ and } \mathrm{C}_{3z}(p) = e^{-(p\Delta z)^2/4\tau_z}, \tag{3.16}$$

where $p = -\mathcal{M}/2+1,...,\mathcal{M}/2$. (ii) Map each source onto the AIM grid: let $\left(\xi_{k,x}^i + p,\ \xi_{k,y}^i + q,\ \xi_{k,z}^i + r\right)$, $p = -\mathcal{M}/2+1,...,\mathcal{M}/2$, $q = -\mathcal{M}/2+1,...,\mathcal{M}/2$, $r = -\mathcal{M}/2+1,...,\mathcal{M}/2$, represent the discrete coordinates of the $\mathcal{M}^3$ AIM sources closest to the actual sources at $\mathbf{r}_n^i$ having the magnitudes $\Sigma_{e=1}^{N^b} I_n^e \left[\psi_n^e\right]_i$ and $\Sigma_{e=1}^{N^b} K_n^e \left[\psi_n^e\right]_i$. Then the contributions of actual sources to these AIM sources $\left(V_{pqr}\right)$ are obtained using the pre-computed mapping coefficients as

$$V_{pqr} = V_0 \left(C_{2x}\right)^p C_{3x}\left(p\right)\left(C_{2y}\right)^q C_{3y}\left(q\right)\left(C_{2z}\right)^r C_{3z}\left(r\right), \tag{3.17}$$

where $V_0 = C_1 \Sigma_{e=1}^{N^b} I_n^e \left[\psi_n^e\right]_i$ or $V_0 = C_1 \Sigma_{e=1}^{N^b} K_n^e \left[\psi_n^e\right]_i$. (iii) Obtain the spectrum of the original sources: After taking the 3D Fourier transform of the AIM sources the correction is made by simply dividing by $\tilde{H}(\tilde{\mathbf{k}})$.

To map the fields back onto the basis functions (step (iii) of the AIM), the FGG is performed again, this time to smear out the fields on the grid to the nonuniform points on the basis functions. To this end, step (ii) of the original AIM is slightly modified. First the spectrum of the corrected sources is multiplied with that of the Green's function to compute $A(\mathbf{r})$'s spectrum $\tilde{A}(\tilde{\mathbf{k}})$ as in the original AIM. Then, $\tilde{A}(\tilde{\mathbf{k}})$ is divided by $\tilde{H}(\tilde{\mathbf{k}})$ to pre-correct the effect of Gaussian smoothing in the final mapping. After that, a 3D inverse FFT is performed on the pre-corrected $\tilde{A}(\tilde{\mathbf{k}})$. Finally, the resulting pre-corrected fields on the uniform AIM grid are mapped onto the nonuniformly distributed quadrature points of the testing integrals using the same FGG scheme. Note that, when using the same quadrature rules for the source and testing integrals, the 4 mapping coefficients used in the forward and backward mapping are identical. That is, they can be used in both operations.

In classical AIM [17], which uses far-field or moment matching, the memory required for storing mapping coefficients scales as $O\left(N^{\mathrm{b}}\mathcal{M}^3\right)$. When AIM-FGG is used, the memory required for storing mapping coefficient is of $O(1)$; it only stores four real numbers for each quadrature point being mapped. AIM-FGG has more pronounced benefits when it is applied to high-order current expansions (e.g., $N^{\mathrm{b}} = 8/15$, for 1^{st} / 2^{nd} order expansion) since the number of quadrature points used to compute source and test integrals in the far-field interactions only weakly increase with order of current expansion. Additionally, since the same basis functions are used for expanding $\mathbf{M}(\mathbf{r})$ and $\mathbf{J}(\mathbf{r})$, no additional memory is needed even though the number of unknowns is doubled in the MOM system.

3.4 Numerical Results

This section presents numerical results that serve to validate the accuracy and demonstrate the efficiency of the AIM-FGG hybrid. First, the accuracy of FGG mapping is investigated and compared to that of MM methods. Next, scattering from some benchmark radar targets, viz. a plate, a double ogive, and PEC and dielectric spheres is analyzed using AIM-FGG accelerated solvers, and the results compared to those obtained using nonaccelerated SIE solvers, published measurements, and analytical solutions. Then, scattering from a more complex structure, namely a Humvee model, is analyzed. Finally, radiation pattern of a dielectric rod antenna is analyzed and the results are compared to published measurements.

3.4.1 FGG Mapping Accuracy

To characterize the accuracy of FGG mapping, consider the CFIE matrix element due to the two basis functions defined on the triangles shown in Fig. 3.1. The CFIE

interaction element versus distance between the triangle pairs is computed using both the AIM-FGG and AIM-MM for increasing $\mathcal{M}$. The relative error Δ^{AIM} is defined as

$$\Delta^{AIM} = \left| \frac{\mathbf{Z}^{AIM}(1,2) - \mathbf{Z}(1,2)}{\mathbf{Z}(1,2)} \right|, \tag{3.18}$$

where $\mathbf{Z}(1,2)$ is computed classically, and $\mathbf{Z}^{AIM}$ is obtained using either AIM-FGG or AIM-MM. Fig. 3.2 shows the relative error Δ^{AIM} versus inter-basis function distance. The free space wavelength λ_0 is 50 m and the CFIE constant α is set to 0.6. The AIM grid size along each dimension is 5 m, i.e. $\Delta x = \Delta y = \Delta z = 5$ m. The curl of the vector potential on the AIM grid is computed using a fourth-order accurate finite difference formula. It is observed that while FGG delivers high accuracy, MM is more accurate for any given $\mathcal{M}$. This is due to differences in the spectral approximations inherent in both methods. To demonstrate this difference, the Fourier transform of a single point source is computed using the FGG and MM and then compared to the exact transform, i.e. a constant over the whole k-space. Fig. 3.3 shows the relative error versus k_x $\left(k_y = k_z = 0\right)$ for different $\mathcal{M}$. The accuracy of MM is very high around $k_x = 0$ but decreases rapidly for increasing k_x. In contrast, FGG is less accurate for small k_x but its accuracy decreases slower than that of MM. That said, on the Ewald sphere (defined by $k_x^2 + k_y^2 + k_z^2 = k_0^2$) MM is more accurate than FGG irrespective the choice of $\mathcal{M}$ -- this explains why AIM-MM is more accurate than AIM-FGG for the same $\mathcal{M}$. Furthermore in [56] it is shown that far-field matching is often more accurate than MM, which suggest that on the Ewald sphere far-field matching is even more accurate. We note, however, that accuracy is far less of an issue in AIM-FGG than it is in AIM-MM or AIM-FMM as M can be increased (and along with it, accuracy) without requiring extra memory. The next sections will demonstrate that the small sacrifice in accuracy associated with FGG mapping is more than compensated for by its large memory savings.

3.4.2 Scattering from PEC Plates

To illustrate the dependence of the AIM accuracy on grid size $(\Delta x = \Delta y = \Delta z)$, and $\mathcal{M}$, the radar cross section (RCS) of a $15\,\text{cm} \times 15\,\text{cm}$ PEC plate is computed by solving the EFIE ($\alpha = 0$). The excitation frequency is 26.3 GHz, corresponding to a free-space wavelength of $\lambda_0 = 1.14\,\text{cm}$, and $N = 59{,}134$. In this and the following examples, the AIM near-field region comprises a sphere of radius of $\lambda_0/2$. The plate is illuminated by a plane-wave

$$\mathbf{E}^i = \hat{\mathbf{p}} e^{-jk_0 \hat{\mathbf{k}} \mathbf{r}}, \tag{3.19}$$

where $\hat{\mathbf{p}} = -\cos(45°)\hat{\mathbf{x}} + \sin(45°)\hat{\mathbf{z}}$ and $\hat{\mathbf{k}} = -\sin(45°)\hat{\mathbf{x}} - \cos(45°)\hat{\mathbf{z}}$. Fig. 3.4 shows the relative root-mean-square (RMS) RCS error versus the AIM grid size for various $\mathcal{M}$; the RMS error is defined as

$$\text{RMS Error} = \frac{\sqrt{\sum_{i=1}^{N_s} \left| \sigma^{AIM}(\theta_i, \phi_i) - \sigma(\theta_i, \phi_i) \right|^2}}{\sqrt{\sum_{i=1}^{N_s} \sigma(\theta_i, \phi_i)^2}} \tag{3.20}$$

where σ^{AIM} and σ represent the bi-static RCS obtained by AIM accelerated and nonaccelerated EFIE solvers, respectively. In (3.20) N_s is the total number of observation angles (θ_i) in E- ($\phi_i = 0°$) and H- ($\phi_i = 90°$) planes at which the RCS is sampled. As it was observed in the previous paragraph, while the AIM-FGG is highly accurate, AIM-MM is more accurate for any given grid size and $\mathcal{M}$. Note that the RMS error decreases with the AIM grid size or increases in $\mathcal{M}$, in both methods.

The sacrifice in accuracy associated with the AIM-FGG hybrid dwarfs in comparison with the memory savings the method realizes. To illustrate this, assume the plate's side length changes while the excitation, average mesh density (in unknowns per square wavelength), and AIM parameters are kept constant. Fig. 3.5(a) shows the FFT, FGG, and MM memory requirements, versus N. These graphs are characteristic of all planar

scatterers; note, in particular that the FFT storage requirements scale as $O(N_c) = O(N)$. The memory requirements of the FGG are independent of M, and smaller than the FFT storage requirements. The same is not true for MM: as soon as $\mathcal{M} = 4$ the storage requirements associated with the mapping exceed those associated with the FFT operations.

Next, computational complexity, memory requirement, and the parallel efficiency of the proposed scheme are evaluated. Consider a rectangular PEC plate with edge lengths $0.1778\ \text{m} \times 0.1016\ \text{m}$ in $x-$ and $y-$ direction. The plate is illuminated by a $\hat{\mathbf{p}} = \hat{\mathbf{x}}$ polarized plane-wave propagating in $\hat{\mathbf{k}} = \hat{\mathbf{z}}$ direction. EM scattering from the plate is analyzed using the AIM-FGG accelerated EFIE solver. A series of simulations are carried out by increasing the frequency of this excitation. In each case a new mesh is generated to keep the average mesh density (in unknowns per square wavelength) constant. λ_0, N, N_c, and N_{iter} in the simulations are given in Table 3.1. In all simulations aim grid size $(\Delta x = \Delta y = \Delta z)$ is set to $\lambda_0/20$ and $\mathcal{M} = 6$. Each simulation is repeated by utilizing increasing number of processors to assess the parallel efficiency. Figs. 3.6 (a) and 3.7 (a) show the matrix-vector multiplication time in the iterative solver and the memory requirement per processor versus number of processors in the simulations. Dashed lines in the figures are ideal speed-up tangents. Matrix-vector multiplication time (when utilizing 24 processors) versus N is plotted in Fig. 3.6 (b). Fig. 3.7 (b) depicts the corresponding measured peak memory over all processors, which includes the operating system overhead. Lines corresponding to theoretical $O(N \log N)$ and $O(N)$ complexity are also plotted in Figs. 3.6 (b) and 3.7 (b), respectively.

3.4.3 Monostatic RCS of a Metallic Double Ogive

Next, scattering from a PEC double ogive, an electromagnetic code consortium (EMCC) benchmark target [71], is analyzed using the CFIE solver accelerated via the

AIM-FGG and the results are compared to those obtained using a nonaccelerated CFIE solver and measurements data [71]. The double ogive comprises two sections of lengths 6.35 cm and 12.7 cm and tip angles $46.4°$ and $22.62°$. The excitation frequency is 9 GHz, $N = 10{,}536,$ and $\alpha = 0.6.$ In this simulation $\Delta x = \Delta y = \Delta z =$ 2.1 cm, $M = 6,$ and $N_c = 196 \times 64 \times 64$. Figs. 3.8 (a) and (b) show the double ogive's monostatic RCS for the HH- and VV-polarizations, respectively; the elevation angle is zero in both cases. The FFT and FGG require 36.7 MB and 2.5 MB of storage, respectively. When using MM instead of FGG with the same parameters, the mapping coefficient storage cost increases to 135 MB, and thus exceeds the FFT storage requirements.

λ_0	N	N_c	N_{iter}
25.4 m	9,830	$294 \times 180 \times 12$	580
20.0 m	15,307	$378 \times 216 \times 12$	642
10.0 m	62,105	$750 \times 420 \times 12$	722
7.4 mm	109,698	$960 \times 560 \times 12$	856
4.9 mm	249,035	$1440 \times 840 \times 12$	1,083
2.4 mm	1,191,782	$3136 \times 1792 \times 12$	2,485

Table 3.1: Free-space wavelength λ_0, number of unknowns $N,$ aim grid dimensions $N_c,$ and number of iterations N_{iter} in PEC plate simulations.

3.4.4 Scattering from PEC Spheres

The bistatic RCS of a PEC sphere of radius 2 m is computed using an AIM-FGG-accelerated CFIE solver and compared to the Mie series solution. The sphere is illuminated by a plane wave with $\hat{\mathbf{p}} = \hat{\mathbf{x}}$ and $\hat{\mathbf{k}} = \hat{\mathbf{z}}.$ The frequency of excitation is 1 GHz, $N = 263{,}667,$ and $\alpha = 0.6.$ The curl of the vector potential on the AIM grid is computed

using a fourth-order accurate finite difference formula. In this simulation $\Delta x = \Delta y = \Delta z =$ 2.5 cm, $M = 6,$ and $N_c = 350 \times 350 \times 350.$ Figs. 3.9 (a) and (b) show the bistatic RCS of the sphere in E-plane ($\phi = 0°$) and H-plane ($\phi = 90°$), respectively. For these parameters the FFT and FGG require 2.4 GB and 86 MB of storage; MM requires 4.5 GB.

Next, assume that the sphere dimensions change while the excitation, average mesh density (in unknowns per square wavelength), and AIM parameters are kept constant. Fig. 5(b) shows the FFT, FGG, and MM memory requirements, versus N. These graphs are characteristic of all non-planar scatterers; note, in particular that the FFT storage requirements scale as $O(N_c) = O(N^{1.5})$. Although the MM storage requirements do not dominate those associated with the FFT for large N, using FGG saves significant memory resources and permits the use of AIM on structures larger than possible with an AIM-MM solver.

To demonstrate the computational complexity, memory requirement, and the parallel efficiency of the proposed scheme a PEC sphere of radius 1 m is considered. The sphere is illuminated by an $\hat{\mathbf{x}}$ polarized plane-wave propagating in the $z-$direction. EM scattering from the sphere is analyzed using the AIM-FGG accelerated EFIE solver. A series of simulations are carried out by increasing the frequency of this excitation. In each case a new mesh is generated to keep the average mesh density (in unknowns per square wavelength) constant. λ_0, N, N_c, and N_{iter} in the simulations are given in Table 3.2. Each simulation is repeated by utilizing increasing number of processors to assess the parallel efficiency. Figs. 3.10 (a) and 3.11 (a) show the matrix-vector multiplication time in the iterative solver and the memory requirement (per processor) versus number of processors in the simulations. Dashed lines in the figures are ideal speed-up tangents. Matrix-vector multiplication time (when utilizing 24 processors) versus N is plotted in Fig. 3.10 (b). Fig. 3.11 (b) depicts the corresponding measured peak memory over all

processors, which includes the operating system overhead. Lines corresponding to theoretical $O\left(N^{1.5}\log N\right)$ and $O\left(N^{1.5}\right)$ complexity are also plotted in Figs. 3.10 (b) and 3.11 (b), respectively.

3.4.5 Bistatic RCS of a Dielectric Sphere

The proposed AIM-FGG accelerated PMCHWT solver is used in the analysis of scattering from a dielectric sphere of radius 2 m, with $\varepsilon_r = 2.5 - j0.5$. The sphere is illuminated by an $\hat{\mathbf{x}}$ polarized plane wave propagating in $z-$direction at $f = 1.5$ GHz. Two simulations are performed: In the first one, the currents on the sphere are expanded using 837,618 zeroth-order basis functions, where as in the second one only 92,080 first-order basis functions are used for the same purpose. In both simulations the surface of the sphere is discretized using curvilinear elements. Fig. 3.12 shows that both solutions practically have the same accuracy even though the high-order method requires far fewer unknowns.

λ_0	N	N_c	N_{iter}
0.8 m	6,924	$120\times120\times120$	493
0.5 m	21,399	$192\times192\times192$	1,012
0.32 m	47,556	$280\times280\times280$	2,500
0.22 m	103,809	$420\times420\times420$	2,134
0.16 m	184,080	$540\times540\times540$	3,060

Table 3.2: Free-space wavelength λ_0, number of unknowns N, aim grid dimensions N_c, and number of iterations N_{iter} in PEC sphere simulations.

3.4.6 Scattering from a Humvee

Next a more realistic geometry is considered. Scattering from an all-PEC model of a Humvee [Fig. 3.13 (a)] is analyzed using an AIM-FGG-accelerated hybrid EFIE-CFIE solver. The EFIE is applied on the main body of the Humvee, which is an open surface, while the CFIE is applied on the tires, which are closed surfaces. The Humvee fits in a box of dimensions $5.14\ \text{m} \times 2.44\ \text{m} \times 1.6\ \text{m}$ and is illuminated by an incident plane wave with $\hat{\mathbf{p}} = \hat{\mathbf{y}}$, $\hat{\mathbf{k}} = -\cos(45°)\hat{\mathbf{x}} - \sin(45°)\hat{\mathbf{z}}$ of frequency 1 GHz; the discrete model involves $N = 151,026$ unknowns. In this simulation $\Delta x = \Delta y = \Delta z =$ 1.875 cm, $M = 4$, $N_c = 560 \times 270 \times 250$, and $\alpha = 0.6$ for the CFIE. Figs. 3.13 (b) and (c) show the real and imaginary parts of the surface current. The storage of the matrices and vectors for the FFT and the FGG mapping coefficients requires 1.7 GB and 75 MB, respectively. Once again the FGG requires far less memory than the MM, which needs roughly 1.2 GB to store mapping coefficients.

3.4.7 Radiation Pattern of a Dielectric Rod Antenna

The proposed solver is used in the characterization of a dielectric rod antenna [72], with $\varepsilon_r = 2.1$ and a loss tangent $\tan\delta = 3 \times 10^{-4}$. The end of the rod is coated with an antireflective layer ($\varepsilon_r = 1.45$). The antenna is fed by a rectangular PEC waveguide at $f = 9\ \text{GHz}$ (Fig. 3.14(a)). The current on the PEC and dielectric surfaces are expanded using 14,846 first-order basis functions. Fig. 3.14 (b) shows the real and imaginary parts of the surface current. Fig. 3.15 (a)-(b) shows that the radiation pattern computed by the proposed solver agrees well with the measurement data presented in [72].

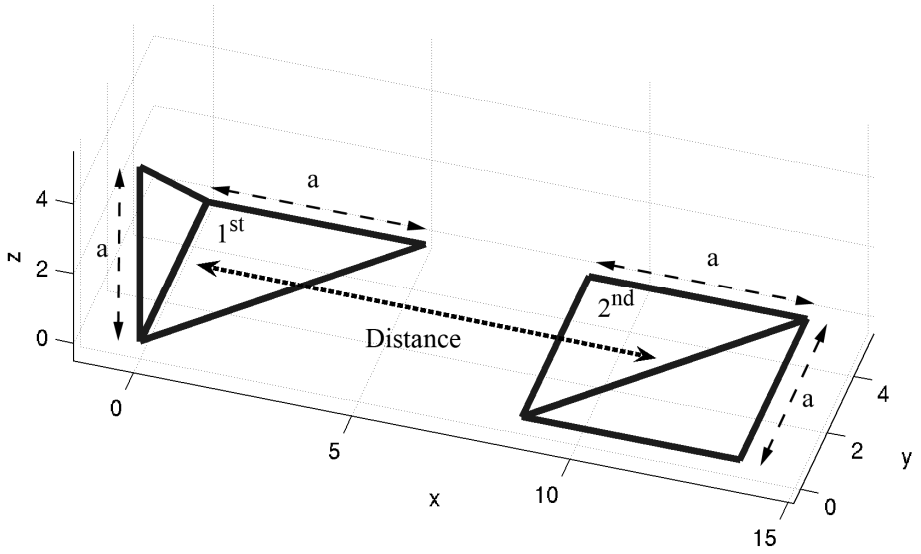

Figure 3.1: Two RWG basis functions; the "distance" between them is defined as that between the mid-points of their defining edges.

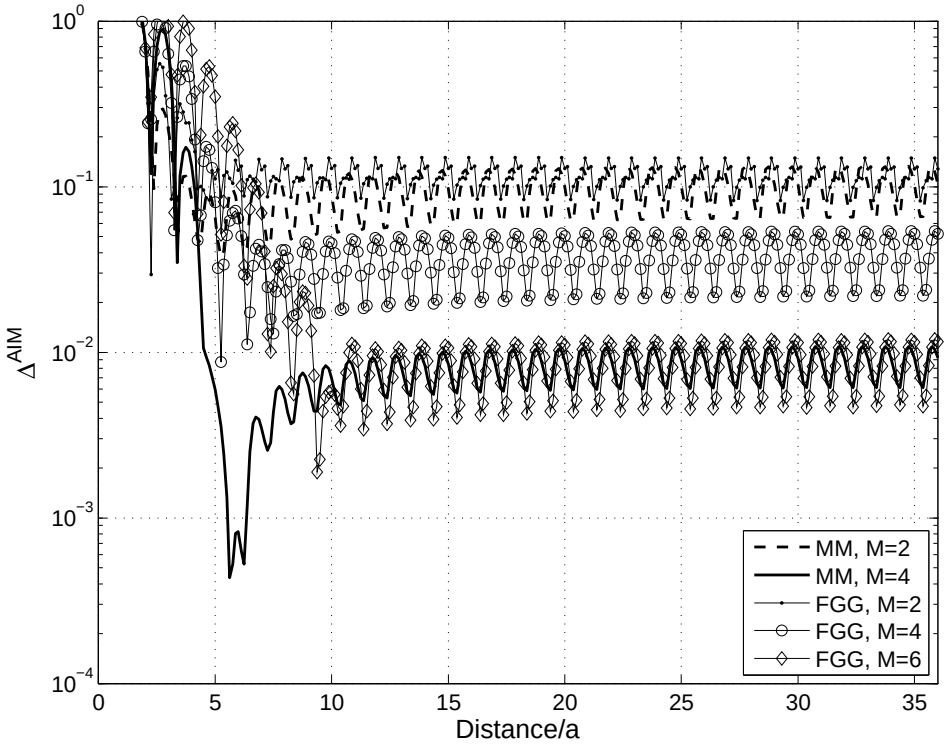

Figure 3.2: Relative error versus "distance/a" between basis functions. "Distance" and "a" are illustrated in Fig. 1.

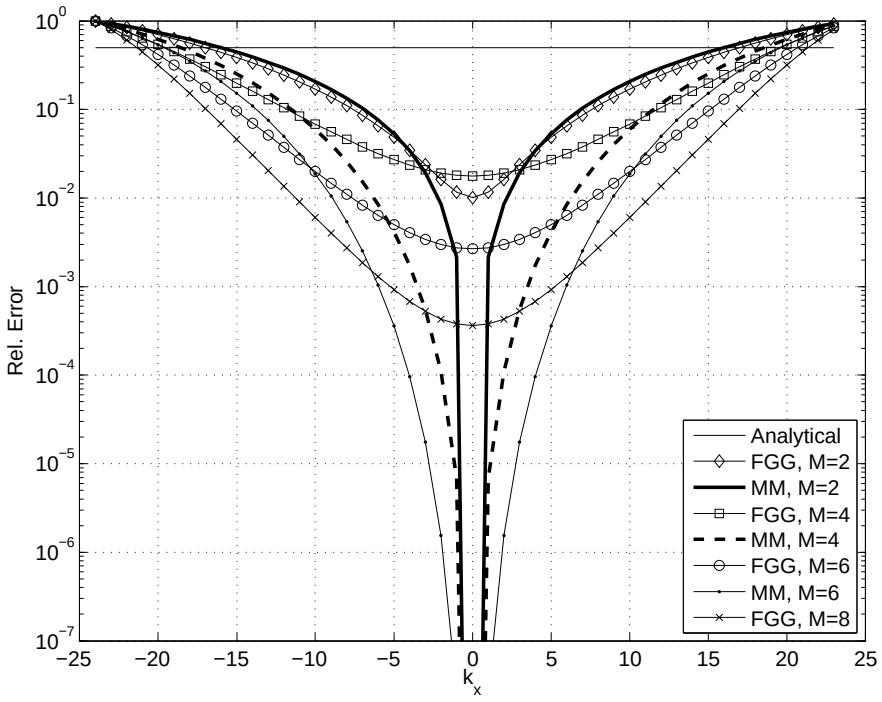

Figure 3.3: Relative error in the Fourier transform of a single dipole versus k_x $\left(k_y = k_z = 0\right)$

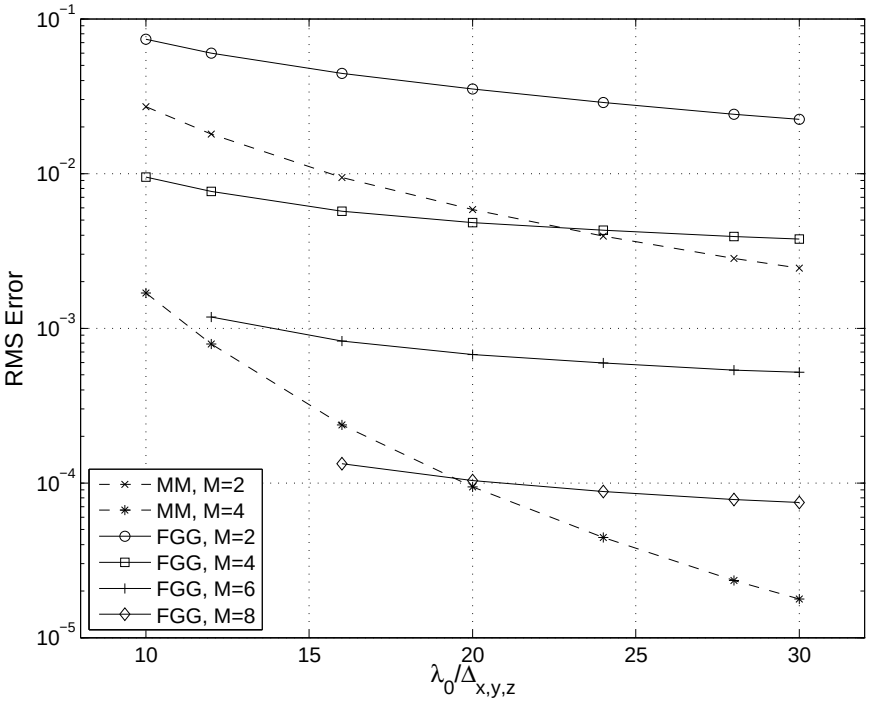

Figure 3.4: RMS error in the RCS of a PEC plate versus AIM grid size for various $\mathcal{M}$

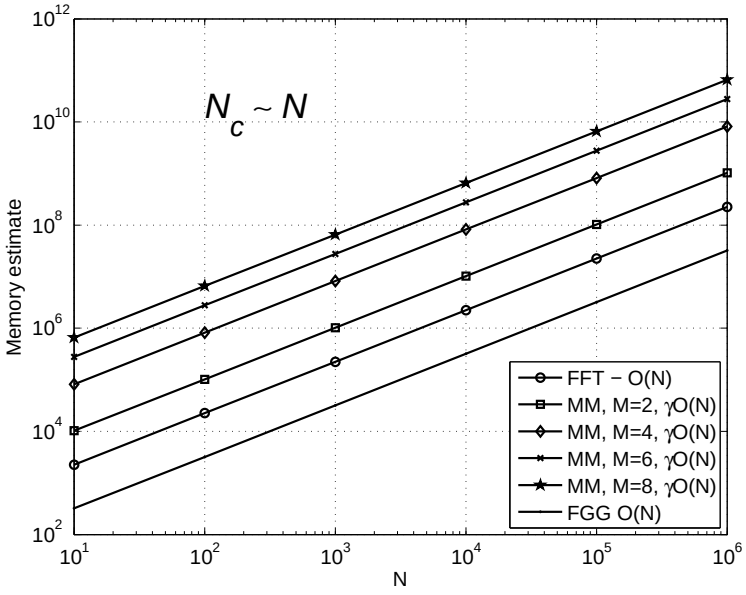

(a)

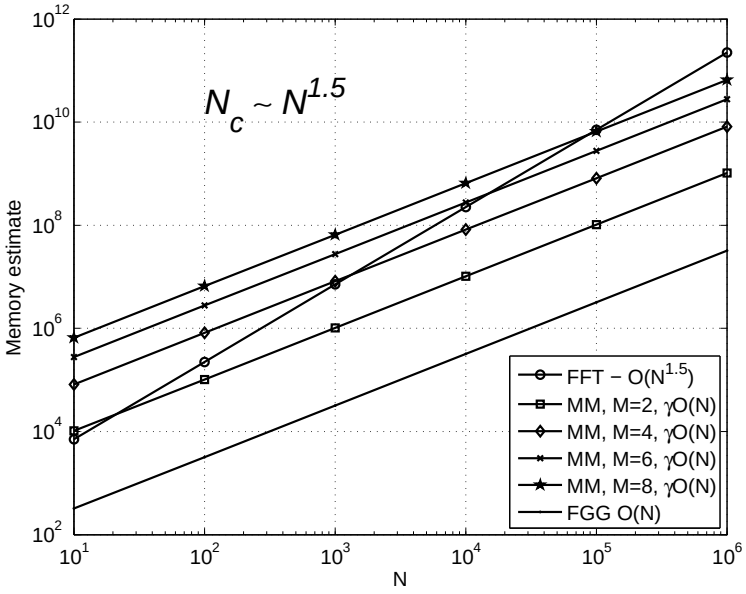

(b)

Figure 3.5: Estimated memory storage requirements of auxiliary AIM sources (denoted by FFT), MM and FGG mapping coefficients for different $\mathcal{M}$ versus N for (a) volumetric and quasi-planar (b) arbitrary 3D surface scatterers.

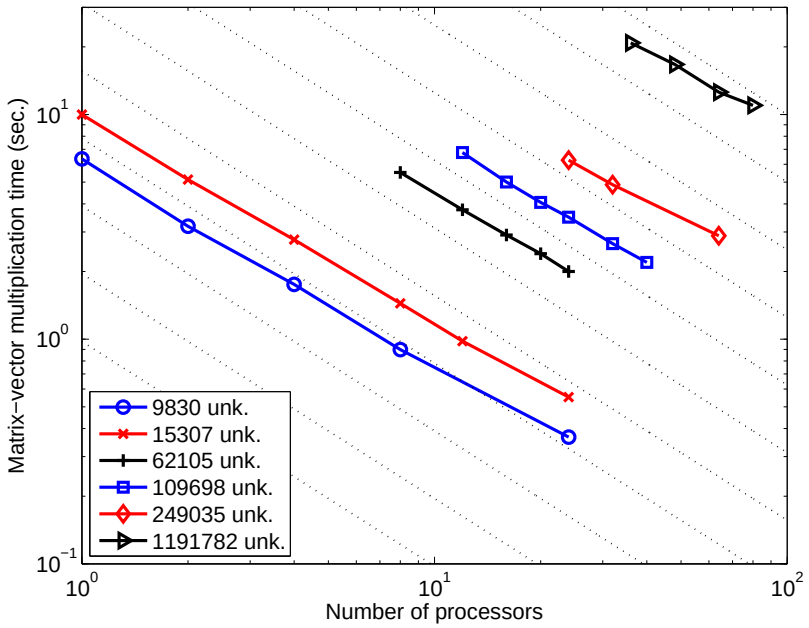

(a)

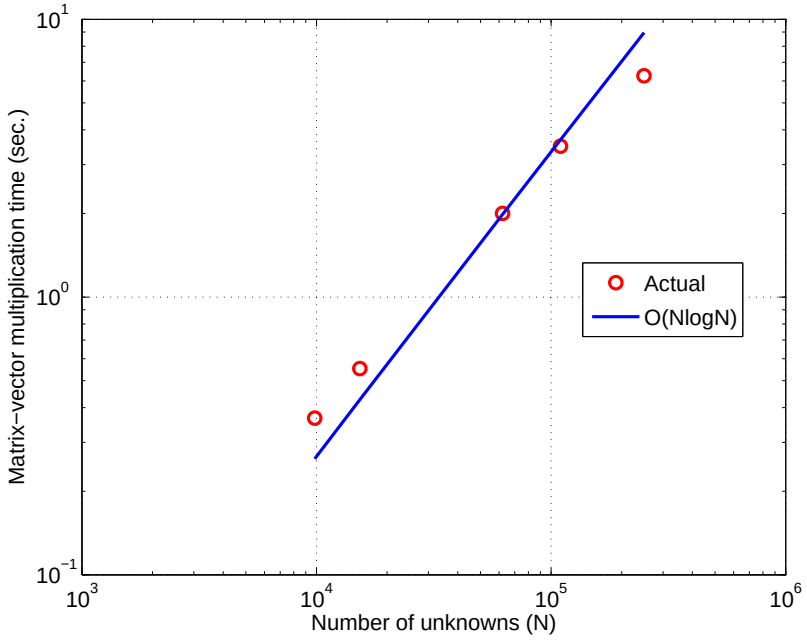

(b)

Figure 3.6: (a) Matrix-vector multiplication time versus number of processors for PEC plate example. Dashed lines are ideal speed-up tangents. (b) Matrix-vector multiplication time versus N when simulations are executed on 24 processors.

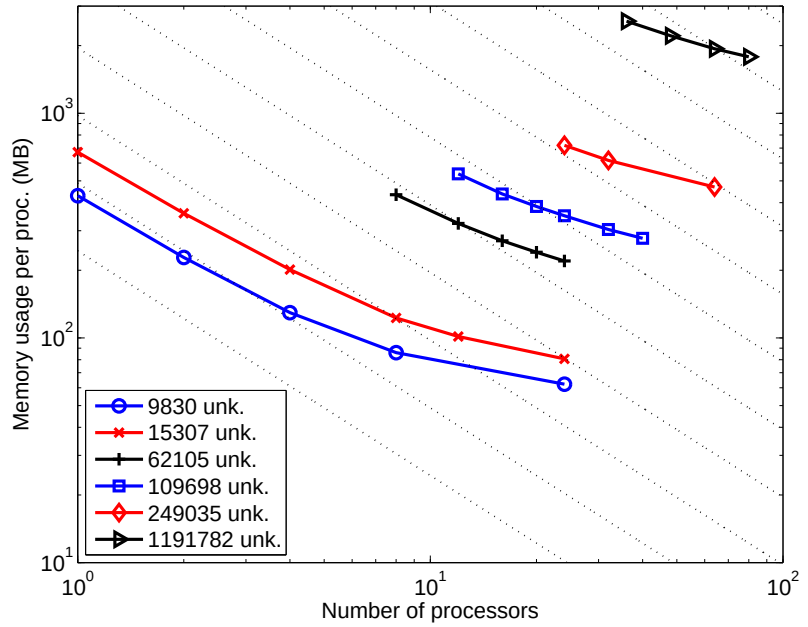

(a)

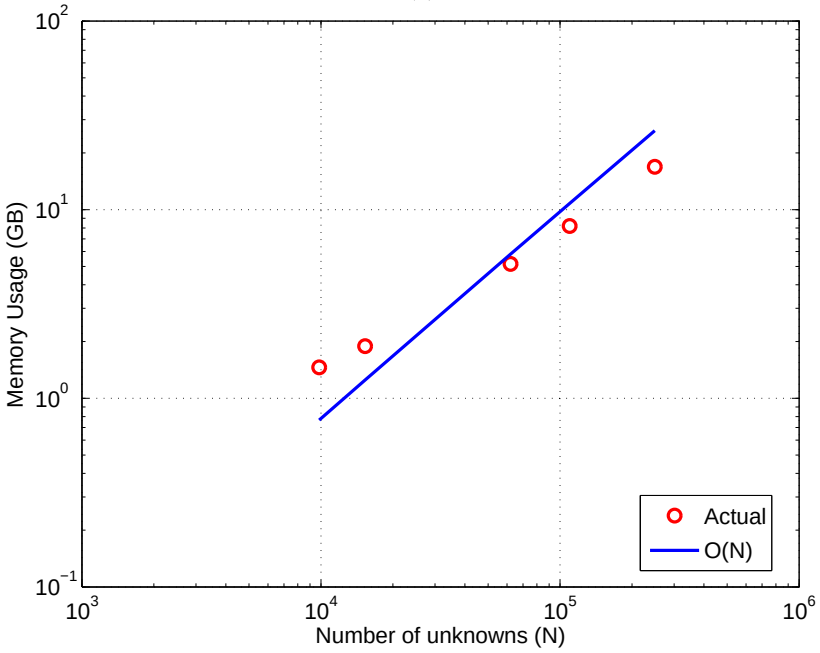

(b)

Figure 3.7: (a) Matrix-vector usage per processor versus number of processors for PEC plate example. Dashed lines are ideal speed-up tangents. (b) Total memory usage versus N. Simulations are executed on 24 processors.

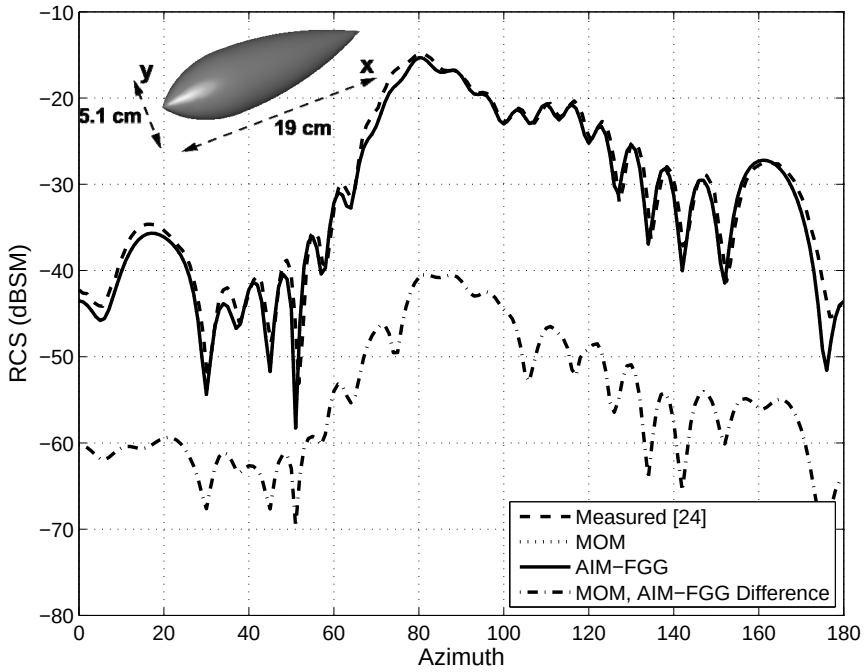

(a)

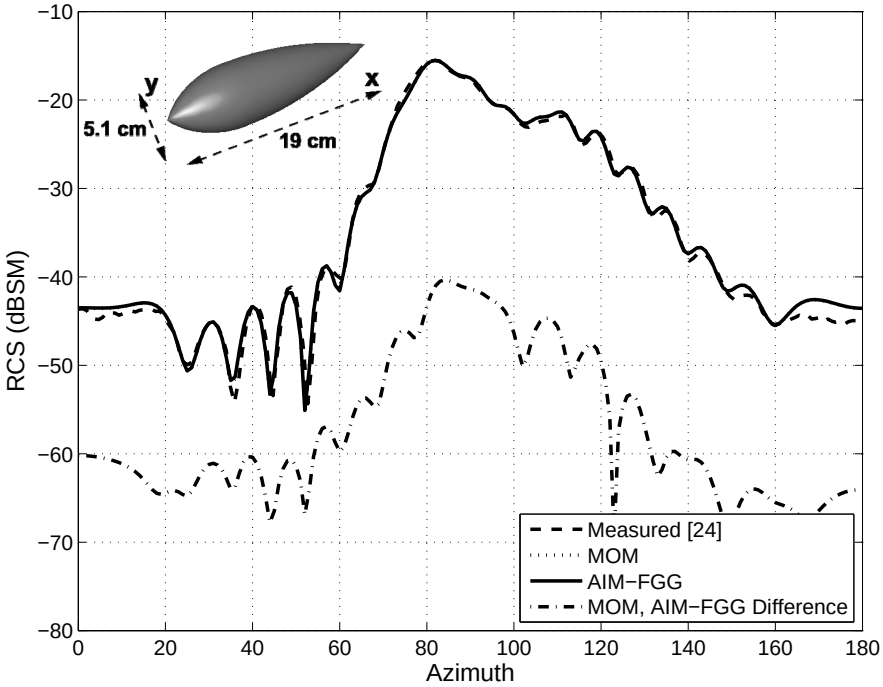

(b)

Figure 3.8: Monostatic RCS of the metallic double ogive at zero elevation angle for (a) HH (b) VV polarizations.

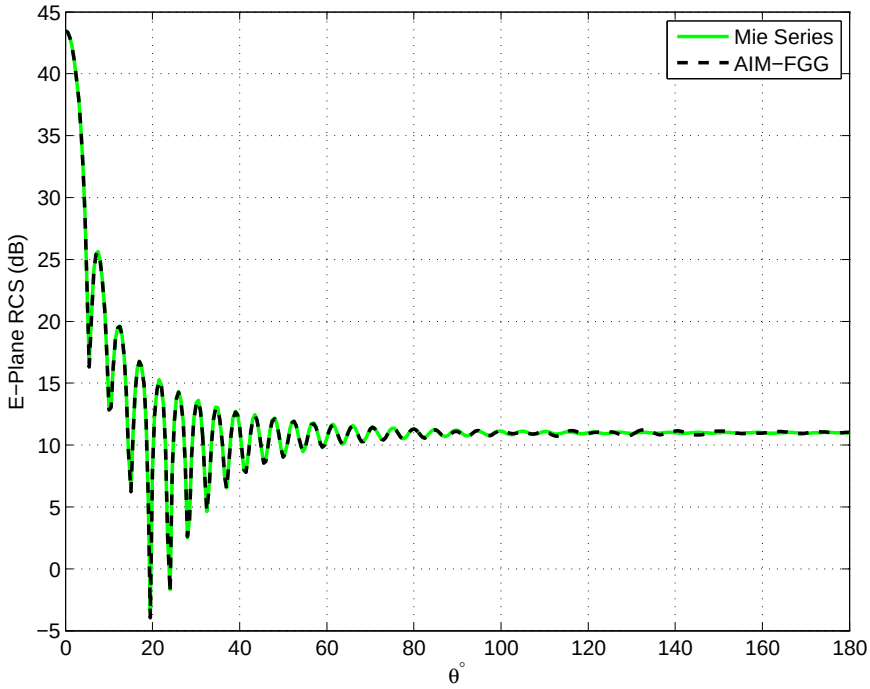

(a)

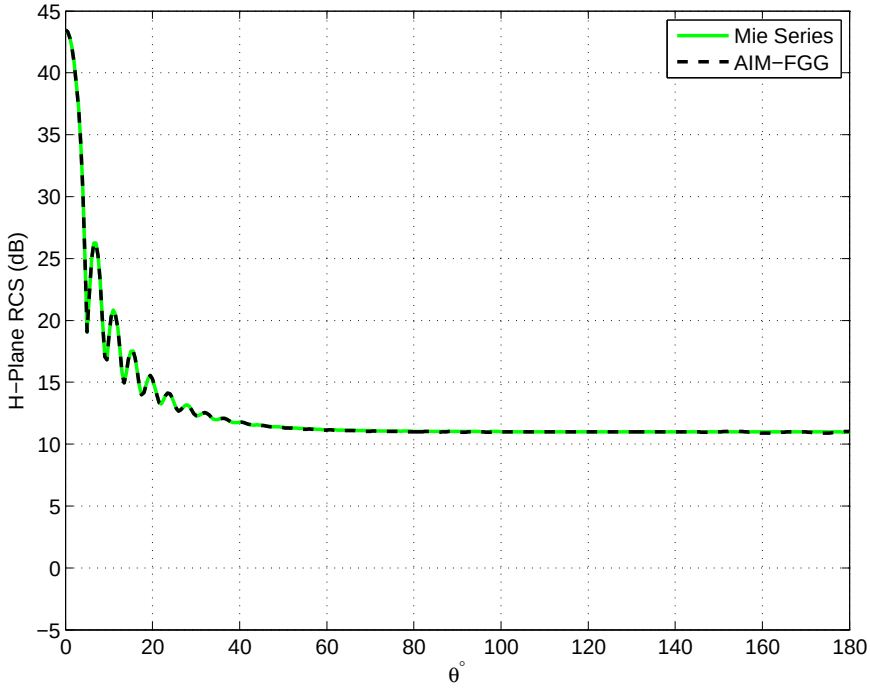

(b)

Figure 3.9: Bistatic RCS of a PEC sphere in (a) E-plane (b) H-plane.

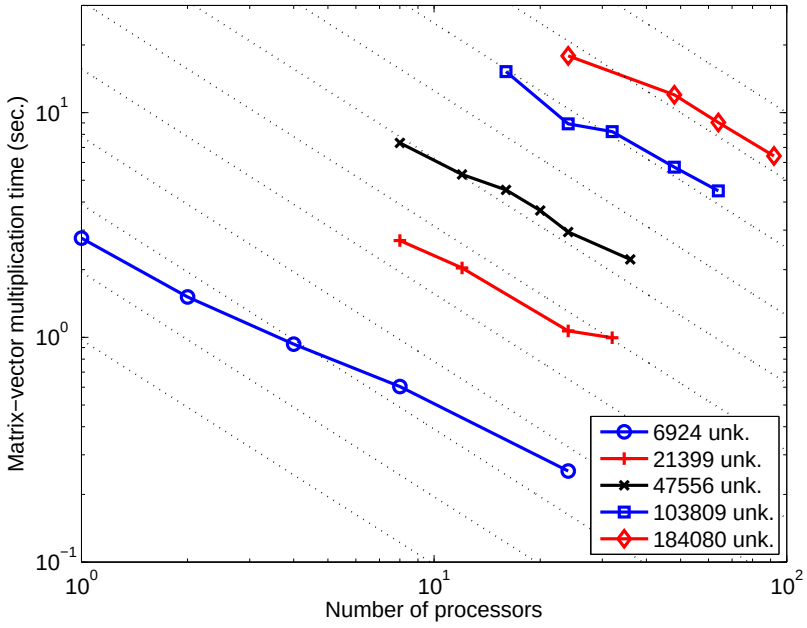

(a)

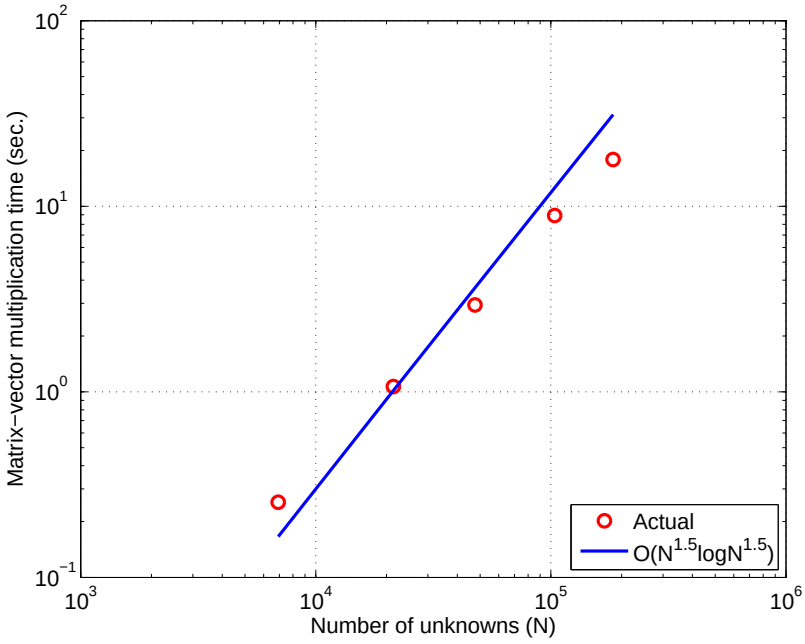

(b)

Figure 3.10: (a) Matrix-vector multiplication time versus number of processors for PEC sphere example. Dashed lines are ideal speed-up tangents. (b) Matrix-vector multiplication time versus N when simulations are executed on 24 processors.

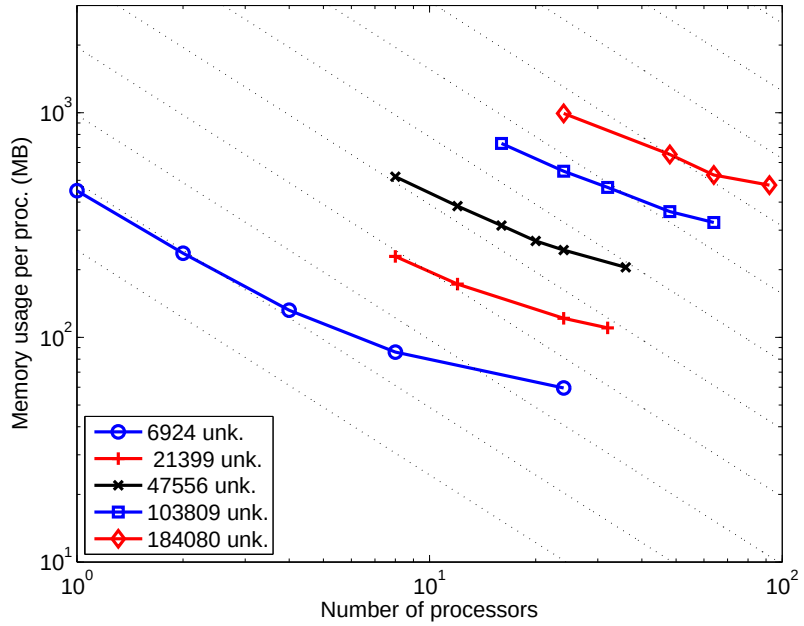

(a)

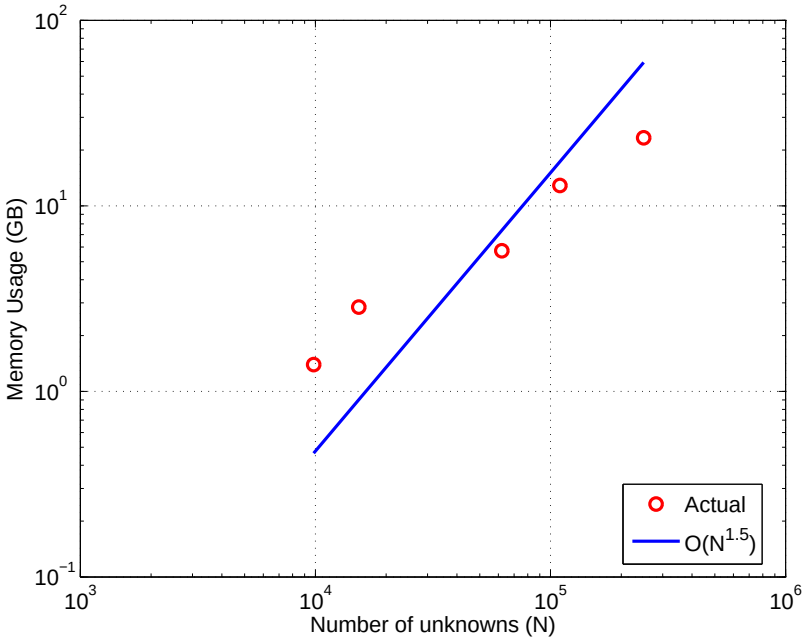

(b)

Figure 3.11: (a) Matrix-vector usage per processor versus number of processors for PEC sphere example. Dashed lines are ideal speed-up tangents. (b) Total memory usage versus N when simulations are executed on 24 processors.

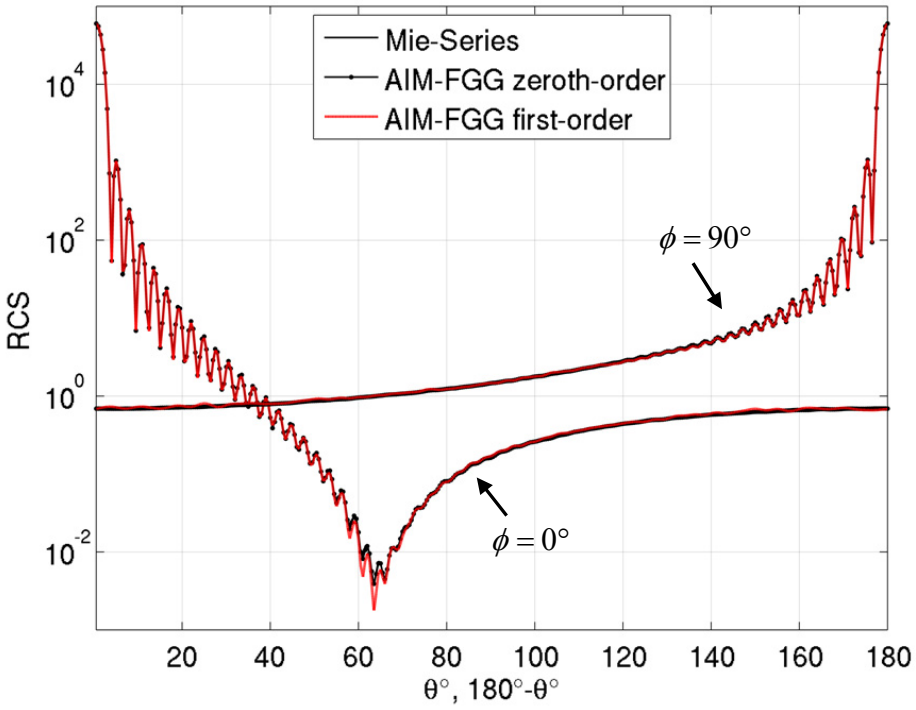

Figure 3.12: Bistatic RCS of a dielectric sphere. RCS is computed for two different orders of basis functions and compared to Mie-series solution

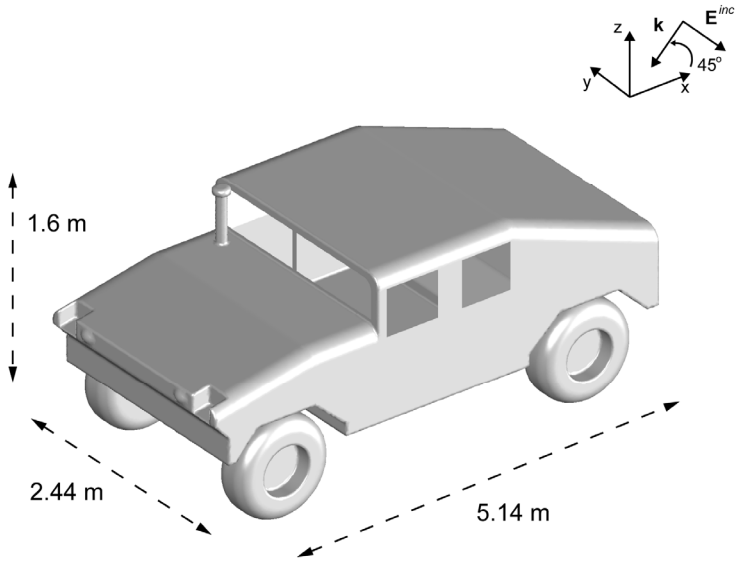

(a)

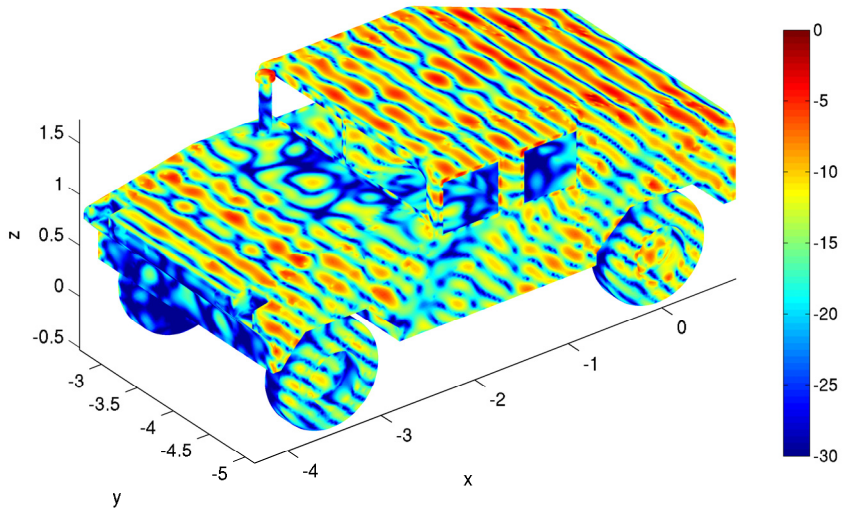

(b)

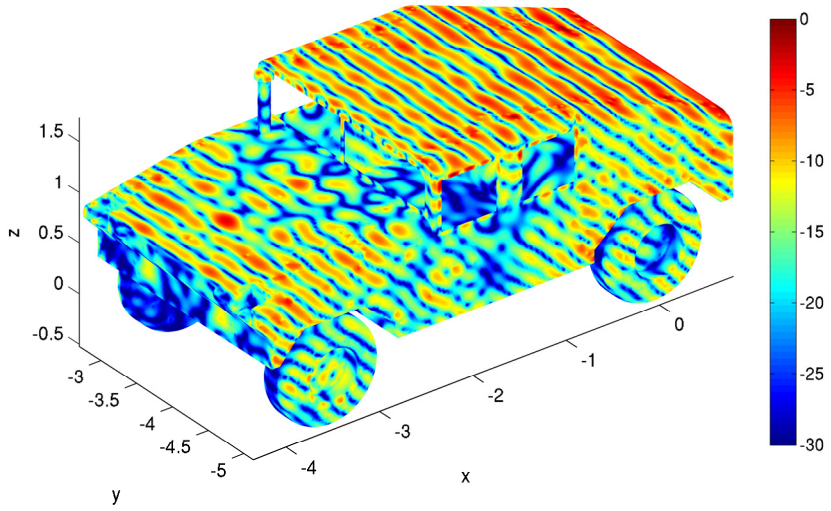

(c)

Figure 3.13: (a) Humvee geometry. (b) Real and (c) imaginary parts of the surface currents.

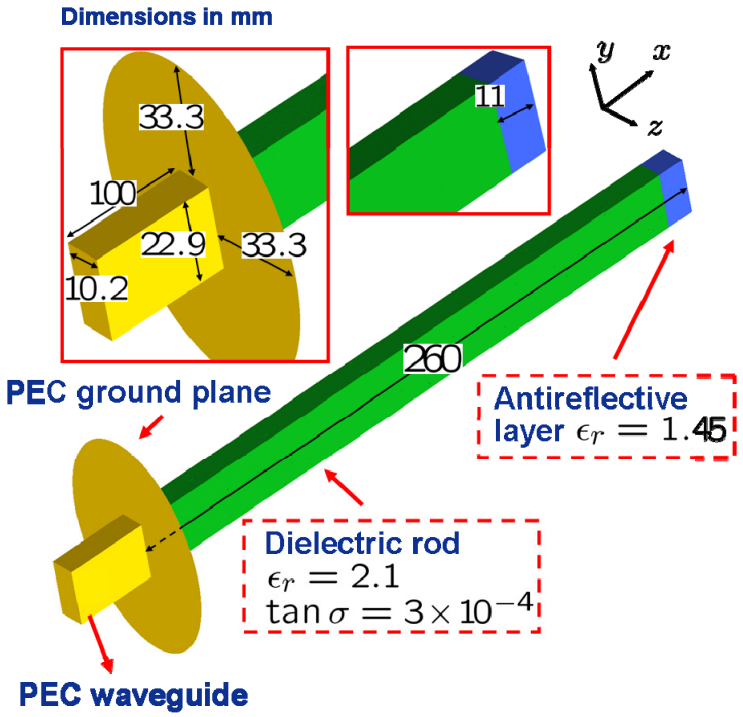

(a)

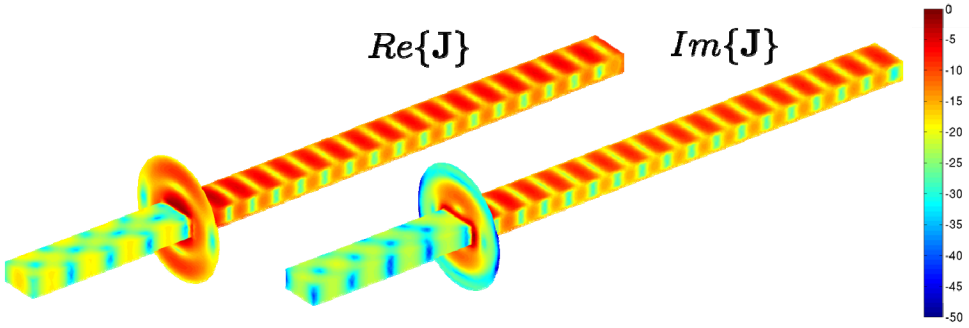

(b)

Figure 3.14: (a) Dielectric rod antenna geometry and material details. All dimensions are given in mm. (b) Real and imaginary parts of the surface currents.

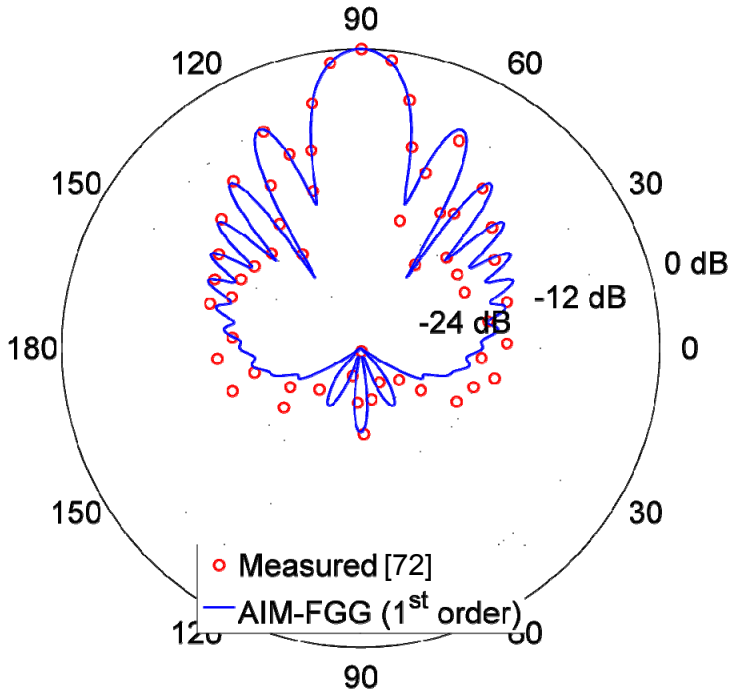

(a)

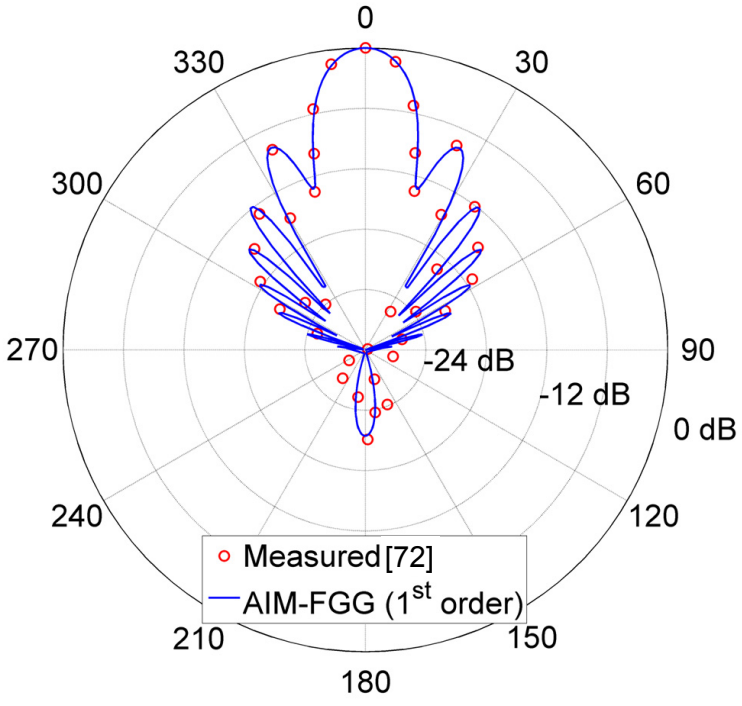

(b)

Figure 3.15: Radiation pattern of the dielectric rod antenna in (a) E- and (b) H-planes

CHAPTER 4
Volume Integral Equation Method

4.1 Introduction

The analysis of electromagnetic (EM) wave interactions from composite and inhomogeneous dielectric structures is important in many engineering applications such as characterization of radar cross section of complex structures, homogenization of metamaterials, radiation from antennas placed next to radomes [73, 74], and microwave imaging. Volume integral equation (VIE) based simulators provide high accuracy and flexibility for the analysis of arbitrarily inhomogeneous structures. The solution of VIEs via the method of moments (MOM) calls for the solution of linear systems of equations of order N, where N is the number of basis functions used to expand the fields inside the structure. The classical (non-accelerated) iterative solution of MOM systems requires $O\left(N^2\right)$ memory and $O\left(N^2\right)$ CPU resources. In contrast to surface integral equation (SIE) solvers, which require the expansion of the currents only on the surface of the object, VIE solvers lead to systems of larger N. However SIE solvers are only applicable to piecewise homogeneous structures.

Several accelerators that reduce these memory and CPU requirements of VIE solvers are proposed, examples include but not limited to, multi-level fast multipole algorithm (MLFMA), conjugate gradient fast Fourier transform (CG-FFT) and pre-corrected FFT

techniques, and the adaptive integral method (AIM); the latter two are closely related. These accelerators reduce the iterative solutions memory and CPU requirements to $O(N)$ and $O(N \log N)$, respectively. CG-FFT method requires the structure to be discretized with a uniform regular grid of hexahedral elements to exploit the Toeplitz property of the MOM matrix via FFTs. However this type of discretization leads to geometry errors due to staircase approximations, and larger number of unknowns since the original structure has to be embedded in a free-space box. MLFMA and AIM (also P-FFT) approaches are proposed to alleviate these drawbacks. Among these accelerators AIM is attractive in particular because of its straightforward implementation and parallelization.

In this chapter, AIM-FGG acceleration is presented for the iterative solution of VIEs. AIM-FGG is a memory efficient extension to conventional AIM, which is originally developed for high order SIE solvers for composite dielectric and PEC structures. AIM-FGG virtually eliminates the need to store AIM mapping coefficients. Section 4.2 summarizes the VIEs. The discretization of the VIE and their MOM based solution is detailed in Section 4.3. A CG-FFT based acceleration technique is presented in Section 4.4. This solver is mainly used to provide benchmark solutions for the proposed AIM-FGG accelerated VIE solver, which is summarized in Section 4.5. Finally, numerical results that serve to validate the presented formulation and demonstrate the efficiency of the proposed solver are presented in Section 4.6.

4.2 Volume integral equations

Consider the time-harmonic EM wave scattering problem from inhomogeneous dielectric objects with arbitrary shape residing in free-space. Let D represent the bounded but not necessarily connected domain which comprises all the scatterers. Let

$\varepsilon_r(\mathbf{r})$ and ε_0 denote the permittivity of D and free-space, respectively. All the objects are non-magnetic and have the permeability of free-space μ_0. An incident electric field $\mathbf{E}^i(\mathbf{r})$, generated by the sources $\mathbf{J}^i(\mathbf{r})$ located outside of D, illuminates the scatterers. According to Maxwell's equations, electric and magnetic fields $\mathbf{E}(\mathbf{r})$, $\mathbf{H}(\mathbf{r})$ satisfy

$$\nabla \times \mathbf{H}(\mathbf{r}) = j\omega\varepsilon(\mathbf{r})\mathbf{E}(\mathbf{r}) + \mathbf{J}^i(\mathbf{r}) \tag{4.1}$$

where $\mathbf{r} \in \mathbb{R}^3$ is the position vector. Let $\mathbf{J}(\mathbf{r})$ represent the volumetric polarization current density

$$\mathbf{J}(\mathbf{r}) = j\omega\left[\varepsilon(\mathbf{r}) - \varepsilon_0\right]\mathbf{E}(\mathbf{r}) \quad \mathbf{r} \in D. \tag{4.2}$$

Using (4.2), (4.1) is rewritten as

$$\nabla \times \mathbf{H}(\mathbf{r}) = j\omega\varepsilon_0\mathbf{E}(\mathbf{r}) + \mathbf{J}(\mathbf{r}) + \mathbf{J}^i(\mathbf{r}). \tag{4.3}$$

$\mathbf{J}(\mathbf{r})$ in (4.3) can be interpreted as a secondary source radiating in free-space generating the fields $\mathbf{E}^s(\mathbf{r})$. Then, the total fields can be expressed as the super-position of the fields generated by $\mathbf{J}(\mathbf{r})$ and $\mathbf{J}^i(\mathbf{r})$ [12]

$$\mathbf{E}(\mathbf{r}) = \mathbf{E}^s(\mathbf{r}) + \mathbf{E}^i(\mathbf{r}) \tag{4.4}$$

$$\mathbf{E}^s(\mathbf{r}) = -j\omega\mathbf{A}^s(\mathbf{r}) - \nabla\phi^s(\mathbf{r}). \tag{4.5}$$

Here, the magnetic vector and scalar electric potentials $\mathbf{A}^s$ and Φ^s are

$$\mathbf{A}^s(\mathbf{r}) = \int_D \mathbf{J}(\mathbf{r}')\, g(\mathbf{r}-\mathbf{r}')dr' \tag{4.6}$$

$$\Phi^s(\mathbf{r}) = \frac{-1}{j\omega\varepsilon_0}\int_D \nabla\cdot\mathbf{J}(\mathbf{r}')\, g(\mathbf{r}-\mathbf{r}')dr' \tag{4.7}$$

where ω is the angular frequency, $g(\mathbf{r}-\mathbf{r}') = e^{-jk_0|\mathbf{r}-\mathbf{r}'|}/\left(4\pi|\mathbf{r}-\mathbf{r}'|\right)$ is the free-space Green's function, $\mathbf{r}$ and $\mathbf{r}'$ are the observer and source points, and $k_0 = \omega\sqrt{\mu_0\varepsilon_0}$ is the free-space wave number. (4.4) along with (4.5)-(4.7) constitutes a VIE in terms of

unknown $\mathbf{J}(\mathbf{r})$. However, for the reasons that will become apparent later in this chapter, it is more convenient to formulate a VIE in terms of electric flux density

$$\mathbf{D}(\mathbf{r}) = \varepsilon(\mathbf{r})\mathbf{E}(\mathbf{r}). \tag{4.8}$$

$\mathbf{J}(\mathbf{r})$ and $\mathbf{D}(\mathbf{r})$ are related by the formula

$$\mathbf{J}(\mathbf{r}) = j\omega\chi(\mathbf{r})\mathbf{D}(\mathbf{r}) \tag{4.9}$$

where $\chi(\mathbf{r})$ is the contrast ratio

$$\chi(\mathbf{r}) = \frac{\varepsilon(\mathbf{r}) - \varepsilon_0}{\varepsilon(\mathbf{r})}. \tag{4.10}$$

Substitution of (4.9) into (4.6) and (4.7), and the resulting equations into (4.5) and (4.4) yields the VIE

$$\begin{aligned}\mathbf{E}^i(\mathbf{r}) = \frac{\mathbf{D}(\mathbf{r})}{\varepsilon(\mathbf{r})} - \frac{k_0^2}{\varepsilon_0}\int_D \chi(\mathbf{r}')\mathbf{D}(\mathbf{r}')g(\mathbf{r}-\mathbf{r}')dr' \\ + \frac{1}{\varepsilon_0}\nabla\int_D \nabla'\cdot\left[\chi(\mathbf{r}')\mathbf{D}(\mathbf{r}')\right]g(\mathbf{r}-\mathbf{r}')dr'.\end{aligned} \tag{4.11}$$

4.3 Numerical solution of VIEs

4.3.1 Geometry Modeling and Basis Functions

To numerical solve (4.11) for $\mathbf{D}(\mathbf{r})$, D is discretized using a mesh of hexahedron (brick) elements and the flux density $\mathbf{D}(\mathbf{r})$ is expanded as

$$\mathbf{D}(\mathbf{r}) \cong \sum_{k=1}^{N} I_k \mathbf{S}_k(\mathbf{r}) \tag{4.12}$$

where I_k and $\mathbf{S}_k(\mathbf{r})$, $k = 1,...,N$ are unknown expansion coefficients and divergence conforming roof-top basis functions, respectively [75, 76]. Each $\mathbf{S}_k(\mathbf{r})$ is supported in a

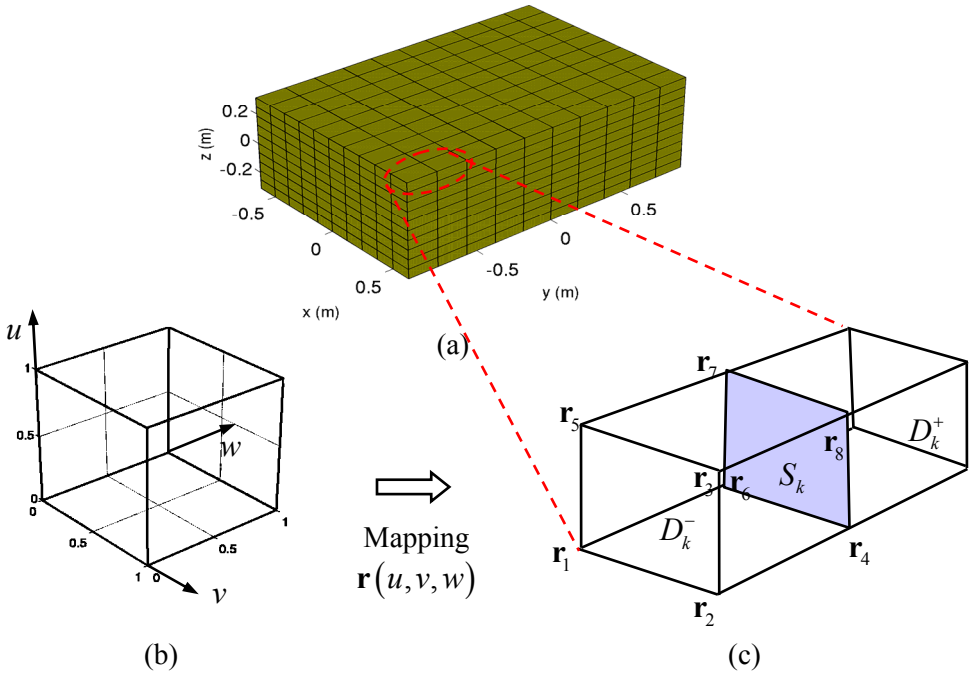

hexahedron pair $D_k = D_k^+ \cup D_k^-$ (Fig. 2 (c)). Let $\mathbf{S}_k^-(\mathbf{r})$ and $\mathbf{S}_k^+(\mathbf{r})$ represent part of the basis function $\mathbf{S}_k(\mathbf{r})$ defined on D_k^- and D_k^+, respectively.

Figure 4.1: (a) A hexahedral mesh of a rectangular prism. (b) Canonical unit cube. (c) Points in a hexahedron in real space can be obtained using a mapping from the reference system.

In order to represent basis functions supported in arbitrarily shaped hexahedra a reference system u,v,w is introduced as depicted in Fig. 2 (b). Then the volume of the hexahedron can be defined as a transformation of the unit cube in the reference system u,v,w to real space as

$$\mathbf{r}(u,v,w) = \sum_{i=1}^{8} P_i(u,v,w)\mathbf{r}_i \tag{4.13}$$

where $\mathbf{r}_i$, $i = 1,...,8$ are the vertices of the hexahedron, $0 \le u \le 1$, $0 \le v \le 1$, $0 \le w \le 1$, and $P_i(u,v,w)$ are the polynomials

$$
\begin{aligned}
&P_1 = (1-u)(1-v)(1-w) \quad P_2 = u(1-v)(1-w) \quad P_3 = (1-u)v(1-w) \\
&P_4 = uv(1-w) \quad P_5 = (1-u)(1-v)w \quad P_6 = u(1-v)w \\
&P_7 = (1-u)vw \quad P_8 = uvw.
\end{aligned} \tag{4.14}
$$

Base vectors and the Jacobian of the parametric transformation $\mathbf{r}(u,v,w)$ are given by

$$
\mathbf{a}_u = \frac{\partial \mathbf{r}}{\partial u} \quad \mathbf{a}_v = \frac{\partial \mathbf{r}}{\partial v} \quad \mathbf{a}_w = \frac{\partial \mathbf{r}}{\partial w}. \tag{4.15}
$$

$$
\mathcal{J} = \begin{bmatrix} \frac{\partial x}{\partial u} & \frac{\partial y}{\partial u} & \frac{\partial z}{\partial u} \\ \frac{\partial x}{\partial v} & \frac{\partial y}{\partial v} & \frac{\partial z}{\partial v} \\ \frac{\partial x}{\partial w} & \frac{\partial y}{\partial w} & \frac{\partial z}{\partial w} \end{bmatrix} \tag{4.16}
$$

Each hexahedron supports six half basis functions

$$
\begin{aligned}
&\mathbf{S}_1^-(\mathbf{r}) = \frac{1}{|\mathcal{J}|} u\mathbf{a}_u \quad \mathbf{S}_2^+(\mathbf{r}) = \frac{1}{|\mathcal{J}|}(1-u)\mathbf{a}_u \quad \mathbf{S}_3^-(\mathbf{r}) = \frac{1}{|\mathcal{J}|} v\mathbf{a}_v \\
&\mathbf{S}_4^+(\mathbf{r}) = \frac{1}{|\mathcal{J}|}(1-v)\mathbf{a}_v \quad \mathbf{S}_5^-(\mathbf{r}) = \frac{1}{|\mathcal{J}|} w\mathbf{a}_w \quad \mathbf{S}_6^+(\mathbf{r}) = \frac{1}{|\mathcal{J}|}(1-w)\mathbf{a}_w
\end{aligned} \tag{4.17}
$$

where $|\mathcal{J}|$ represents the determinant of $\mathcal{J}$. On each face S_k only one basis function $\mathbf{S}_k(\mathbf{r})$ has normal component which is also continuous over the face. This property naturally satisfies the continuity of the $\mathbf{D}(\mathbf{r})$ across dielectric interfaces. Also, $\chi(\mathbf{r})$ is approximated by piecewise constant functions which has a constant value $\chi_k^{\pm}$ over each hexahedron $D_k^{\pm}$, $k = 1,...,N$. To simplify the formulation that follows let $\chi_k(\mathbf{r})$ represent the local piecewise constant function

$$
\chi_k(\mathbf{r}) = \begin{cases} \chi_k^+, & \mathbf{r} \in D_k^+ \\ \chi_k^-, & \mathbf{r} \in D_k^- \\ 0, & \text{otherwise} \end{cases} \tag{4.18}
$$

4.3.2 MOM System of Equations

Substitution of (4.12) into (4.11) and testing the resulting equations with $\chi_k \mathbf{S}_k(\mathbf{r})$, $k = 1,...,N$ yields the MOM system

$$\mathbf{ZI} = \mathbf{V} \tag{4.19}$$

where $\mathbf{I}$ and $\mathbf{V}$ are the $N-$vectors of unknown coefficients and tested incident fields, and $\mathbf{Z}$ is the $N \times N$ MOM impedance matrix. Their entries are

$$\mathbf{I}(k) = I_k \tag{4.20}$$

$$\mathbf{V}(k) = \int_{D_k} \chi_k(\mathbf{r}) \mathbf{S}_k(\mathbf{r}) \mathbf{E}^i(\mathbf{r}) dr \tag{4.21}$$

$$\begin{aligned}
\mathbf{Z}(k,k') = & \int_{D_k} \chi_k(\mathbf{r}) \mathbf{S}_k(\mathbf{r}) \left(1 - \chi_{k'}(\mathbf{r})\right) \mathbf{S}_{k'}(\mathbf{r}) dr \\
& - \frac{k_0^2}{\varepsilon_0} \int_{D_k} \int_{D_{k'}} \chi_k(\mathbf{r}) \mathbf{S}_k(\mathbf{r}) g(\mathbf{r}-\mathbf{r}') \chi_{k'}(\mathbf{r}') \mathbf{S}_{k'}(\mathbf{r}') dr' dr \\
& - \frac{1}{\varepsilon_0} \left[\begin{array}{l}
\displaystyle\int_{D_k} \int_{D_{k'}} \chi_k(\mathbf{r}) \nabla \cdot \mathbf{S}_k(\mathbf{r}) g(\mathbf{r}-\mathbf{r}') \chi_{k'}(\mathbf{r}') \nabla' \cdot \mathbf{S}_{k'}(\mathbf{r}') dr' dr \\
+ \left(\chi_{k'}^- - \chi_{k'}^+\right) \displaystyle\int_{D_k} \int_{S_{k'}} \chi_k(\mathbf{r}) \nabla \cdot \mathbf{S}_k(\mathbf{r}) g(\mathbf{r}-\mathbf{r}') dr' dr \\
+ \left(\chi_k^- - \chi_k^+\right) \displaystyle\int_{S_k} \int_{D_{k'}} g(\mathbf{r}-\mathbf{r}') \chi_{k'}(\mathbf{r}') \nabla' \cdot \mathbf{S}_{k'}(\mathbf{r}') dr' dr \\
\left(\chi_k^- - \chi_k^+\right)\left(\chi_{k'}^- - \chi_{k'}^+\right) \displaystyle\int_{S_k} \int_{S_{k'}} g(\mathbf{r}-\mathbf{r}') dr' dr
\end{array} \right]
\end{aligned} \tag{4.22}$$

where $k = 1,...,N$ and $k' = 1,...,N$. Note that there is an ambiguity when S_k touches the boundary of D since D_k^+ (or D_k^-) falls beyond D and it is not defined. This can be solved by padding the original mesh with a single layer of elements with free-space permittivity $(\chi = 0)$.

When N is large, (4.19) can only be solved iteratively, a process that requires the repeated multiplication of $\mathbf{Z}$ by trial solution vectors. The memory and CPU time requirements of classical MOM-based iterative solvers therefore scale as $O(N^2)$ and

$O\left(N_{\text{iter}}N^2\right)$, respectively. Here N_{iter} is the number of iterations required for the solution to reach a given accuracy; typically $N_{\text{iter}} \ll N$, especially when D is electrically large and uniformly discretized.

4.4 A Special Case: Uniform Mesh and FFT Accelerated VIE solver

When the hexahedra mesh conforms to a regular grid, $\mathbf{Z}$ becomes a multilevel block Toeplitz (MBT) matrix due to $g(\mathbf{r})$'s spatial translational invariance property. By the virtue of the MBT property, matrix vector multiplications pertinent to $\mathbf{Z}$ can be carried out efficiently (and exactly) using FFTs. This method reduces the memory and CPU requirements of the MOM-based iterative solver to $O(N)$ and $O\left(N_{iter}N\log N\right)$, respectively [15].

To detail the VIE-FFT algorithm, matrix equation (4.19) is decomposed into five terms as

$$\mathbf{RI}+\mathcal{I}_{\chi^+}\mathbf{Z}^{+,+}\mathcal{I}_{\chi^+}\mathbf{I}+\mathcal{I}_{\chi^+}\mathbf{Z}^{+,-}\mathcal{I}_{\chi^-}\mathbf{I}+\mathcal{I}_{\chi^-}\mathbf{Z}^{-,+}\mathcal{I}_{\chi^+}\mathbf{I}+\mathcal{I}_{\chi^-}\mathbf{Z}^{-,-}\mathcal{I}_{\chi^-}\mathbf{I}=\mathbf{V} \tag{4.23}$$

where $\mathbf{R}$ is a sparse matrix with entries representing the first integral in (4.19), $\mathcal{I}_{\chi^\pm}$ is the diagonal matrix with entries $\chi_k^\pm, k=1,...,N.$ Here, $\left(k,k'\right)^{th}$ entry of $\mathbf{Z}^{\pm,\pm}$ denote the remaining interaction integrals in (4.19) involving only half basis functions $\mathbf{S}_k^\pm(\mathbf{r})$ and $\mathbf{S}_{k'}^\pm(\mathbf{r})$ excluding the contrast functions χ_k^+ and $\chi_{k'}^\pm$.

For a regular grid each basis function can be addressed by three integers $p=1,...,P,$ $q=1,...,Q,$ $r=1,...,R.$ For the sake of simplicity, in what follows the index k and the notation $\mathbf{S}_k^\pm(\mathbf{r})$ are replaced with the quartet (p,q,r,t) and the notation $\mathbf{S}_{p,q,r}^{t,\pm}(\mathbf{r})$. $t=1,\ 2,\ 3$ along with $+$ or $-$ sign discriminates the six half basis functions defined on a hexagon. Using the new notation entries of $\mathbf{Z}^{\dagger,\dagger'}$ are denoted as

$$\mathbf{Z}^{\dagger,\dagger'}\left(k,k'\right)=\mathbf{Z}^{\dagger,\dagger'}\left(p-p',q-q',r-r';t,t'\right), \tag{4.24}$$

where † and †′ denotes + or − signs, and the MLT property is indicated. Then, the k^{th} entry of the matrix vector product $\mathbf{Z}^{\dagger,\dagger'}\mathbf{I}_{\chi^{\dagger'}}$ can be represented as the 3D convolution

$$\left[\mathbf{Z}^{\dagger,\dagger'}\mathbf{I}_{\chi^{\pm}}\right]_k = \chi^{\dagger}_{p,q,r}\sum_{t'}\sum_{p'}\sum_{q'}\sum_{r'}\mathbf{Z}^{\dagger,\dagger'}\left(p-p',q-q',r-r';t,t'\right)\chi^{\dagger'}_{p',q',r'}I^{t',\dagger'}_{p',q',r'}. \quad (4.25)$$

Finally, the convolutions in (4.25) are carrier out efficiently by using 3D FFTs (and IFFTs) of size $2P\times 2Q\times 2R$ and element to element vector multiplications, as is well known. The $O\left(N_{iter}N\log N\right)$ computational cost of VIE-FFT is due all FFTs, and $O\left(N\right)$ memory requirements are due to the storage of unique blocks of $\mathbf{Z}^{\dagger,\dagger'}$ and the sparse matrices and vectors in (4.23)

4.5 AIM-FGG Accelerated VIE solver

Alternatively, the matrix vector multiplications pertinent to the MOM matrix $\mathbf{Z}$ can be accelerated with AIM-FGG. When using AIM $\mathbf{Z}$ is separated into near and far field components as

$$\mathbf{Z} = \mathbf{Z}^{\text{near}} + \mathbf{Z}^{\text{far}}. \quad (4.26)$$

The AIM accelerates the matrix vector multiplications involving $\mathbf{Z}^{\text{far}}$ by using point sources on the auxiliary AIM grid. Let $A_k\left(\mathbf{r}\right)$ denote the integral

$$A_k(\mathbf{r}) = \int_{D_k}\psi_k(\mathbf{r}')g_p(\mathbf{r}-\mathbf{r}')dr' \quad (4.27)$$

which appears in (4.22), where $\psi_k(\mathbf{r}')$ represents $I_k\nabla'\cdot\chi_k(\mathbf{r}')\mathbf{S}_k(\mathbf{r}')$ or any Cartesian component of $I_k\chi_k(\mathbf{r}')\mathbf{S}_k(\mathbf{r}')$. Using an N^q point quadrature rule, (3.2) is approximated as

$$A_k(\mathbf{r}) \cong \sum_{i=1}^{N^q}\psi_k^i g(\mathbf{r}-\mathbf{r}_k^i), \quad (4.28)$$

with $\psi_k^i = \psi_k\left(\mathbf{r}_k^i\right) w_k^i$; here, and in (3.3), $\mathbf{r}_k^i = \hat{\mathbf{x}}x_k^i + \hat{\mathbf{y}}y_k^i + \hat{\mathbf{z}}z_k^i$ and w_k^i, $i = 1,...,N_q$, are quadrature points and weights for the k^{th} basis function respectively. Then, the AIM-FGG algorithm described in Chapter 3 can be employed to accelerate the iterative solution of (4.19). In (4.26) $\mathbf{Z}^{\text{near}}$ is a sparse matrix that stores pre-corrected near-field interactions; its entries are computed using (4.22) and corrected for the errors introduced by the use of global FFTs used in the matrix-vector multiplications involving $\mathbf{Z}^{\text{far}}$.

In the special case when the hexahedra mesh conforms to a regular grid, AIM-FGG can be modified in two aspects for further memory efficiency. First, only a single row/column of $\mathbf{Z}^{\text{near}}$ is enough to represent the whole $\mathbf{Z}^{\text{near}}$ since the entries are repeating themselves due to the regularity of the structure. Second, when element dimensions are the same only one set of coefficients are required to map the actual sources to the nearest AIM sources. That is, only $4N^q$ coefficients are computed/stored and used for the whole mesh. The memory efficiency of this special AIM-FGG implementation is shown by examples in the numerical results section.

In contrast to FFT acceleration, AIM-FGG acceleration of VIE solver allows its hybridization with SIE solvers. This is due to the explicit calculation of the fields on the auxiliary AIM grid in AIM-FGG. When hybridized with an SIE solver an extended AIM grid covering both domains allows both solvers to couple.

4.6 Numerical Results

This section presents numerical results that validate the solvers and demonstrate their efficiency. First, nonaccelerated VIE solver is used to analyze EM scattering from a dielectric sphere and an array of dielectric cubes and the results are compared to those obtained using exact analytical methods, i.e. Mie series solutions, and a PMCHWT based SIE solver. Next, VIE-FFT solver is validated via the scattering analysis of a dielectric

cube and a large dielectric sphere and the results are compared to those obtained using nonaccelerated VIE solver, Mie series solution, and the SIE solver. Finally, VIE-AIM-FGG is used to analyze scattering from a large dielectric cube and the results are compared to those obtained using the VIE-FFT solver. In the examples mesh density is represented by average edge length of the hexahedral elements δ. All solvers are implemented using the popular message passing interface (MPI) programming model, and executed on clusters of processors to reduce the computational requirements. Computational complexity and the parallelization efficiency of the above mentioned solvers are demonstrated via memory usage and CPU time statistics for problems with increasing N and number of processors. A transpose free quasi minimal residual (TFQMR) iterative scheme [55] is used to solve MOM matrix equations. Unless otherwise stated the tolerance of TFQMR is set to 10^{-6} and N_{iter} represents number of iterations required to reach this tolerance in the examples. All simulations are carried out on a cluster of dual-core 2.8 GHz AMD Opteron 2220 SE processors at the Center for Advanced Computing, University of Michigan. A parallel subroutine library, FFTW [77], is employed to carry out the FFTs (and IFFTs) in the VIE-FFT and VIE-AIM-FGG solvers.

4.6.1 Validation of the Non-Accelerated VIE-Solver

The first test geometry is a dielectric sphere of radius 0.24 m with relative permittivity $\varepsilon_r = 2.0 - j0.5$. The sphere is embedded in a free-space cube of edge length 0.48 m. A staircase approximation models the sphere as shown in the inset in Fig. 4.2. A VIE solver is used to compute the RCS of the sphere and the results are compared to the Mie series solution. The sphere is illuminated by a plane wave

$$\mathbf{E}^i = \hat{\mathbf{p}} e^{-jk_0 \hat{\mathbf{k}}\mathbf{r}}, \tag{4.29}$$

with $\hat{\mathbf{p}} = \hat{\mathbf{x}}$ and $\hat{\mathbf{k}} = \hat{\mathbf{z}}$, and frequency $f =$ 750 MHz. In the simulation average edge length, number of unknowns, and number of iterations are $\delta = 0.02$ m, $N = 43,200$, and $N_{iter} = 20$, respectively. Fig. 4.2 (a) shows the bistatic RCS of the sphere in E-plane ($\phi = 0°$) and H-plane ($\phi = 90°$).

Next, the EM scattering from a structure comprising $2 \times 2 \times 2$ array of dielectric cubes is analyzed and the results are compared to those of a PMCHWT based SIE solver. Cubes are homogeneous and each has the dimensions 0.5 m × 0.5 m × 0.5 m. The relative permittivity of the dielectric medium in cubes is linearly varied between $1.5 - 5.0$ from the first cube to the last, as shown in Fig. 4.3 (c). The structure is illuminated with a $\hat{\mathbf{p}} = \hat{\mathbf{x}}$ polarized plane wave propagating in $\hat{\mathbf{k}} = \hat{\mathbf{z}}$ direction at $f =$ 300 MHz. In the VIE based simulation $\delta = 0.05$ m, $N = 26,400$, and $N_{iter} = 84$, whereas in the SIE based simulation $N = 28,800$, and $N_{iter} = 614$. A diagonal pre-conditioner is used for the SIE solver. The triangular mesh used in the SIE solver is also shown in Fig. 4.3 (d). Fig. 4.3 (a) and (b) shows the bistatic RCS of the sphere in E-plane ($\phi = 0°$) and H-plane ($\phi = 90°$), respectively.

4.6.2 Validation of the VIE-FFT Solver

The first test geometry for the VIE-FFT solver is a dielectric cube of edge length 0.5 m, with $\varepsilon_r = 2.0 - j0.5$. The cube is discretized with a regular uniform grid of hexahedral elements with $\delta = 0.02$ m. The incident field is a $\hat{\mathbf{x}}$ polarized plane wave propagating in $\hat{\mathbf{z}}$ direction at $f = 750$ MHz. The EM scattering from the cube is analyzed and the results are compared to those obtained with nonaccelerated VIE solver, and PMCHWT based SIE solver. In the VIE-FFT simulation $N = 48,750$, and $N_{iter} = 20$, whereas in the SIE based simulation $N = 22,500$, and $N_{iter} = 309$. In the SIE solver a diagonal pre-conditioner is utilized. Fig. 4.4 shows the bistatic RCS of the cube in E-plane ($\phi = 0°$) and H-plane ($\phi = 90°$).

Next, a series of simulations are performed by increasing the size of the dielectric cube while keeping rest of the simulation parameters intact. Simulations are carried out using 32 processors. Fig. 4.6 (a) and (b) show the matrix setup and matrix-vector multiplication times, and fitting $O(N)$ and $O(N \log N)$ lines, respectively. The deviation from $O(N \log N)$ line in Fig. 4.6 (b), especially for small N, is due to the overhead associated with the parallel FFTs.

To demonstrate the parallel efficiency of the solver scattering from a dielectric cube of edge length 3.2 m, with $\varepsilon_r = 2.0$ is analyzed using the VIE-FFT solver. A series of simulations are performed by increasing the number of processors. The incident field is a $\hat{\mathbf{x}}$ polarized plane wave propagating in $\hat{\mathbf{z}}$ direction at $f = 300$ MHz. In all simulations $\delta = 0.05$ m, $N = 798,720$, and $N_{iter} = 130$. Memory usage and matrix-vector multiplication time of the solver are plotted with respect to number of processors in Fig. 4.6 (c) and (d).

4.6.3 Validation of the VIE-AIM-FGG Solver

Finally, the VIE-AIM-FGG solver is validated via the scattering analysis of dielectric cubes with $\varepsilon_r = 2.0$. Six simulations are performed by increasing the size of the dielectric cube while keeping other simulation parameters intact. All cubes are discretized with a regular uniform grid of hexahedral elements with $\delta = 0.1$ m. The incident field is a $\hat{\mathbf{x}}$ polarized plane wave propagating in $\hat{\mathbf{z}}$ direction at $f = 300$ MHz. AIM grid size $\Delta x = \Delta y = \Delta z = 0.0833$ m and $\mathcal{M} = 6$. The RCS of the cube is computed and the results are compared to those obtained with VIE-FFT solver. The edge lengths of the cubes, N, N_{iter}, and the root mean square (RMS) error in bistatic RCS results are given in Table 4.1. Here, RMS error

$$\text{RMS Error}=\frac{\sqrt{\sum_{i=1}^{N_s}\left|\sigma\left(\theta_i,\phi_i\right)-\sigma^{ref}\left(\theta_i,\phi_i\right)\right|^2}}{\sqrt{\sum_{i=1}^{N_s}\sigma^{ref}\left(\theta_i,\phi_i\right)^2}} \tag{4.30}$$

where σ and σ^{ref} represent the bistatic RCS obtained by the VIE-AIM-FGG solver and VIE-FFT solver, respectively. In (5.31) N_s represents the total number of observation angles $\left(\theta_i\right)$ in E- $\left(\phi_i=0°\right)$ and H- $\left(\phi_i=90°\right)$ planes at which RCS is sampled. Fig. 4.7 (a) and (b) show the bistatic RCS of the 6.0 m cube in E-plane ($\phi=0°$) and H-plane ($\phi=90°$). All simulations are carried out using 16 processors. Fig. 4.8 (a) and (b) show CPU time to setup $\mathbf{Z}^{\text{near}}$ and carry out each matrix-vector multiplication with respect to N. Also the fitting $O(1)$ and $O(N\log N)$ lines are overlaid in this figure. To demonstrate the parallel efficiency of the VIE-AIM-FGG solver the case with 4.0 m edge length is simulated using increasing number of processors. Fig. 4.8 (c) shows the CPU time to carry out each matrix vector multiplication with respect to the number of processors. The solver exhibits excellent scalability in this example.

Cube Edge Length	2.0 m	2.5 m	3.0 m	4.0 m	5.0 m	6.0 m
N	25,200	48,750	83,700	196,800	382,500	658,800
N_{iter}	50	71	107	212	383	592
RMS error	0.0046	0.0252	0.058	0.0397	0.0251	0.0353

Table 4.1: Number of unknowns and iterations, and RMS error in the RCS results of the VIE-AIM-FGG solver for various dielectric cubes of given edge lengths. Reference results for is the RMS error calculations are obtained with the FFT solver.

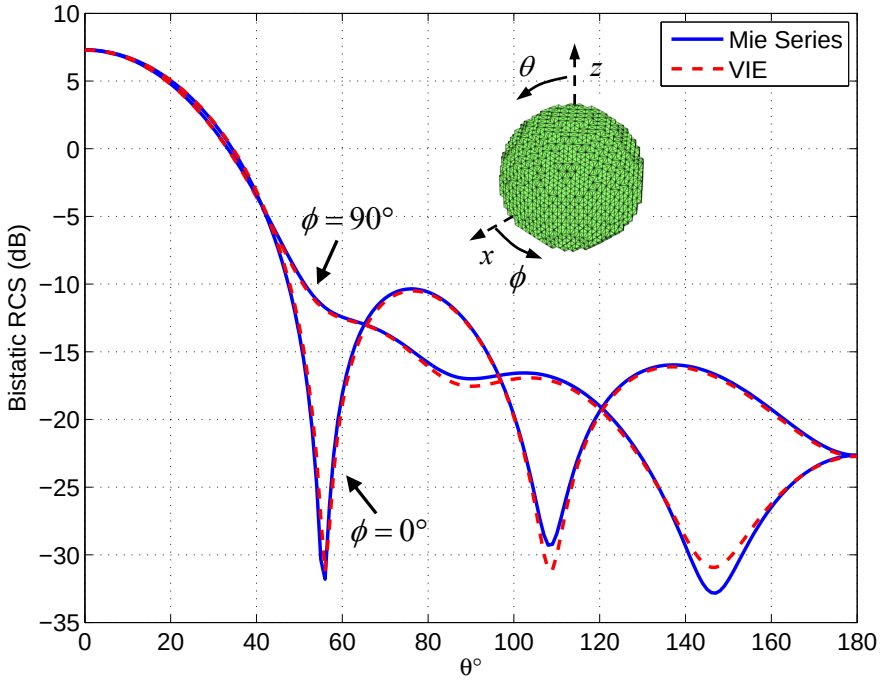

Figure 4.2: Bistatic RCS of a dielectric sphere of radius 0.24 m and relative permittivity $\varepsilon_r = 2 - j0.5$.

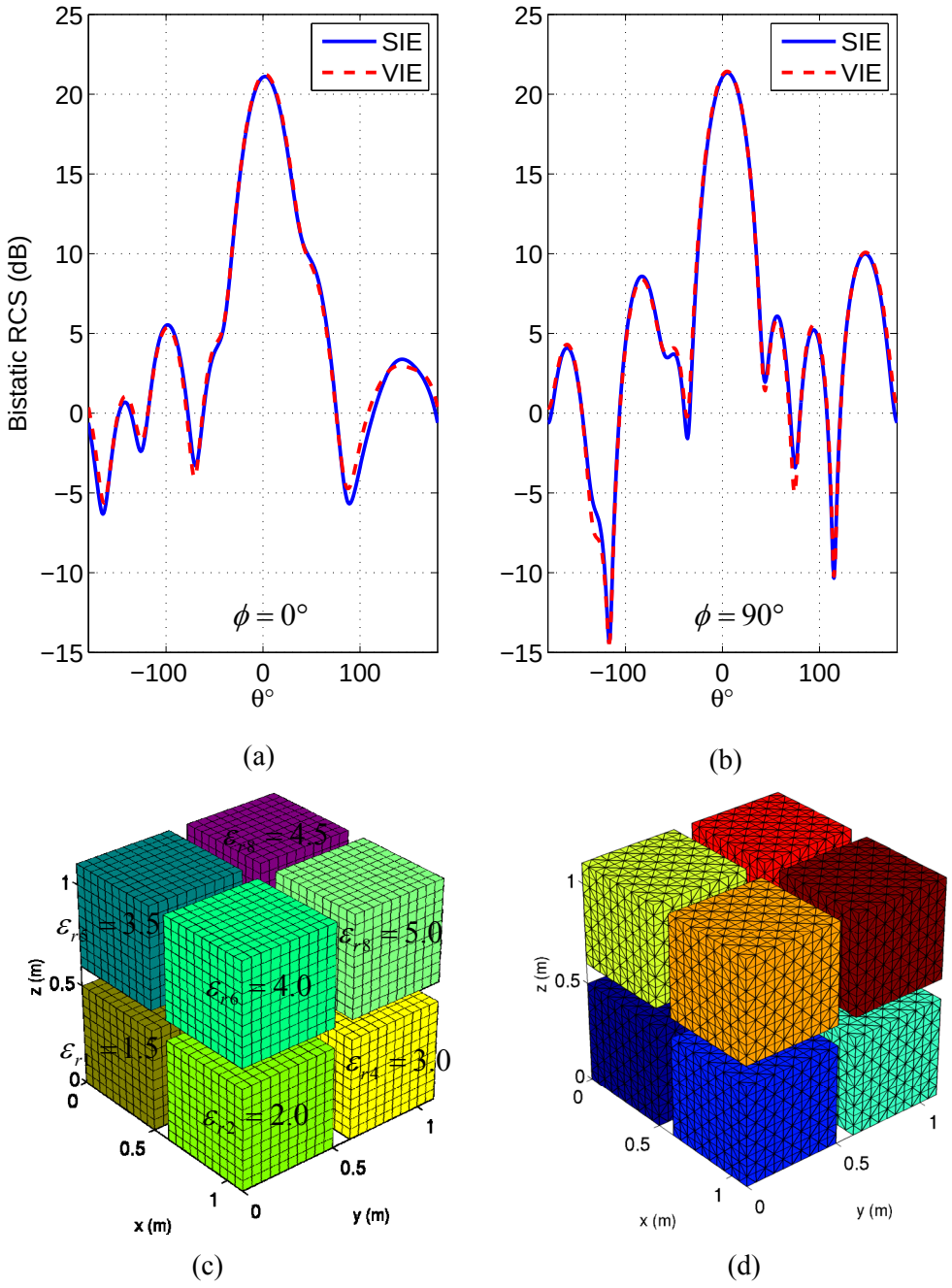

Figure 4.3: Bistatic RCS of the eight cube structure in (a) E- and (b) H-planes. The meshes of eight cube structure for (c) VIE and (d) SIE solvers. The relative permittivity of each cube is given in (c).

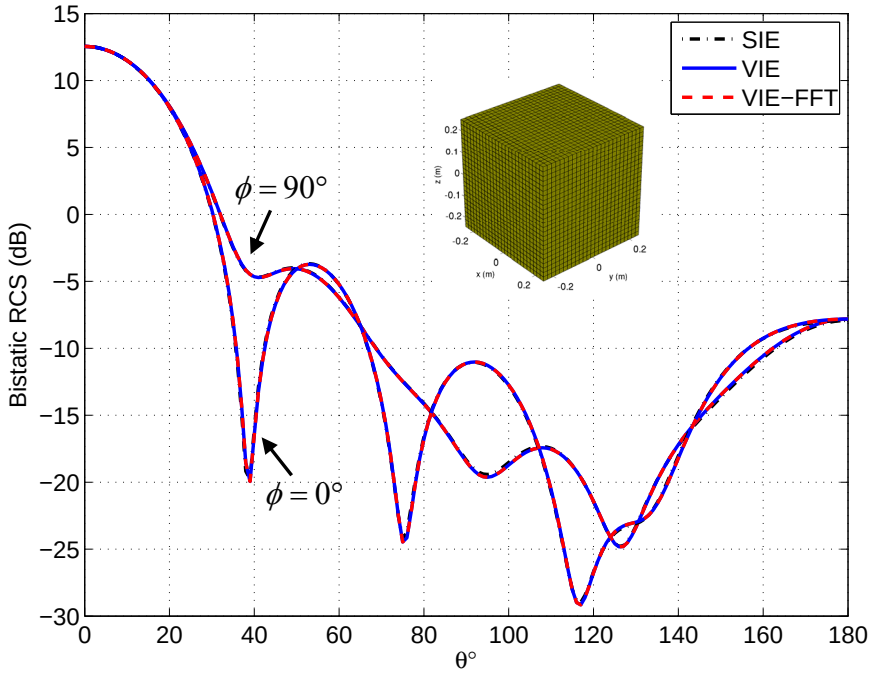

Figure 4.4: Bistatic RCS of a homogeneous dielectric cube of edge length 0.5 m and relative permittivity $\varepsilon_r = 2.0 - j0.5$.

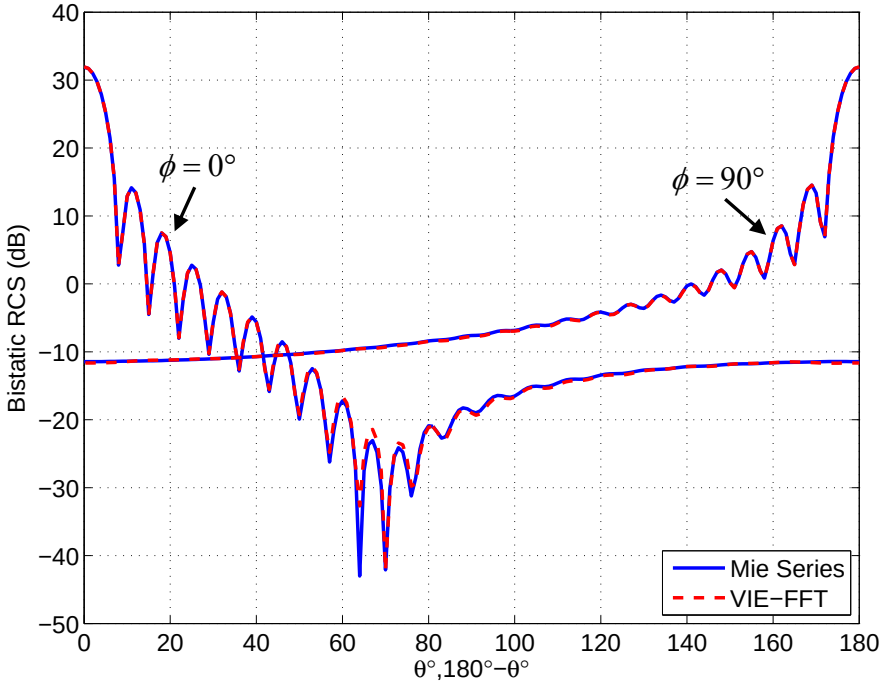

Figure 4.5: Bistatic RCS of a dielectric sphere of radius 0.8 m and relative permittivity $\varepsilon_r = 2.0 - j0.5$.

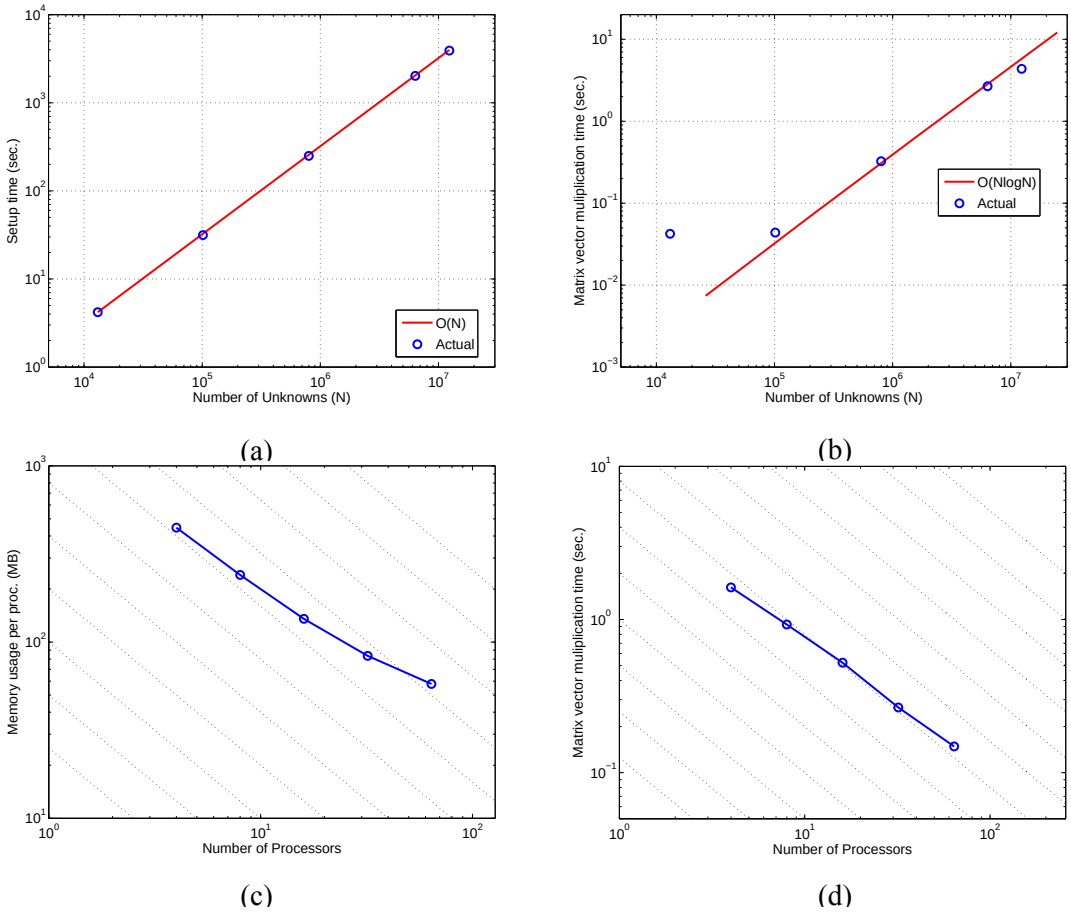

Figure 4.6: (a) Matrix setup and (b) matrix vector multiplication time of the VIE-FFT solver. (c) Memory usage and (d) matrix vector multiplication time versus number of processors. Dashed lines in (c) and (d) represent the ideal scaling lines.

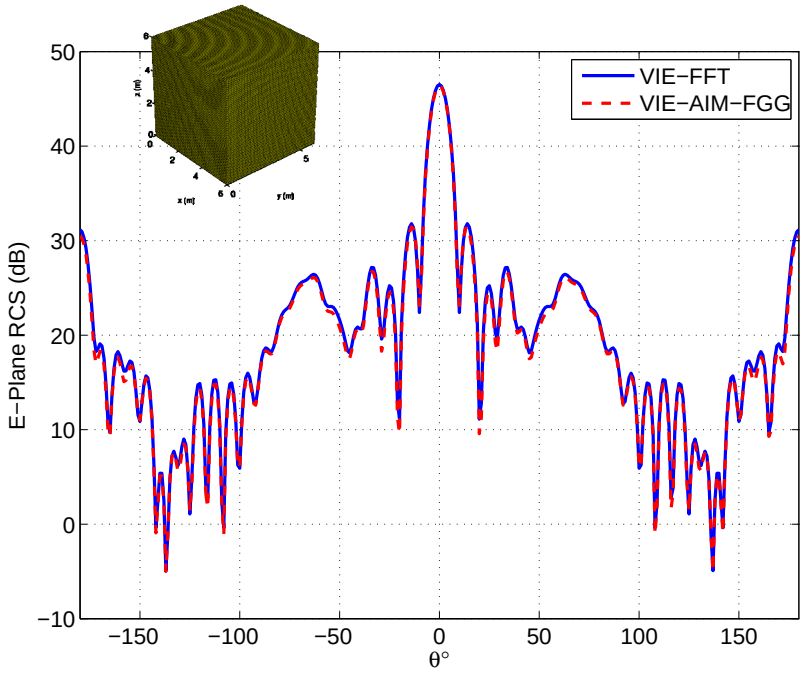

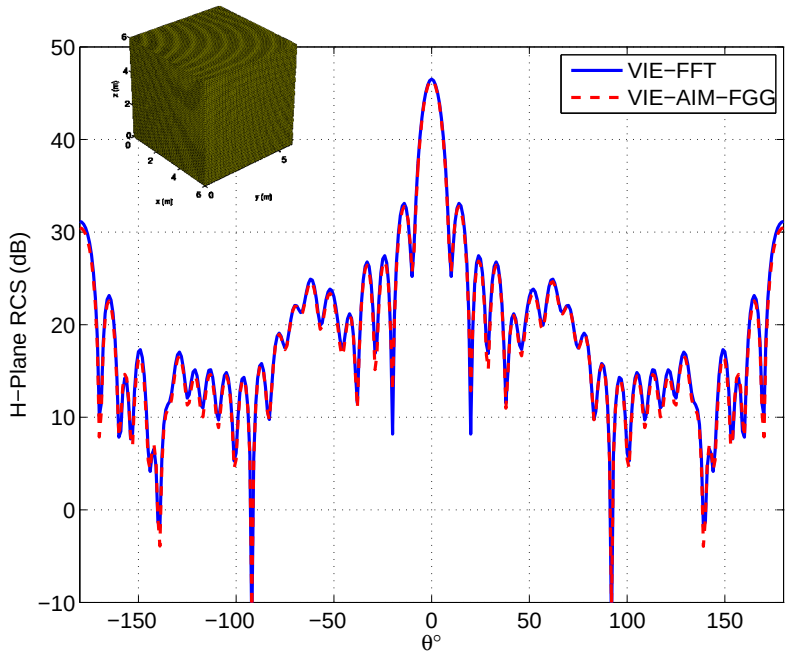

(b)

Figure 4.7: Bistatic RCS of a dielectric cube of edge length 6 m, with $\varepsilon_r = 2.0$.

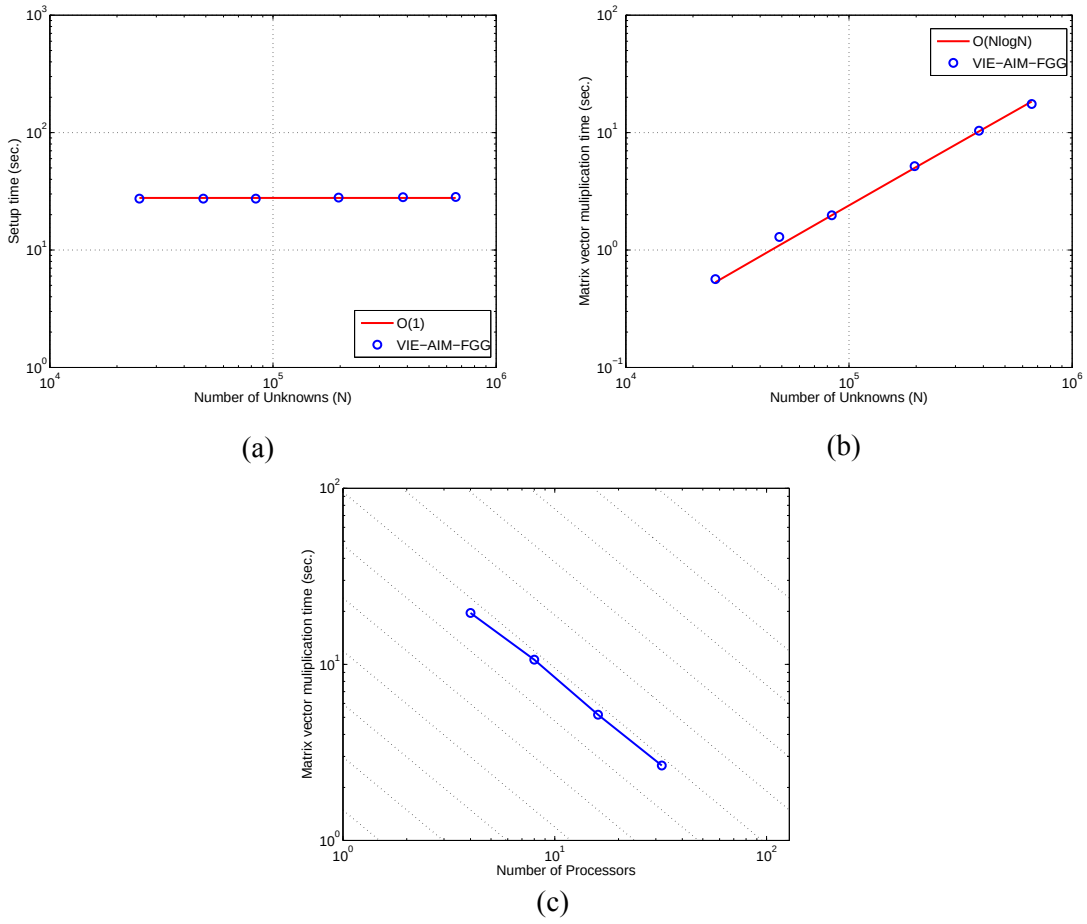

Figure 4.8: Computational Complexity and parallel efficiency of the VIE-AIM-FGG solver. Dashed lines in (c) represent the ideal scaling lines with respect to number of processors.

CHAPTER 5
Finite Element Boundary Integral Method

5.1 Formulation

Consider a penetrable inhomogeneous scatterer D residing in unbounded free-space. Let $\{\varepsilon(\mathbf{r}), \mu(\mathbf{r})\}$ and $\{\varepsilon_0, \mu_0\}$ denote the permittivity and permeability of D and free-space, respectively. The scatterer is illuminated by external incident electric and fields $\mathbf{E}^i(\mathbf{r})$ and $\mathbf{H}^i(\mathbf{r})$. We wish to find the total electric and magnetic fields everywhere in space. Maxwell's equations state that the electric and magnetic fields $\mathbf{E}(\mathbf{r})$ and $\mathbf{H}(\mathbf{r})$ satisfy

$$\nabla \times \mathbf{E}(\mathbf{r}) = -j\omega\mu(\mathbf{r})\mathbf{H}(\mathbf{r}) \tag{5.1}$$

$$\nabla \times \mathbf{H}(\mathbf{r}) = j\omega\varepsilon(\mathbf{r})\mathbf{E}(\mathbf{r}) \tag{5.2}$$

where ω is angular frequency of the incident field. Taking the curl of (5.1) and the substitution of (5.2) yields the vector wave equation for $\mathbf{E}(\mathbf{r})$

$$\nabla \times \frac{1}{\mu_r(\mathbf{r})} \nabla \times \mathbf{E}(\mathbf{r}) + k_0^2 \varepsilon_r(\mathbf{r})\mathbf{E}(\mathbf{r}) = 0 \quad \mathbf{r} \in D \tag{5.3}$$

where $\varepsilon_r(\mathbf{r}) = \varepsilon(\mathbf{r})/\varepsilon_0$ and $\mu_r(\mathbf{r}) = \mu(\mathbf{r})/\mu_0$ are the relative permittivity and permeability of D, $k_0 = \omega\sqrt{\varepsilon_0\mu_0}$ is the free-space wavenumber. To numerical solve (5.3)

for $\mathbf{E}(\mathbf{r})$, D is discretized using tetrahedral elements, and $\mathbf{E}(\mathbf{r})$, $\mathbf{H}(\mathbf{r})$ are expanded in terms of edge based curl conforming volume basis functions $\mathbf{N}_k(\mathbf{r})$ [8] as

$$\mathbf{E}(\mathbf{r}) \cong \sum_{k=1}^{N_{FE}} E_k \mathbf{N}_k(\mathbf{r}) \tag{5.4}$$

$$\mathbf{H}(\mathbf{r}) \cong \sum_{k=1}^{N_{FE}} H_k \mathbf{N}_k(\mathbf{r}) \tag{5.5}$$

where $\{E_k,\ H_k\}$, k $= 1,..., N_{FE}$ are the electric and magnetic field unknowns. To solve for $\{E_k, H_k\}$, electric field vector wave equation is discretized in Galerkin weak form yielding the following N_{FE} equations in D

$$\begin{aligned} &\int_D \left[\frac{1}{\mu_r(\mathbf{r})} \nabla \times \mathbf{N}_k(\mathbf{r}) \cdot \nabla \times \mathbf{E}(\mathbf{r}) - k_0^2 \varepsilon_r(\mathbf{r}) \mathbf{N}_k(\mathbf{r}) \cdot \mathbf{E}(\mathbf{r}) \right] dv \\ &- jk_0 \int_S \mathbf{N}_k(\mathbf{r}) \cdot \left[\hat{\mathbf{n}}(\mathbf{r}) \times \overline{\mathbf{H}}(\mathbf{r}) \right] ds = 0, \quad k = 1,..., N^{FE} \end{aligned} \tag{5.6}$$

where S is the closed surface bounding D, $\hat{\mathbf{n}}(\mathbf{r})$ is the outward pointing unit vector normal to S, and $\overline{\mathbf{H}}(\mathbf{r}) = Z_0 \mathbf{H}(\mathbf{r})$ with $Z_0 = \sqrt{\mu_0/\varepsilon_0}$. In obtaining (5.6), a vector identity and the divergence theorem is used to transfer the curl operator onto the basis function $\mathbf{N}_k(\mathbf{r})$ and to form the surface integral. Substitution of (5.4) and (5.5) into (5.6), and rearranging unknowns and equations yields the matrix system

$$\begin{bmatrix} \mathbf{A}^{II} & \mathbf{A}^{IB} & \mathbf{0} \\ \mathbf{A}^{BI} & \mathbf{A}^{BB} & \mathbf{B} \end{bmatrix} \cdot \begin{bmatrix} \mathbf{E}^I \\ \mathbf{E}^B \\ \mathbf{H}^B \end{bmatrix} = \begin{bmatrix} \mathbf{0} \\ \mathbf{0} \end{bmatrix} \tag{5.7}$$

where $\mathbf{E}^I$ is a $N_{FE}^I -$ vector of electric field unknowns in D, $\mathbf{E}^B$ and $\mathbf{H}^B$ are $N_{FE}^B -$ vectors of electric and magnetic field unknowns on S. Clearly, $N_{FE} = N_{FE}^I + N_{FE}^B$. $\mathbf{A}^{II}$, $\mathbf{A}^{IB}$, $\mathbf{A}^{BI}$, $\mathbf{A}^{BB}$, and $\mathbf{B}$ are the well-known sparse FE sub-matrices whose entries are given by

$$\mathbf{A}(k,k') = \int_D \left[\frac{1}{\mu_r(\mathbf{r})} \nabla \times \mathbf{N}_k(\mathbf{r}) \cdot \nabla \times \mathbf{N}_{k'}(\mathbf{r}) - k_0^2 \varepsilon_r(\mathbf{r}) \mathbf{N}_k(\mathbf{r}) \cdot \mathbf{N}_{k'}(\mathbf{r}) \right] dv \tag{5.8}$$

$$\mathbf{B}(k,k') = -jk_0 \int_S \mathbf{N}_k(\mathbf{r}) \cdot \left[\hat{\mathbf{n}} \times \mathbf{N}_{k'}(\mathbf{r}) \right] ds. \tag{5.9}$$

For a unique solution of $\mathbf{E}$ and $\mathbf{H}$, an auxiliary equation must be introduced to (5.7). This is done by formulating a combined field integral equation on surface S. Let $\mathbf{J}(\mathbf{r})$ and $\mathbf{M}(\mathbf{r})$ represent the surface electric and magnetic currents induced on S in response to the excitation $\mathbf{E}^i$ and $\mathbf{H}^i$. Enforcing the boundary conditions on electric and magnetic fields tangential so S yields the electric and magnetic field integral equations (EFIE and MFIE); a CFIE is obtained by linearly combining EFIE and MFIE

$$\hat{\mathbf{n}} \times \left[\mathcal{L}(\bar{\mathbf{J}}) - \mathcal{K}(\mathbf{M}) \right] = \hat{\mathbf{n}} \times \mathbf{E}^i(\mathbf{r}) \quad \text{(EFIE)}, \tag{5.10}$$

$$\hat{\mathbf{n}} \times \left[\mathcal{K}(\bar{\mathbf{J}}) + \mathcal{L}(\mathbf{M}) \right] = \hat{\mathbf{n}} \times \bar{\mathbf{H}}^i(\mathbf{r}) \quad \text{(MFIE)}, \tag{5.11}$$

$$\text{CFIE=EFIE+MFIE}. \tag{5.12}$$

Here, $\mathbf{r}$ is an observation point exterior to D, and $\bar{\mathbf{J}}(\mathbf{r}) = Z_0 \mathbf{J}(\mathbf{r})$ and $\bar{\mathbf{H}}^i(\mathbf{r}) = Z_0 \mathbf{H}^i(\mathbf{r})$. Integral operators $\mathcal{L}(\mathbf{X})$ and $\mathcal{K}(\mathbf{X})$ are given by

$$\mathcal{L}(\mathbf{X}) = jk_0 \int_S \left[\mathbf{X}(\mathbf{r}') + \frac{1}{k_0^2} \nabla \nabla' \cdot \mathbf{X}(\mathbf{r}') \right] g(\mathbf{r} - \mathbf{r}') ds' \tag{5.13}$$

$$\mathcal{K}(\mathbf{X}) = -\frac{\mathbf{X}}{2} + \int_S \mathbf{X}(\mathbf{r}') \times \nabla g(\mathbf{r} - \mathbf{r}') ds' \tag{5.14}$$

where $g(\mathbf{r} - \mathbf{r}') = e^{-jk_0|\mathbf{r}-\mathbf{r}'|} / (4\pi|\mathbf{r} - \mathbf{r}'|)$ is the free-space scalar Green function, $\mathbf{X}$ represents $\mathbf{J}(\mathbf{r})$ or $\mathbf{M}(\mathbf{r})$, and the integral in (5.14) is evaluated Cauchy principle value sense. (5.10) and (5.11) can be derived using the current-field relations

$$\mathbf{M}(\mathbf{r}) = \mathbf{E}(\mathbf{r}) \times \hat{\mathbf{n}}, \quad \mathbf{J}(\mathbf{r}) = \hat{\mathbf{n}} \times \mathbf{H}(\mathbf{r}) \quad \mathbf{r} \in S \tag{5.15}$$

To numerically solve (5.12), S is discretized using triangular elements that are conforming to the FE mesh, and the currents are expanded as

$$\mathbf{J}(\mathbf{r}) \cong \sum_{n=1}^{N_{BI}} I_n \mathbf{S}_n(\mathbf{r}), \quad \mathbf{M}(\mathbf{r}) \cong \sum_{n=1}^{N_{BI}} K_n \mathbf{S}_n(\mathbf{r}) \quad \mathbf{r} \in S \tag{5.16}$$

where $\{I_n, K_n\}$ and $\mathbf{S}_n(\mathbf{r})$ are unknown current coefficients and Rao-Wilton-Glisson (RWG) basis functions [54], respectively. Substitution of (5.16) into (5.12), testing the resulting EFIE with $\alpha \mathbf{S}_n(\mathbf{r}) + (1-\alpha)\hat{\mathbf{n}} \times \mathbf{S}_n(\mathbf{r})$, and MFIE with $\hat{\mathbf{n}} \times \mathbf{S}_n(\mathbf{r})$ yields the MOM system

$$\begin{bmatrix} \mathbf{Q} & \mathbf{P} \end{bmatrix} \begin{bmatrix} \mathbf{I} \\ \mathbf{K} \end{bmatrix} = \mathbf{V} \tag{5.17}$$

where $\mathbf{I}$ and $\mathbf{K}$ are $N_{BI}-$vectors of unknown current coefficients and tested incident fields, $\mathbf{P}$ and $\mathbf{Q}$ are $N_{BI} \times N_{BI}$ MOM impedance matrices. Their entries are

$$\mathbf{I}(k) = I_k, \quad (k = 1, ..., N_{BI}) \tag{5.18}$$

$$\mathbf{K}(k) = K_k, \quad (k = 1, ..., N_{BI}) \tag{5.19}$$

$$\mathbf{V}(k) = \left\langle \alpha \mathbf{S}_k(\mathbf{r}') + (1-\alpha)\hat{\mathbf{n}} \times \mathbf{S}_k(\mathbf{r}'), \mathbf{E}^i(\mathbf{r}') \right\rangle + \left\langle \hat{\mathbf{n}} \times \mathbf{S}_k(\mathbf{r}'), \mathbf{H}^i(\mathbf{r}') \right\rangle \quad k, k' = (1, ..., N_{BI}) \tag{5.20}$$

$$\mathbf{Q}(k,k') = \left\langle \alpha \mathbf{S}_k(\mathbf{r}) + (1-\alpha)\hat{\mathbf{n}} \times \mathbf{S}_k(\mathbf{r}), \mathcal{L}(\mathbf{S}_{k'}(\mathbf{r})) \right\rangle_S + \left\langle \hat{\mathbf{n}} \times \mathbf{S}_k(\mathbf{r}), \mathcal{K}(\mathbf{S}_{k'}(\mathbf{r})) \right\rangle_S \quad k, k' = (1, ..., N_{BI}) \tag{5.21}$$

$$\mathbf{P}(k,k') = \left\langle \hat{\mathbf{n}} \times \mathbf{S}_k(\mathbf{r}), \mathcal{L}(\mathbf{S}_{k'}(\mathbf{r})) \right\rangle_S - \left\langle \alpha \mathbf{S}_k(\mathbf{r}) + (1-\alpha)\hat{\mathbf{n}} \times \mathbf{S}_k(\mathbf{r}), \mathcal{K}(\mathbf{S}_{k'}(\mathbf{r})) \right\rangle_S \quad k, k' = (1, ..., N_{BI}) \tag{5.22}$$

where the inner products $\langle \ \rangle_S$ are defined as

$$\left\langle \mathbf{a}(\mathbf{r}), \mathbf{b}(\mathbf{r}) \right\rangle_S = \int_S \mathbf{a}(\mathbf{r}) \cdot \mathbf{b}(\mathbf{r}) \, ds. \tag{5.23}$$

The choice of testing functions for EFIE and MFIE is motivated by obtaining a better conditioned matrix at the end [29]. It should be noted that the FE basis functions $\mathbf{N}_k$ representing the fields on S are equivalent to $\hat{\mathbf{n}} \times \mathbf{S}_k$, and $N_{BI} = N_{FE}^B$. Therefore, $\mathbf{E}^B$ and $\mathbf{H}^B$ are equivalent to $\mathbf{K}$ and $\mathbf{I}$, respectively. Combination of (5.17) and (5.7) yields the final $N^{tot} \times N^{tot}$ FE-BI system

$$\begin{bmatrix} \mathbf{A}^{II} & \mathbf{A}^{IB} & \mathbf{0} \\ \mathbf{A}^{BI} & \mathbf{A}^{BB} & \mathbf{B} \\ \mathbf{0} & \mathbf{P} & \mathbf{Q} \end{bmatrix} \begin{bmatrix} \mathbf{E}^I \\ \mathbf{E}^B \\ \mathbf{H}^B \end{bmatrix} = \begin{bmatrix} \mathbf{0} \\ \mathbf{0} \\ \mathbf{V} \end{bmatrix}, \tag{5.24}$$

where $N^{tot} = N_{FE}^I + N_{BI}$.

5.2 Solution of FE-BI System

For large N^{tot}, (5.24) can not be solved directly and iterative solvers are called for. Iterative solvers repeatedly apply FE-BI matrix to trial vectors until the solution reaches a given accuracy. Therefore the computational requirements scale multiplicatively with the cost of applying FE-BI matrix to trial vectors and the number of iterations N_{iter}. N_{iter} is closely related to the condition number of the FE-BI matrix. Unfortunately, the condition number is affected by the existence of sparse FE sub-matrices. FE matrices are usually bad conditioned especially for non-uniform meshes and highly inhomogeneous materials [78]. As a remedy for this problem, a pre-conditioner that utilizes sparse direct solvers is employed [78]. Before solving (5.24) iteratively, 2×2 FE matrices

$$\mathbf{A} = \begin{bmatrix} \mathbf{A}^{II} & \mathbf{A}^{IB} \\ \mathbf{A}^{BI} & \mathbf{A}^{BB} \end{bmatrix} \tag{5.25}$$

are factorized using a sparse direct solver and the factorizations are stored in the computer memory. Availability of the inverse of FE matrices $\mathbf{A}^{-1}$ permits us to reformulate FE-BI equations and remove the FE unknowns $\mathbf{E}^I$ and $\mathbf{E}^B$ from the global

system of equations. Using the first two row blocks of (5.24) a relation between $\mathbf{E}^B$ and $\mathbf{H}^B$ is obtained

$$\mathbf{E}^B = -\mathbf{R}\cdot\mathbf{A}^{-1}\cdot\begin{bmatrix}\mathbf{0}\\ \mathbf{B}\end{bmatrix}\mathbf{H}^B. \tag{5.26}$$

Here $\mathbf{R}$ is a $N^{BI}\times N^{FE}$ sparse matrix selecting the boundary unknowns of the FE system

$$\mathbf{R} = \begin{bmatrix}\mathbf{0} & \mathbf{I}\end{bmatrix} \tag{5.27}$$

where $\mathbf{I}$ is a $N^{BI}\times N^{BI}$ identity matrix. Substituting (5.26) into (5.24) yields the reduced $N^{BI}\times N^{BI}$ FE-BI system of equations

$$\tilde{\mathbf{Z}}\cdot\mathbf{H}^B = \left[\mathbf{P}\cdot\mathbf{G}+\mathbf{Q}\right]\mathbf{H}^B = \mathbf{V} \tag{5.28}$$

where $\mathbf{G}$ is the compact notation

$$\mathbf{G} = -\mathbf{R}\cdot\mathbf{A}^{-1}\cdot\begin{bmatrix}\mathbf{0}\\ \mathbf{B}\end{bmatrix}. \tag{5.29}$$

In the iterative solution of (5.28), the matrix-vector multiplications pertinent to $\mathbf{P}$ and $\mathbf{Q}$ have $O\left(N^2\right)$ memory and CPU requirements. These requirements can be reduced using adaptive integral method (AIM) [17] or multilevel fast multipole [11, 79] accelerators. In this work AIM-FGG [20, 80] a memory-efficient extension of classical AIM is employed for this purpose to reduce the memory and CPU requirements to $O\left(N_c\right)$ and $O\left(N_c \log N_c\right)$, respectively. Here, $N_c \propto N$ for volumetric and quasi-planar scatterers, where the basis functions occupy most of the space enclosed by the domain D; $N_c \propto N^{1.5}$ for arbitrarily shaped three-dimensional (3D) surface scatterers. A detailed explanation of AIM-FGG acceleration technique can be found in Chapter 3.

5.3 Validation and Numerical Results

This section presents numerical results that validate the AIM-FGG accelerated FE-BI solver and demonstrate its efficiency. First, nonaccelerated FE-BI solver is used to analyze EM scattering from a dielectric sphere the results are compared to those obtained using exact analytical methods, i.e. Mie series solutions. Next, a series of simulations are performed for the same example by decreasing the discretization size and the accuracy of the FE-BI solver is compared to that of the VIE solver for the same discretization size. Finally AIM-FGG accelerated FE-BI is used to analyze scattering from a large dielectric cube and the results are compared to those obtained using the VIE-FFT solver. In the examples mesh density is represented by average edge length of the tetrahedral elements δ. Proposed solver is implemented using the popular message passing interface (MPI) programming model, and executed on clusters of processors to reduce the computational requirements. A transpose free quasi minimal residual (TFQMR) iterative scheme [55] is used to solve FE-BI matrix equations. Unless otherwise stated the tolerance of TFQMR is set to 10^{-6} and N_{iter} represents number of iterations required to reach this tolerance in the examples. All simulations are carried out on a cluster of dual-core 2.8 GHz AMD Opteron 2220 SE processors at the Center for Advanced Computing, University of Michigan. A commercially available software package PARDISO is used to compute the LU factorization of the sparse FE matrix $\mathbf{A}$, and apply forward and backward substitution.

5.3.1 Dielectric Sphere

The first test geometry is a dielectric sphere of radius $0.2\,\text{m}$, with relative permittivity $\varepsilon_r = 2.0$. The sphere is embedded in a free-space cube of edge length $0.4\,\text{m}$. A staircase approximation models the sphere as shown in the inset in Fig. 5.1(a). An non-accelerated FE-BI solver with parameter $\alpha = 0.4$ is used to compute the RCS of the

sphere and the results are compared to the Mie series solution. The sphere is illuminated by a plane wave

$$\mathbf{E}^i = \hat{\mathbf{p}} e^{-jk_0 \hat{\mathbf{k}} \mathbf{r}}, \tag{5.30}$$

with $\hat{\mathbf{p}} = \hat{\mathbf{x}}$ and $\hat{\mathbf{k}} = \hat{\mathbf{z}}$, and frequency $f =$ 300 MHz. In the simulation average edge length, number of unknowns, and number of iterations are $\delta = 0.025$ m, $N^{BI} = 4,608$, and $N_{iter} = 10$, respectively. Fig. 5.1 (a) shows the bistatic RCS of the sphere in E-plane ($\phi = 0°$) and H-plane ($\phi = 90°$).

Next, a series of simulations are performed for the first example by changing the discretization size δ from 0.1 m to 0.008 m while keeping other parameters intact. The accuracy of the solutions are measured quantitatively by computing the relative root-mean-square (RMS) error in the bistatic RCS

$$\text{RMS Error} = \frac{\sqrt{\sum_{i=1}^{N_s} \left| \sigma(\theta_i, \phi_i) - \sigma^{ref}(\theta_i, \phi_i) \right|^2}}{\sqrt{\sum_{i=1}^{N_s} \sigma^{ref}(\theta_i, \phi_i)^2}} \tag{5.31}$$

where σ and σ^{ref} represent the bistatic RCS obtained by the FE-BI solver and Mie series solution, respectively. In (5.31) N_s represents the total number of observation angles (θ_i) in E- $(\phi_i = 0°)$ and H- $(\phi_i = 90°)$ planes at which RCS is sampled. Same set of simulations are repeated for the VIE-FFT solver described in Chapter 3. Fig. 5.1 (b) shows the RMS error versus δ for both solvers. As expected FE-BI methods is less accurate for given mesh density.

5.3.2 Inhomogeneous Dielectric Cube

Next, EM scattering from an inhomogeneous dielectric cube of edge length 2.0 m, is analyzed. The cube is divided into two homogeneous layers in $x-$ direction. These layers have the relative permittivity $\varepsilon_{r1} = 2.5 - j0.25$ and $\varepsilon_{r1} = 2.0 - j0.5$. The incident field is a

$\hat{\mathbf{x}}$ polarized plane wave propagating in $\hat{\mathbf{z}}$ direction at $f = 300$ MHz. An AIM-FGG accelerated FE-BI solver with $\alpha = 0.4$ is used to compute the RCS of the sphere and the results are compared to those obtained using a non-accelerated FE-BI solver and a VIE-FFT solver. AIM grid size $\Delta x = \Delta y = \Delta z = 0.05$ m and mapping parameter $\mathcal{M} = 6$. In the FE-BI simulation $N = 28,800,$ and $N_{iter} = 20$, whereas in the VIE-FFT based simulation $N = 196,800,$ and $N_{iter} = 83$. In both simulations $\delta = 0.05$ m.. Fig. 5.2 (a) and (b) show the bistatic RCS of the cube in E-plane ($\phi = 0°$) and H-plane ($\phi = 90°$).

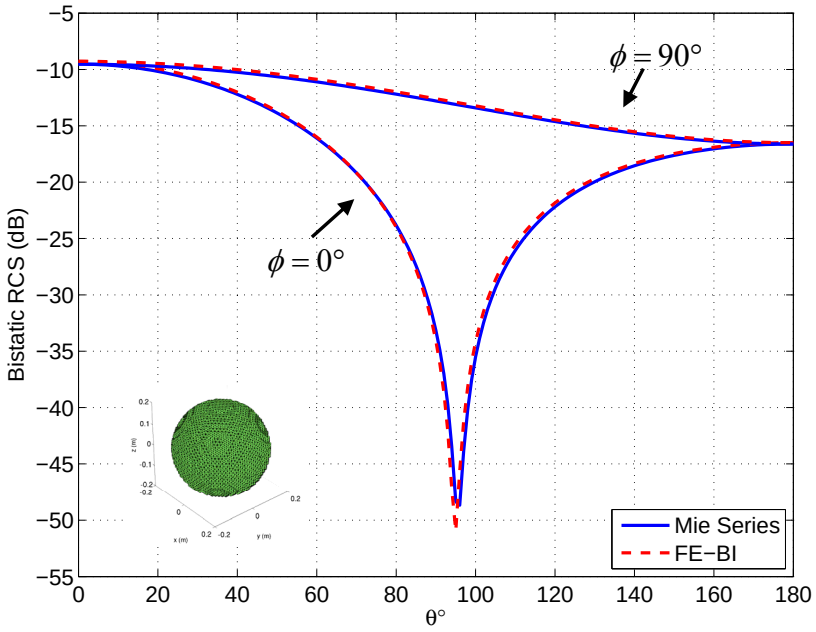

(a)

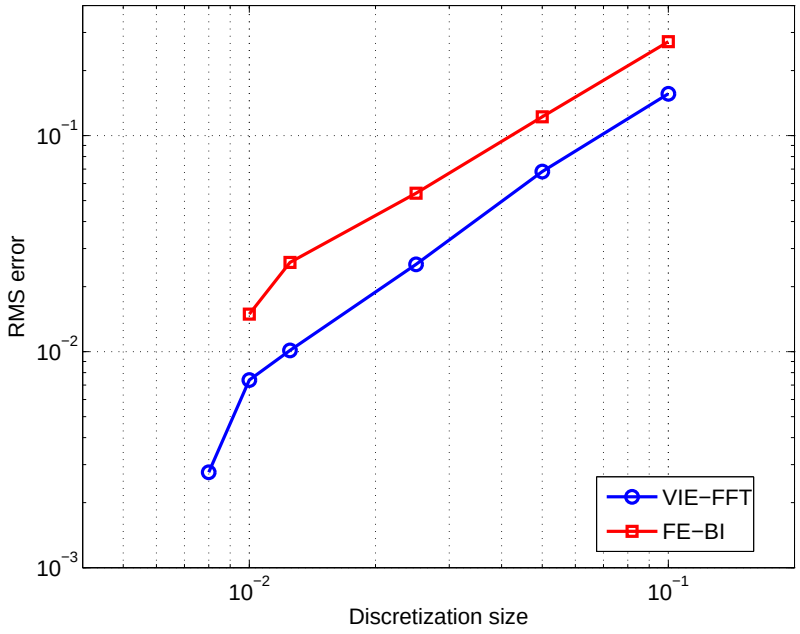

(b)

Figure 5.1: (a) Bistatic RCS of a dielectric sphere of radius 0.2 m and relative permittivity $\varepsilon_r = 2$. (b) Discretization size versus RMS error. A uniform rectangular grid is used to model the sphere. The staircase approximation of the sphere surface is depicted in the inset of (a).

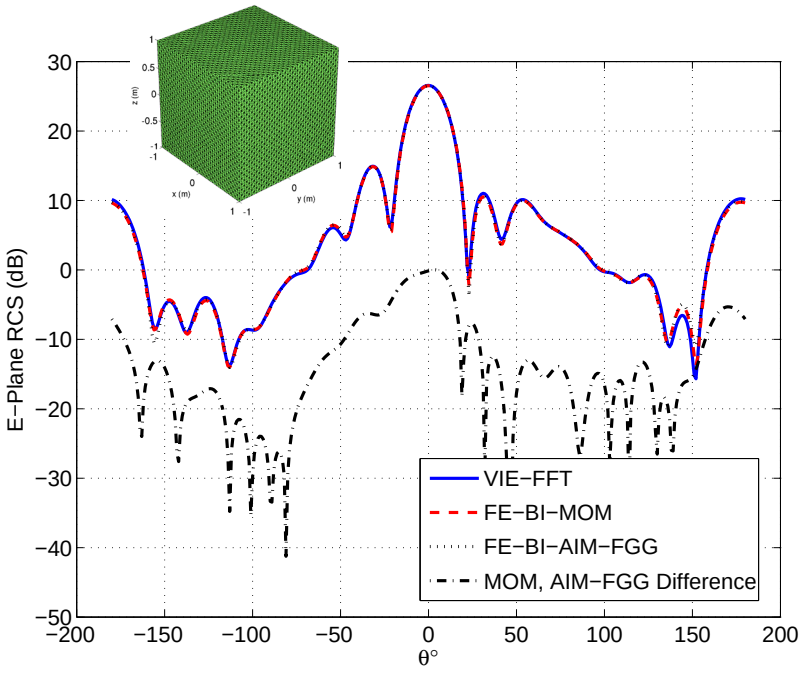

(a)

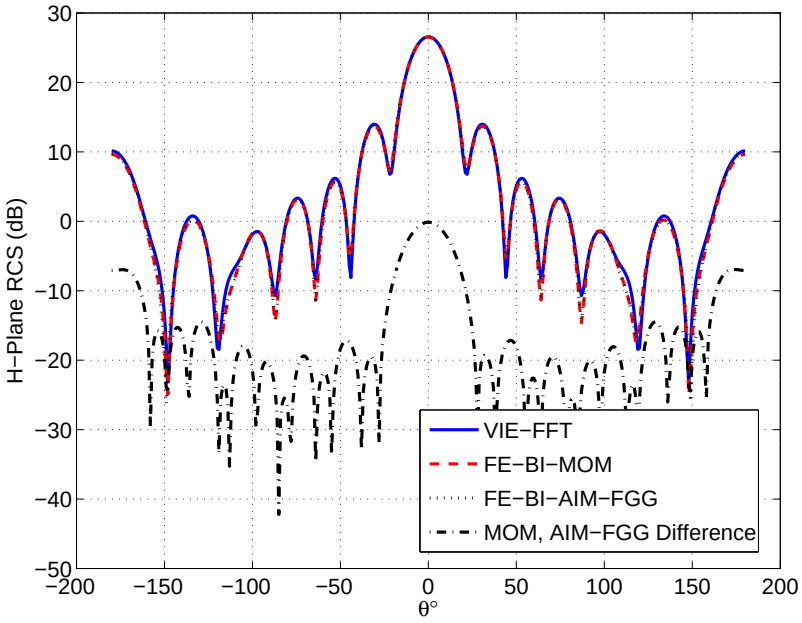

(b)

Figure 5.2: Bistatic RCS of an inhomogeneous dielectric cube of edge length 2 m.

CHAPTER 6
Domain Decomposition Based Finite Element-Boundary Integral-Volume Integral Equation Method

6.1 Introduction

This chapter details the proposed hybrid domain decomposition (DD) based finite element (FE) –boundary integral (BI) –volume integral equation (VIE) approach for analyzing electromagnetic (EM) wave scattering from complex inhomogeneous structures. Section 6.2 details the hybrid DD-FE-BI-VIE formulation and its MOM based discretization. Section 6.3 presents a memory and CPU time efficient approach to solve the hybrid DD-FE-BI-VIE MOM system. Preliminary numerical results are presented in Subsection 6.4 to validate the accuracy of the proposed solver.

6.2 Formulation

Consider the EM wave scattering problem from a composite structure comprising PEC surfaces and arbitrarily inhomogeneous dielectric bodies Ω residing in unbounded free space. Let $\varepsilon(\mathbf{r})$ and ε_0 denote the permittivity of Ω and free-space, respectively. DD method begins with dividing Ω into N non-overlapping domains Ω_i,

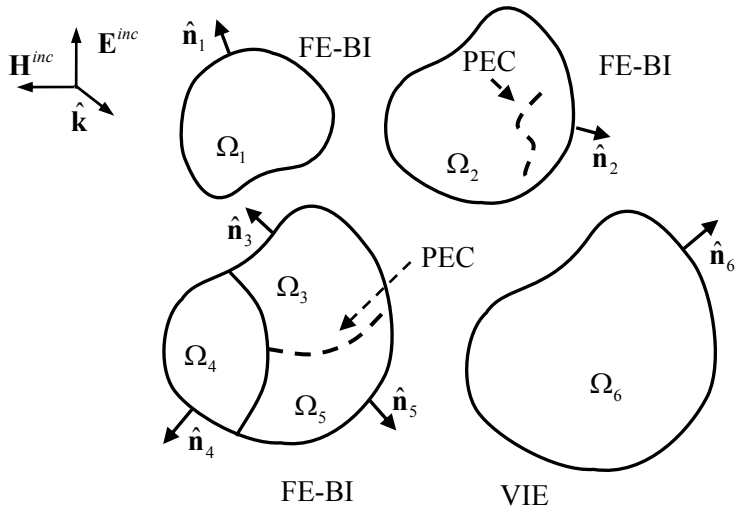

Figure 6.1: Composite structure and domain decomposition. Dielectric interfaces and PEC surfaces are represented by solid and dashed lines, respectively.

$i = 1,...,N$. Let N_{FE-BI} and N_{VIE} represent the number of domains modeled by FE-BI and VIE methods, respectively; and $N = N_{FE-BI} + N_{VIE}$. In Fig. 14 an example structure with $N_{FE-BI} = 5$ and $N_{VIE} = 1$ is illustrated. VIE domains are non-magnetic and have free-space permeability μ_0. A disjoint dielectric body can be represented by a single domain or partitioned into several domains if the electric size is too big. In general, domains are tailored to have similar sizes for computational efficiency. Let $\partial\Omega_i$, $i = 1,...,N_{FE-BI}$ denote the boundaries of FE-BI domains. PEC surfaces can reside on $\partial\Omega_i$ or can be enclosed in Ω_i, $i = 1,...,N_{FE-BI}$. The structure is excited by incident time-harmonic electric and magnetic fields $\mathbf{E}^{inc}(\mathbf{r})$ and $\mathbf{H}^{inc}(\mathbf{r})$ with angular frequency ω. In what follows time dependence $e^{-j\omega t}$ is assumed and suppressed.

The numerical analysis starts with subdividing FE-BI domains Ω_i, $i = 1,...,N_{FE-BI}$ into tetrahedral elements and expanding electric and magnetic fields $\mathbf{E}_i(\mathbf{r})$ and $\mathbf{H}_i(\mathbf{r})$ in each domain in terms of edge based curl-conforming volume basis functions $\mathbf{N}_{ij}(\mathbf{r})$ [8] as

$$\mathbf{E}_i(\mathbf{r}) \cong \sum_{j=1}^{N_i^{FE}} E_{ij}\mathbf{N}_{ij}(\mathbf{r}),\ \mathbf{H}_i(\mathbf{r}) \cong \sum_{j=1}^{N_i^{FE}} H_{ij}\mathbf{N}_{ij}(\mathbf{r}),\ i=1,...,N_{FE-BI}, \tag{6.1}$$

where N_i^{FE} is the number of FE unknowns, $\{E_{ij},\ H_{ij}\},\ j=1,...,N_i^{FE}$ are the electric and magnetic field unknowns in $\Omega_i,\ i=1,...,N_{FE-BI}$. To solve for these unknowns electric field vector wave equation is discretized in Galerkin weak-form yielding the following N_i^{FE} equations in Ω_i

$$\begin{aligned}&\int_{\Omega_i}\left[\frac{1}{\mu_r(\mathbf{r})}\nabla\times\mathbf{N}_{ij}(\mathbf{r})\cdot\nabla\times\mathbf{E}_i(\mathbf{r})-k_0^2\varepsilon_r(\mathbf{r})\mathbf{N}_{ij}(\mathbf{r})\cdot\mathbf{E}_i(\mathbf{r})\right]dv\\&-jk_0\int_{\partial\Omega_i}\mathbf{N}_{ij}(\mathbf{r})\cdot\left[\hat{\mathbf{n}}_i\times\overline{\mathbf{H}}_i(\mathbf{r})\right]ds=0,\ j=1,...,N_i^{FE}\end{aligned} \tag{6.2}$$

where $\varepsilon_r(\mathbf{r})=\varepsilon(\mathbf{r})/\varepsilon_0$ and $\mu_r(\mathbf{r})=\mu(\mathbf{r})/\mu_0$ are the relative permittivity and permeability of Ω, $k_0=\omega\sqrt{\varepsilon_0\mu_0}$ is the free-space wavenumber, $\hat{\mathbf{n}}_i$ is the outward pointing unit vector normal to $\partial\Omega_i$, and $\overline{\mathbf{H}}_i(\mathbf{r})=Z_0\mathbf{H}_i(\mathbf{r})$ with $Z_0=\sqrt{\mu_0/\varepsilon_0}$ being the free-space intrinsic impedance. Substitution of (6.1) into (6.2) yields the matrix equation (assuming there are no interior sources)

$$\begin{bmatrix}\mathbf{A}_i^{II} & \mathbf{A}_i^{IB} & \mathbf{0}\\ \mathbf{A}_i^{BI} & \mathbf{A}_i^{BB} & \mathbf{B}_i\end{bmatrix}\cdot\begin{bmatrix}\mathbf{E}_i^I\\ \mathbf{E}_i^B\\ \mathbf{H}_i^B\end{bmatrix}=\begin{bmatrix}\mathbf{0}\\ \mathbf{0}\end{bmatrix} \tag{6.3}$$

where $\mathbf{E}_i^I$ is the vector containing electric field unknowns in Ω_i, $\mathbf{E}_i^B$, and $\mathbf{H}_i^B$ are the vectors containing electric and magnetic field unknowns on $\partial\Omega_i$. $\mathbf{A}_i^{II}$, $\mathbf{A}_i^{IB}$, $\mathbf{A}_i^{BI}$, $\mathbf{A}_i^{BB}$, and $\mathbf{B}_i$ are the well-known sparse FE sub-matrices whose entries are given by

$$[\mathbf{A}_i]_{pq}=\int_{\Omega_i}\left[\frac{1}{\mu_r(\mathbf{r})}\nabla\times\mathbf{N}_{ip}(\mathbf{r})\cdot\nabla\times\mathbf{N}_{iq}(\mathbf{r})-k_0^2\varepsilon_r(\mathbf{r})\mathbf{N}_{ip}(\mathbf{r})\cdot\mathbf{N}_{iq}(\mathbf{r})\right]dv \tag{6.4}$$

$$[\mathbf{B}_i]_{pq}=-jk_0\int_{\partial\Omega_i}\mathbf{N}_{ip}(\mathbf{r})\cdot\left[\hat{\mathbf{n}}\times\mathbf{N}_{iq}(\mathbf{r})\right]ds. \tag{6.5}$$

Next step in the analysis is to build and discretize the coupled IEs for the exterior medium and VIE domains. In response to $\mathbf{E}^{inc}(\mathbf{r})$ and $\mathbf{H}^{inc}(\mathbf{r})$ electric and magnetic surface currents $\mathbf{J}_i^s(\mathbf{r})$ and $\mathbf{M}_i^s(\mathbf{r})$, and volume (polarization) currents $\mathbf{J}_i^v(\mathbf{r})$ are induced on $\partial\Omega_i,\ i=1,...,N_{FE-BI}$, and in $\Omega_i,\ i=(N_{FE-BI}+1),...,N$. These currents satisfy the following coupled set of boundary and volume IEs: (i) on $\partial\Omega_i,\ i=1,...,N_{FE-BI}$ electric and magnetic field IEs

$$\sum_{i=1}^{N_{FE-BI}}\left[\mathcal{L}_i^s\left(\overline{\mathbf{J}}_i^s\right)-\mathcal{K}_i^s\left(\mathbf{M}_i^s\right)\right]+\sum_{i=1}^{N_{VIE}}\mathcal{L}_i^v\left(\mathbf{J}_i^v\right)=\mathbf{E}^{inc}\left(\mathbf{r}\right)\ \forall\mathbf{r}\in\partial\Omega_i^+,\ i=1,...,N_{FE-BI} \tag{6.6}$$

$$\sum_{i=1}^{N_{FE-BI}}\left[\mathcal{K}_i^s\left(\overline{\mathbf{J}}_i^s\right)+\mathcal{L}_i^s\left(\mathbf{M}_i^s\right)\right]+\sum_{i=1}^{N_{VIE}}\mathcal{K}_i^v\left(\mathbf{J}_i^v\right)=\overline{\mathbf{H}}^{inc}\left(\mathbf{r}\right)\ \forall\mathbf{r}\in\partial\Omega_i^+,\ i=1,...,N_{FE-BI}, \tag{6.7}$$

(ii) in $\Omega_i,\ i=(N_{FE-BI}+1),...,N$ electric field IE

$$\sum_{i=1}^{N_{FE-BI}}\left[\mathcal{L}_i^s\left(\overline{\mathbf{J}}_i^s\right)-\mathcal{K}_i^s\left(\mathbf{M}_i^s\right)\right]+\sum_{i=1}^{N_{VIE}}\mathcal{L}_i^v\left(\mathbf{J}_i^v\right)+\mathbf{E}_i\left(\mathbf{r}\right)=\mathbf{E}^{inc}\left(\mathbf{r}\right)\ \forall\mathbf{r}\in\Omega_i,\ i=(N_{FE-BI}+1),...,N. \tag{6.8}$$

Here $\partial\Omega_i^+$ is the exterior side of Ω_i, $\overline{\mathbf{J}}_i^s=Z_0\mathbf{J}_i^s$ and $\overline{\mathbf{H}}^{inc}=Z_0\mathbf{H}^{inc}$, and $\mathbf{E}_i\left(\mathbf{r}\right)$ is the total electric field in $\Omega_i,\ i=(N_{FE-BI}+1),...,N$. In (6.6) and (6.7) the first and second terms on the left hand side of the equation represent the scattered fields from the FE-BI and VIE domains, respectively. Surface and volume integral operators $\mathcal{L}_i^s$, $\mathcal{K}_i^s$, $\mathcal{L}_i^v$, and $\mathcal{K}_i^v$ are defined as

$$\mathcal{L}_i^s\left(\mathbf{X}\right)=jk_0\int_{\partial\Omega_i}\left[\mathbf{X}(\mathbf{r}')+\frac{1}{k_0^2}\nabla\nabla'\cdot\mathbf{X}(\mathbf{r}')\right]g\left(\mathbf{r}-\mathbf{r}'\right)ds' \tag{6.9}$$

$$\mathcal{K}_i^s\left(\mathbf{X}\right)=-\frac{\mathbf{X}}{2}+\int_{\partial\Omega_i}\mathbf{X}(\mathbf{r}')\times\nabla g\left(\mathbf{r}-\mathbf{r}'\right)ds' \tag{6.10}$$

$$\mathcal{L}_i^v\left(\mathbf{X}\right)=\int_{\Omega_i}\left[j\omega\mu_0\mathbf{X}(\mathbf{r}')-\frac{1}{j\omega\varepsilon_0}\nabla\nabla'\cdot\mathbf{X}(\mathbf{r}')\right]g\left(\mathbf{r}-\mathbf{r}'\right)dv' \tag{6.11}$$

$$\mathcal{K}_i^v\left(\mathbf{X}\right)=Z_0\int_{\Omega_i}\mathbf{X}\left(\mathbf{r}'\right)\times\nabla g\left(\mathbf{r}-\mathbf{r}'\right)dv' \tag{6.12}$$

where $g\left(\mathbf{r}-\mathbf{r}'\right)=e^{-jk_0|\mathbf{r}-\mathbf{r}'|}\big/\left(4\pi\left|\mathbf{r}-\mathbf{r}'\right|\right)$ is the free-space scalar Green function. Integral in (6.10) is taken as Cauchy principal value. $\mathbf{J}_i^v\left(\mathbf{r}\right)$ is related to $\mathbf{E}_i\left(\mathbf{r}\right)$ and the electric flux density $\mathbf{D}_i\left(\mathbf{r}\right)=\varepsilon\left(\mathbf{r}\right)\mathbf{E}_i\left(\mathbf{r}\right)$ as

$$\mathbf{J}_i^v\left(\mathbf{r}\right)=j\omega\left[\varepsilon\left(\mathbf{r}\right)-\varepsilon_0\right]\mathbf{E}\left(\mathbf{r}\right)=j\omega\chi\left(\mathbf{r}\right)\mathbf{D}\left(\mathbf{r}\right)\ \forall\mathbf{r}\in\Omega_i,\ i=\left(N_{FE-BI}+1\right),...,N \tag{6.13}$$

where $\chi\left(\mathbf{r}\right)=1-\varepsilon_0\big/\varepsilon\left(\mathbf{r}\right)$ is the contrast parameter. Substitution of (6.13) into (6.6)-(6.7) yields S-EFIE, S-MFIE, and V-EFIE in $\mathbf{J}_i^s$, $\mathbf{M}_i^s$, and $\mathbf{D}_i$

$$\sum_{i=1}^{N_{FE-BI}}\left[\mathcal{L}_i^s\left(\overline{\mathbf{J}}_i^s\right)-\mathcal{K}_i^s\left(\mathbf{M}_i^s\right)\right]+\sum_{i=1}^{N_{VIE}}\mathcal{L}_i^{v,D}\left(\mathbf{D}_i\right)=\mathbf{E}^{inc}\left(\mathbf{r}\right)\ \forall\mathbf{r}\in\partial\Omega_i^+,\ i=1,...,N_{FE-BI} \tag{6.14}$$

$$\sum_{i=1}^{N_{FE-BI}}\left[\mathcal{K}_i^s\left(\overline{\mathbf{J}}_i^s\right)+\mathcal{L}_i^s\left(\mathbf{M}_i^s\right)\right]+\sum_{i=1}^{N_{VIE}}\mathcal{K}_i^{v,D}\left(\mathbf{D}_i\right)=\overline{\mathbf{H}}^{inc}\left(\mathbf{r}\right)\ \forall\mathbf{r}\in\partial\Omega_i^+,\ i=1,...,N_{FE-BI}, \tag{6.15}$$

$$\sum_{i=1}^{N_{FE-BI}}\left[\mathcal{L}_i^s\left(\overline{\mathbf{J}}_i^s\right)-\mathcal{K}_i^s\left(\mathbf{M}_i^s\right)\right]+\sum_{i=1}^{N_{VIE}}\mathcal{L}_i^{v,I}\left(\mathbf{D}_i\right)=\mathbf{E}^{inc}\left(\mathbf{r}\right)\ \forall\mathbf{r}\in\Omega_i,\ i=\left(N_{FE-BI}+1\right),...,N, \tag{6.16}$$

where $\mathcal{L}_i^{v,D}$, $\mathcal{K}_i^{v,D}$, and $\mathcal{L}_i^{v,I}$ are the complementary volume integral operators given by

$$\mathcal{L}_i^{v,D}\left(\mathbf{X}\right)=\int_{\Omega_i}\left\{-\omega^2\mu_0\left[\chi\left(\mathbf{r}'\right)\mathbf{X}\left(\mathbf{r}'\right)\right]+\frac{1}{\varepsilon_0}\nabla\nabla'\cdot\left[\chi\left(\mathbf{r}'\right)\mathbf{X}\left(\mathbf{r}'\right)\right]\right\}g\left(\mathbf{r}-\mathbf{r}'\right)dv', \tag{6.17}$$

$$\mathcal{K}_i^{v,D}\left(\mathbf{X}\right)=\frac{jk_0}{\varepsilon_0}\int_{\Omega_i}\left[\chi\left(\mathbf{r}'\right)\mathbf{X}\left(\mathbf{r}'\right)\right]\times\nabla g\left(\mathbf{r}-\mathbf{r}'\right)dv', \tag{6.18}$$

$$\mathcal{L}_i^{v,I}\left(\mathbf{X}\right)=\mathcal{L}_i^{v,D}\left(\mathbf{X}\right)+\frac{\mathbf{X}}{\varepsilon\left(\mathbf{r}\right)}. \tag{6.19}$$

To numerical solve the coupled set of equations (6.14)-(6.16) for $\overline{\mathbf{J}}_i$, $\mathbf{M}_i$, and $\mathbf{D}_i$ using MOM, surfaces $\partial\Omega_i,\ i=1,...,N_{FE-BI}$ and volumes $\Omega_i,\ i=\left(N_{FE-BI}+1\right),...,N$ are discretized by meshes of planar triangles and hexahedra and $\overline{\mathbf{J}}_i\left(\mathbf{r}\right)$, $\mathbf{M}_i\left(\mathbf{r}\right)$, and $\mathbf{D}_i\left(\mathbf{r}\right)$ are expanded as

$$\mathbf{J}_i(\mathbf{r}) \cong \sum_{j=1}^{N_i^{BI}} J_{ij}\mathbf{S}_{ij}^{RWG}(\mathbf{r}),\ \ \mathbf{M}_i(\mathbf{r}) \cong \sum_{j=1}^{N_i^{BI}} M_{ij}\mathbf{S}_{ij}^{RWG}(\mathbf{r}),\ \mathbf{r} \in \partial\Omega_i,\ i = 1,...,N_{FE-BI} \quad (6.20)$$

$$\mathbf{D}_i(\mathbf{r}) \cong \sum_{j=1}^{N_i^{VIE}} D_{ij}\mathbf{S}_{ij}^{RT}(\mathbf{r}),\ \mathbf{r} \in \Omega_i,\ i = (N_{FE-BI}+1),...,N \quad (6.21)$$

where $\{J_{ij}, M_{ij}\}$, $j = 1,...,N_i^{BI}$, D_{ij}, $j = 1,...,N_i^{VIE}$ are the unknown expansion coefficients, $\mathbf{S}_{ij}^{RWG}(\mathbf{r})$ are divergence conforming Rao-Wilton-Glisson (RWG) basis functions [54] defined on triangle pairs, $\mathbf{S}_{ij}^{RT}(\mathbf{r})$ are divergence conforming roof-top basis functions defined on hexahedron pairs [7, 75, 81], N_i^{BI} and N_i^{VIE} are the number of BI and VIE unknowns on $\partial\Omega_i$ and in Ω_i, respectively. Also $\chi(\mathbf{r})$ is approximated by pulse basis functions which assume constant values over each hexahedron. It should be noted that the FE basis functions $\mathbf{N}_{ij}(\mathbf{r})$ representing the fields on $\partial\Omega_i$ are equivalent to $\hat{\mathbf{n}} \times \mathbf{S}_{ij}^{RWG}(\mathbf{r})$, $\mathbf{r} \in \partial\Omega_i$, $i = 1,...,N_{FE-BI}$. Hence $\mathbf{E}_i^B$, $\mathbf{H}_i^B$ are related to $\mathbf{J}_i$, $\mathbf{M}_i$ as

$$\begin{bmatrix} \mathbf{E}_i^B \\ \mathbf{H}_i^B \end{bmatrix} = \begin{bmatrix} \mathbf{M}_i \\ \mathbf{J}_i \end{bmatrix},\ i = 1,...,N_{FE-BI}, \quad (6.22)$$

where $\mathbf{J}_i = \begin{bmatrix} J_{i1} & \dots & J_{iN_i^{BI}} \end{bmatrix}^T$, $\mathbf{M}_i = \begin{bmatrix} M_{i1} & \dots & M_{iN_i^{BI}} \end{bmatrix}^T$ are the vectors containing the unknown current coefficients; here superscript ^{T} represents the transpose operation. Therefore $\{\mathbf{E}_i^I, \mathbf{J}_i, \mathbf{M}_i\}$ are the only set of unknowns considered in FE-BI system of equations for Ω_i.

BI-VIE system of equations are discretized and coupled with the FE matrices (6.3) by taking the following steps: (i) (6.20) and (6.21) are substituted into (6.14)-(6.16). (ii) The resulting equations are tested with $\alpha\mathbf{S}_{ij}^{RWG}(\mathbf{r}) + (1-\alpha)\hat{\mathbf{n}}_i \times \mathbf{S}_{ij}^{RWG}(\mathbf{r})$, $\hat{\mathbf{n}}_i \times \mathbf{S}_{ij}^{RWG}(\mathbf{r})$, and $\chi(\mathbf{r})\mathbf{S}_{ij}^{RT}(\mathbf{r})$, respectively. Here, α is a real parameter changing from 0 to 1. The choice of testing functions for EFIE and MFIE is motivated by obtaining a better conditioned matrix at the end [29]. (iii) First two equations are linearly combined to obtain combined field integral equation (CFIE) type BI-VIE matrices. (iv) Finally the

resulting BI-VIE matrices are augmented with (6.3) yielding the $N^{tot} \times N^{tot}$ global system of equations is assembled by combining matrices from all domains

$$\mathbf{Z} \cdot \mathbf{I} = \begin{bmatrix} \mathbf{Z}^{FE-BI,FE-BI} & \mathbf{Z}^{FE-BI,VIE} \\ \mathbf{Z}^{VIE,FE-BI} & \mathbf{Z}^{VIE,VIE} \end{bmatrix} \cdot \begin{bmatrix} \mathbf{I}^{FE-BI} \\ \mathbf{I}^{VIE} \end{bmatrix} = \begin{bmatrix} \mathbf{V}^{FE-BI} \\ \mathbf{V}^{VIE} \end{bmatrix}, \tag{6.23}$$

where N^{tot} is the total number of unknowns

$$N^{tot} = \sum_{i=1}^{N^{FE-BI}} N_i^{BI} + N_i^{FE} + \sum_{i=N^{FE-BI}+1}^{N} N_i^{VIE}. \tag{6.24}$$

Here $\mathbf{V}^{FE-BI} = \begin{bmatrix} \mathbf{V}_1^{FE-BI} & \cdots & \mathbf{V}_{N^{FE-BI}}^{FE-BI} \end{bmatrix}^T$ and $\mathbf{V}^{VIE} = \begin{bmatrix} \mathbf{V}_{N^{FE-BI}+1}^{VIE} & \cdots & \mathbf{V}_N^{VIE} \end{bmatrix}^T$ represent the tested incident fields on $\partial\Omega_i,\ i = 1,...,N^{FE-BI}$ and in $\Omega_i,\ i = N^{FE-BI+1},...,N,$ respectively. More specifically

$$\mathbf{V}_i^{FE-BI} = \begin{bmatrix} \mathbf{0} \\ \mathbf{0} \\ \mathbf{V}_i^{BI} \end{bmatrix}, \tag{6.25}$$

and the entries of $\mathbf{V}_i^{BI},\ \mathbf{V}_N^{VIE}$ are given by

$$\left[\mathbf{V}_i^{BI}\right]_p = \left\langle \mathbf{S}_{ip}^{RWG}(\mathbf{r}), \mathbf{E}^{inc}(\mathbf{r}) \right\rangle_{\partial\Omega_i} + \left\langle \hat{\mathbf{n}} \times \mathbf{S}_{ip}^{RWG}(\mathbf{r}), \overline{\mathbf{H}}^{inc}(\mathbf{r}) \right\rangle_{\partial\Omega_i},\ i = 1,...,N^{FE-BI}. \tag{6.26}$$

$$\left[\mathbf{V}_i^{VIE}\right]_p = \left\langle \chi(\mathbf{r}) \mathbf{S}_{ip}^{RT}(\mathbf{r}), \mathbf{E}^{inc}(\mathbf{r}) \right\rangle_{\Omega_i},\ i = \left(N^{FE-BI}+1\right),...,N \tag{6.27}$$

with the inner products $\langle\ \rangle_{\partial\Omega_i}$ and $\langle\ \rangle_{\Omega_i}$ defined as

$$\left\langle \mathbf{a}(\mathbf{r}), \mathbf{b}(\mathbf{r}) \right\rangle_{\partial\Omega_i} = \int_{\partial\Omega_i} \mathbf{a}(\mathbf{r}) \cdot \mathbf{b}(\mathbf{r})\, ds, \tag{6.28}$$

$$\left\langle \mathbf{a}(\mathbf{r}), \mathbf{b}(\mathbf{r}) \right\rangle_{\Omega_i} = \int_{\Omega_i} \mathbf{a}(\mathbf{r}) \cdot \mathbf{b}(\mathbf{r})\, dv. \tag{6.29}$$

In (6.23) $\mathbf{I} = \begin{bmatrix} \mathbf{I}^{FE-BI} & \mathbf{I}^{VIE} \end{bmatrix}^T$ is the unknown coefficient vector with $\mathbf{I}^{FE-BI} = \begin{bmatrix} \mathbf{I}_1^{FE-BI} & \cdots & \mathbf{I}_{N_{FE-BI}}^{FE-BI} \end{bmatrix}^T$ and $\mathbf{I}^{VIE} = \begin{bmatrix} \mathbf{D}_{N^{FE-BI}+1} & \cdots & \mathbf{D}_N \end{bmatrix}^T$ being the individual FE-BI and VIE unknown coefficient vectors. $\mathbf{I}_i^{FE-BI} = \begin{bmatrix} \mathbf{E}_i^I & \mathbf{M}_i & \mathbf{J}_i \end{bmatrix},\ i = 1,...,N_{FE-BI}$ and

$\mathbf{D}_i$, $i=\left(N_{FE-BI}+1\right),...,N$ are the FE-BI and VIE unknown coefficient vectors, respectively.

In the remainder of this section, sub-matrices $\mathbf{Z}^{FE-BI,FE-BI}$, $\mathbf{Z}^{FE-BI,VIE}$, $\mathbf{Z}^{VIE,FE-BI}$, and $\mathbf{Z}^{VIE,VIE}$ are described. Sub-matrix $\mathbf{Z}^{FE-BI,FE-BI}$ is a collocation of FE-BI matrices $\mathbf{Z}_{ij}^{FE-BI,FE-BI}$ from every domain pair $\left\{\Omega_i,\Omega_j\right\}$, $\left\{i,j\right\}\in\left\{1,...,N_{FE-BI}\right\}$

$$\mathbf{Z}^{FE-BI,FE-BI}=\begin{bmatrix}\mathbf{Z}_{11}^{FE-BI,FE-BI} & \mathbf{Z}_{12}^{FE-BI,FE-BI} & \cdots & \mathbf{Z}_{1N^{FE-BI}}^{FE-BI,FE-BI}\\ \mathbf{Z}_{21}^{FE-BI,FE-BI} & \mathbf{Z}_{22}^{FE-BI,FE-BI} & \cdots & \mathbf{Z}_{2N^{FE-BI}}^{FE-BI,FE-BI}\\ \vdots & \vdots & \ddots & \vdots\\ \mathbf{Z}_{N^{FE-BI}1}^{FE-BI,FE-BI} & \mathbf{Z}_{N^{FE-BI}2}^{FE-BI,FE-BI} & \cdots & \mathbf{Z}_{N^{FE-BI}N^{FE-BI}}^{FE-BI,FE-BI}\end{bmatrix}, \tag{6.30}$$

where

$$\mathbf{Z}_{ii}^{FE-BI,FE-BI}=\begin{bmatrix}\mathbf{A}_i^{II} & \mathbf{A}_i^{IB} & \mathbf{0}\\ \mathbf{A}_i^{BI} & \mathbf{A}_i^{BB} & \mathbf{B}_i\\ \mathbf{0} & \mathbf{P}_{ii} & \mathbf{Q}_{ii}\end{bmatrix},\quad \left\{i\right\}\in\left\{1,...,N_{FE-BI}\right\}, \tag{6.31}$$

$$\mathbf{Z}_{ij}^{FE-BI,FE-BI}=\begin{bmatrix}\mathbf{0} & \mathbf{0} & \mathbf{0}\\ \mathbf{0} & \mathbf{0} & \mathbf{0}\\ \mathbf{0} & \mathbf{P}_{ij} & \mathbf{Q}_{ij}\end{bmatrix},\quad \left\{i,j\right\}\in\left\{1,...,N_{FE-BI}\right\},\left(i\neq j\right) \tag{6.32}$$

In (6.31) $\mathbf{P}_{ij}$, $\mathbf{Q}_{ij}$ are the CFIE type BI matrices whose entries are

$$\begin{aligned}\left[\mathbf{P}_{ij}\right]_{pq}&=-\left\langle\alpha\mathbf{S}_{ip}^{RWG}\left(\mathbf{r}\right)+\left(1-\alpha\right)\hat{\mathbf{n}}_i\times\mathbf{S}_{ip}^{RWG}\left(\mathbf{r}\right),\mathcal{K}_j^s\left(\mathbf{S}_{jq}^{RWG}\right)\right\rangle_{\partial\Omega_i}\\&+\left\langle\hat{\mathbf{n}}_i\times\mathbf{S}_{ip}^{RWG}\left(\mathbf{r}\right),\mathcal{L}_j^s\left(\mathbf{S}_{jq}^{RWG}\right)\right\rangle_{\partial\Omega_i},\ p\in\left\{1,...,N_i^{BI}\right\},\ q\in\left\{1,...,N_j^{BI}\right\}\end{aligned} \tag{6.33}$$

$$\begin{aligned}\left[\mathbf{Q}_{ij}\right]_{pq}&=\left\langle\alpha\mathbf{S}_{ip}^{RWG}\left(\mathbf{r}\right)+\left(1-\alpha\right)\hat{\mathbf{n}}\times\mathbf{S}_{ip}^{RWG}\left(\mathbf{r}\right),\mathcal{L}_j^s\left(\mathbf{S}_{jq}^{RWG}\right)\right\rangle_{\partial\Omega_i}\\&+\left\langle\hat{\mathbf{n}}\times\mathbf{S}_{ip}^{RWG}\left(\mathbf{r}\right),\mathcal{K}_j^s\left(\mathbf{S}_{jq}^{RWG}\right)\right\rangle_{\partial\Omega_i},\ p\in\left\{1,...,N_i^{BI}\right\},\ q\in\left\{1,...,N_j^{BI}\right\}.\end{aligned} \tag{6.34}$$

Sub-matrix $\mathbf{Z}^{FE-BI,VIE}$ accounts for the interactions between surface- test and volume-source basis functions and it can be represented by

$$\mathbf{Z}^{FE-BI,VIE}=\begin{bmatrix}\mathbf{Z}^{FE-BI,VIE}_{1\left(N^{FE-BI}+1\right)} & \mathbf{Z}^{FE-BI,VIE}_{1\left(N^{FE-BI}+2\right)} & \cdots & \mathbf{Z}^{FE-BI,VIE}_{1N}\\ \mathbf{Z}^{FE-BI,VIE}_{2\left(N^{FE-BI}+1\right)} & \mathbf{Z}^{FE-BI,VIE}_{2\left(N^{FE-BI}+2\right)} & \cdots & \mathbf{Z}^{FE-BI,VIE}_{2N}\\ \vdots & \vdots & \ddots & \vdots\\ \mathbf{Z}^{FE-BI,VIE}_{N^{FE-BI}1} & \mathbf{Z}^{FE-BI,VIE}_{N^{FE-BI}2} & \cdots & \mathbf{Z}^{FE-BI,VIE}_{N^{FE-BI}N}\end{bmatrix}, \tag{6.35}$$

where $\mathbf{Z}^{FE-BI,VIE}_{ij}$ is the compact notation

$$\mathbf{Z}^{FE-BI,VIE}_{ij}=\begin{bmatrix}\mathbf{0}\\ \mathbf{0}\\ \mathbf{Z}^{BI,VIE}_{ij}\end{bmatrix},\ i\in\left\{1,...,N_{FE-BI}\right\},\ \mathrm{j}\in\left\{N_{FE-BI}+1,...,N\right\} \tag{6.36}$$

with

$$\begin{aligned}\left[\mathbf{Z}^{BI,VIE}_{ij}\right]_{pq}&=\left\langle\mathbf{S}^{RWG}_{ip},\mathcal{L}^{v,D}_{i}\left(\mathbf{S}^{RT}_{jq}\right)\right\rangle_{\partial\Omega_i}+\left\langle\hat{\mathbf{n}}_i\times\mathbf{S}^{RWG}_{ip},\mathcal{K}^{v,D}_{i}\left(\mathbf{S}^{RT}_{jq}\right)\right\rangle_{\partial\Omega_i},\\ &p\in\left\{1,...,N^{BI}_{i}\right\},\ q\in\left\{1,...,N^{VIE}_{j}\right\}.\end{aligned} \tag{6.37}$$

Similarly $\mathbf{Z}^{VIE,FE-BI}_{ij}$ accounts for the interactions between volume- test and surface-source basis functions

$$\mathbf{Z}^{VIE,FE-BI}=\begin{bmatrix}\mathbf{Z}^{VIE,FE-BI}_{\left(N^{FE-BI}+1\right)1} & \mathbf{Z}^{VIE,FE-BI}_{\left(N^{FE-BI}+1\right)2} & \cdots & \mathbf{Z}^{VIE,FE-BI}_{\left(N^{FE-BI}+1\right)N^{FE-BI}}\\ \mathbf{Z}^{VIE,FE-BI}_{\left(N^{FE-BI}+1\right)1} & \mathbf{Z}^{VIE,FE-BI}_{\left(N^{FE-BI}+2\right)2} & \cdots & \mathbf{Z}^{VIE,FE-BI}_{\left(N^{FE-BI}+2\right)N^{FE-BI}}\\ \vdots & \vdots & \ddots & \vdots\\ \mathbf{Z}^{VIE,FE-BI}_{N1} & \mathbf{Z}^{FE-BI,VIE}_{N2} & \cdots & \mathbf{Z}^{VIE,FE-BI}_{NN^{FE-BI}}\end{bmatrix}, \tag{6.38}$$

where $\mathbf{Z}^{FE-BI,VIE}_{ij}$ is the compact notation

$$\mathbf{Z}^{VIE,FE-BI}_{ij}=\begin{bmatrix}\mathbf{0} & \mathbf{Z}^{VIE,BI-E}_{ij} & \mathbf{Z}^{VIE,BI-H}_{ij}\end{bmatrix},\ i\in\left\{N_{FE-BI}+1,...,N\right\},\ \mathrm{j}\in\left\{1,...,N_{FE-BI}\right\} \tag{6.39}$$

with

$$\left[\mathbf{Z}^{VIE,BI-E}_{ij}\right]_{pq}=\left\langle\chi\left(\mathbf{r}\right)\mathbf{S}^{RT}_{ip}\left(\mathbf{r}\right),\mathcal{L}^{s}_{i}\left(\mathbf{S}^{RWG}_{jq}\right)\right\rangle_{\Omega_i},\ p\in\left\{1,...,N^{VIE}_{i}\right\},\ j\in\left\{1,...,N^{BI}_{j}\right\}, \tag{6.40}$$

$$\left[\mathbf{Z}^{VIE,BI-H}_{ij}\right]_{pq}=-\left\langle\chi\left(\mathbf{r}\right)\mathbf{S}^{RT}_{ip},\mathcal{K}^{s}_{i}\left(\mathbf{S}^{RWG}_{jq}\right)\right\rangle_{\Omega_i},\ p\in\left\{1,...,N^{VIE}_{i}\right\},\ j\in\left\{1,...,N^{BI}_{j}\right\}. \tag{6.41}$$

Finally, the sub-matrix $\mathbf{Z}_{ij}^{VIE,VIE}$ accounting for the interactions between volume-test and volume-source basis functions is given by

$$\mathbf{Z}^{VIE,VIE}=\begin{bmatrix} \mathbf{Z}^{VIE,VIE}_{\left(N^{FE-BI}+1\right)\left(N^{FE-BI}+1\right)} & \mathbf{Z}^{VIE,VIE}_{\left(N^{FE-BI}+1\right)\left(N^{FE-BI}+2\right)} & \cdots & \mathbf{Z}^{VIE,VIE}_{\left(N^{FE-BI}+1\right)N} \\ \mathbf{Z}^{VIE,VIE}_{\left(N^{FE-BI}+2\right)\left(N^{FE-BI}+1\right)} & \mathbf{Z}^{VIE,VIE}_{\left(N^{FE-BI}+2\right)\left(N^{FE-BI}+2\right)} & \cdots & \mathbf{Z}^{VIE,VIE}_{\left(N^{FE-BI}+2\right)N} \\ \vdots & \vdots & \ddots & \vdots \\ \mathbf{Z}^{VIE,VIE}_{N\left(N^{FE-BI}+1\right)} & \mathbf{Z}^{VIE,VIE}_{N\left(N^{FE-BI}+2\right)} & \cdots & \mathbf{Z}^{VIE,VIE}_{NN} \end{bmatrix}, \tag{6.42}$$

where

$$\begin{aligned} \left[\mathbf{Z}_{ij}^{VIE,VIE}\right]_{pq} &= \left\langle \chi(\mathbf{r})\mathbf{S}_{ip}^{RT}(\mathbf{r}), \mathcal{L}_i^{v,I}\left(\mathbf{S}_{jq}^{RT}\right)\right\rangle_{\Omega_i},\ \{i,j\}\in\{N_{FE-BI}+1,...,N\}, \\ & p\in\left\{1,...,N_i^{VIE}\right\},\ q\in\left\{1,...,N_j^{VIE}\right\}. \end{aligned} \tag{6.43}$$

6.3 Solution of DD-FE-BI-VIE-MOM System

For large N^{tot} (6.23) can not be solved directly and iterative solvers are called for. Iterative solvers repeatedly apply $\mathbf{Z}$ to trial vectors until the solution reaches a given accuracy. Therefore the computational requirements scale multiplicatively with the cost of applying $\mathbf{Z}$ to trial vectors and the number of iterations N_{iter}. The former can be reduced by using adaptive integral method (AIM) [17] or multilevel fast multipole [11, 79] accelerators to accelerate the matrix-vector multiplications pertinent to BI-VIE coupled system. In this work AIM-FGG [20, 80] a memory-efficient extension of classical AIM is employed for this purpose.

N_{iter} is closely related to the condition number of the global system matrix $\mathbf{Z}$. Unfortunately, the condition number of $\mathbf{Z}$ is affected by the existence of sparse FE sub-matrices. FE matrices are usually bad conditioned especially for non-uniform meshes and highly inhomogeneous materials [78]. As a remedy for this problem, a pre-conditioner that utilizes sparse direct solvers is employed [78]. Before solving (6.23)

iteratively, FE matrices $\mathbf{A}_i,\ i=1,...,N^{FE-BI}$ are factorized using a sparse direct solver and the factorizations are stored in the computer memory. Availability of the inverse of FE matrices $\mathbf{A}_i^{-1}$ permits us to reformulate FE-BI equations and remove the unknowns $\mathbf{E}_i^I$, $\mathbf{M}_i$ from the global system of equations as follows. A relation between $\mathbf{M}_i$ and $\mathbf{J}_i$ is obtained from (6.3) using $\mathbf{A}_i^{-1}$

$$\mathbf{M}_i = -\mathbf{Q}_i^H \cdot \mathbf{A}_i^{-1} \cdot \begin{bmatrix} \mathbf{0} \\ \mathbf{B}_i \end{bmatrix} \mathbf{J}_i \ \ i \in \left\{1,..,N^{FE-BI}\right\} \tag{6.44}$$

Here $N_i^{BI} \times N_i^{FE}$ matrix $\mathbf{Q}_i^H$ define the operator for selecting the boundary unknowns from the FE matrix given by

$$\mathbf{Q}_i^H = \begin{bmatrix} \mathbf{0} & \mathbf{I} \end{bmatrix}, \tag{6.45}$$

where $\mathbf{I}$ is the $N_i^{BI} \times N_i^{BI}$ identity matrix. Substituting (6.44) into (6.31) yields reduced FE-BI matrices $\tilde{\mathbf{Z}}_{ij}^{FE-BI}$

$$\tilde{\mathbf{Z}}_{ij}^{FE-BI} = \left[\mathbf{P}_{ij} \cdot \mathbf{G}_j + \mathbf{Q}_{ij} \right] \ \ \{i,j\} \in \left\{1,...,N_{FE-BI}\right\}. \tag{6.46}$$

Here $\mathbf{G}_j = -\mathbf{Q}_j^H \cdot \mathbf{A}_j^{-1} \cdot \begin{bmatrix} \mathbf{0} & \mathbf{B}_j \end{bmatrix}^T$ is the compact notation of the operation relating $\mathbf{M}_i$ to $\mathbf{J}_i$. Finally the global system (6.23) can be reformulated as a $\tilde{N}^{tot} \times \tilde{N}^{tot}$ matrix equation in $\mathbf{J}$ and $\mathbf{D}$ as

$$\begin{bmatrix} \tilde{\mathbf{Z}}^{FE-BI,FE-BI} & \mathbf{Z}^{FE-BI,VIE} \\ \mathbf{Z}^{VIE,FE-BI} & \mathbf{Z}^{VIE,VIE} \end{bmatrix} \cdot \begin{bmatrix} \mathbf{J} \\ \mathbf{I}^{VIE} \end{bmatrix} = \begin{bmatrix} \mathbf{V}^{BI} \\ \mathbf{V}^{VIE} \end{bmatrix}. \tag{6.47}$$

where

$$\tilde{N}^{tot} = \sum_{i=1}^{N^{FE-BI}} N_i^{BI} + \sum_{i=N^{FE-BI}+1}^{N} N_i^{VIE}. \tag{6.48}$$

6.4 Numerical Results

This section presents numerical results that validate the proposed FE-BI-VIE solver. First, non-accelerated DD-FE-BI solver is used to analyze EM scattering from a dielectric sphere, and the results are compared to those obtained using exact analytical methods, i.e. Mie series solutions. Next, a 27 cube dielectric structure is considered. RCS results are obtained using AIM-FGG accelerated DD-FE-BI solver, and the results are compared to those obtained using an AIM-FGG accelerated PMCHWT based SIE solver. Finally, AIM-FGG accelerated DD-FE-BI is used to analyze scattering from a composite structure comprising dielectric and PEC cubes and the results are compared to those obtained using a AIM-FGG accelerated PMCHWT-EFIE based SIE solver. In the examples mesh density is represented by average edge length of the tetrahedral elements δ_s, which also corresponds to the average edge length of the triangular elements discretizing the domain boundaries. Average edge length for the hexahedral elements used to discretize domains modeled by VIE solver is denoted by δ_v. Proposed solver is implemented using the message passing interface (MPI) programming model, and executed on clusters of processors to reduce the computational requirements per processor. A transpose free quasi minimal residual (TFQMR) iterative scheme [55] is used to solve the hybrid DD-FE-BI-VIE matrix equations. Unless otherwise stated the tolerance of TFQMR is set to 10^{-6} and N_{iter} represents number of iterations required to reach this tolerance in the examples. All simulations are carried out on a cluster of dual-core 2.8 GHz AMD Opteron 2220 SE processors at the Center for Advanced Computing, University of Michigan.

6.4.1 Dielectric Sphere

The first test geometry is a dielectric sphere of radius $0.5\,\text{m}$, with relative permittivity $\varepsilon_r = 2.5$ which is embedded in a free-space cube of edge length $1.0\,\text{m}$,

which is decomposed into eight domains (Fig. 6.1(b)). Sphere surface is modeled by a staircase approximated as shown in Fig. 6.1(c). An incident plane wave

$$\mathbf{E}^i = \hat{\mathbf{p}} e^{-jk_0 \hat{\mathbf{k}} \mathbf{r}}, \tag{6.49}$$

with $\hat{\mathbf{p}} = \hat{\mathbf{x}}$ and $\hat{\mathbf{k}} = \hat{\mathbf{z}}$, at frequency $f = 300$ MHz is illuminating the sphere. The proposed DD-FE-BI (non-accelerated) solver with parameter $\alpha = 0.4$ is used to compute the RCS of the sphere and the results are compared to the Mie series solution. In the simulation average edge length, number of unknowns, and number of iterations are $\delta_s = 0.05$ m, $\tilde{N}^{tot} = 14,400$, and $N_{iter} = 355$, respectively. Fig. 6.1 (a) shows the bistatic RCS of the sphere in E-plane ($\phi = 0°$) and H-plane ($\phi = 90°$).

6.4.2 Composite Dielectric/PEC Structure

Next, a composite structure comprising dielectric and PEC regions is considered. The structure is decomposed into six cubical (and conforming) domains as shown in Fig. 6.2 (a). Two of these domains are dielectric with relative permittivity $\varepsilon_r = 2.5 - j0.5$. These cubes are residing between three free-space cubes ($\varepsilon_r = 1$), and a PEC cube at the end. An incident plane-wave with $\hat{\mathbf{p}} = \hat{\mathbf{x}}$ and $\hat{\mathbf{k}} = \hat{\mathbf{z}}$, at frequency $f = 300$ MHz is illuminating the structure. EM scattering from the structure is analyzed using an AIM-FGG accelerated DD-FE-BI solver with $\alpha = 0.4$. In this simulation $\delta_s = 0.05$ m, $\tilde{N}^{tot} = 43,200$, and $N_{iter} = 1315$. To obtain a reference solution a second simulation is performed using an AIM-FGG accelerated PMCHWT-EFIE based SIE solver. This time, an equivalent structure shown in Fig. 6.2(b) is considered. The free space cubes are removed from the model and the remaining structure is excited with the same incident plane-wave. In the second simulation $N = 36,000$, and $N_{iter} = 463$. In both simulations AIM grid size $\Delta x = \Delta y = \Delta z = 0.05$ m and mapping parameter $\mathcal{M} = 4$, and AIM near-field region comprises a sphere of radius of $\lambda_0/4$. Bistatic RCS of these structures is

computed and the results are compared in E-plane ($\phi = 0°$) and H-plane ($\phi = 90°$) as depicted in Fig. 6.3 (a) and (b).

6.4.3 Dielectric Cube Array

Next, EM scattering from a $3\times3\times3$ array of dielectric cubes is analyzed using the AIM-FGG accelerated DD-FE-BI solver with $\alpha = 0.4.$. Each cube is homogeneous with relative permittivity $\varepsilon_{ri} = 2.5 + (1.0 - j0.5)(i-1)/26,\ i = 1,...,27.$ The array is illuminated by a $\hat{\mathbf{p}} = \hat{\mathbf{x}}$ polarized plane wave propagating in $\hat{\mathbf{k}} = \hat{\mathbf{z}}$ direction at frequency $f =$ 300 MHz. Another simulation is performed using an AIM-FGG accelerated PMCHWT based SIE solver [26] to obtain a second set of results that serve as a reference. In the first simulation $\tilde{N}^{tot} = 194,400$ and $N_{iter} = 1,603$, whereas in the second simulation $N = 388,800,$ and $N_{iter} = 574.$ In both simulations $\delta_s = 0.05$ m, AIM grid size $\Delta x = \Delta y = \Delta z = 0.05,$ mapping parameter $\mathcal{M} = 6,$ and AIM near-field region comprises a sphere of radius of $0.3\lambda_0.$ Bistatic RCS of the structure is computed and the results in E-plane ($\phi = 0°$) and H-plane ($\phi = 90°$) are compared in Fig. 6.4 (b) and (c).

6.4.4 Homogeneous Dielectric Cubes

Finally, EM scattering from a structure comprising two dielectric cubes is analyzed using the AIM-FGG accelerated hybrid DD-FE-BI-VIE solver with $\alpha = 0.4.$ Each cube is homogeneous with relative permittivity $\varepsilon_r = 2.0.$ The geometry is decomposed into nine domains. The first cube is modeled as a single domain handled with the VIE solver, whereas the second cube is decomposed into eight identical domains handled with the DD-FE-BI solver as shown in Fig. 6.5(a). The structure is illuminated by a $\hat{\mathbf{p}} = \hat{\mathbf{x}}$ polarized plane wave propagating in $\hat{\mathbf{k}} = \hat{\mathbf{z}}$ direction at frequency $f =$ 300 MHz. Another simulation is performed using a pure VIE solver to obtain results that serve as a reference. In the first simulation $\delta_s = \delta_v = 0.1$ m, $\tilde{N}^{tot} = 39,600,$ and $N_{iter} = 1,361,$

whereas in the second simulation $N = 50,400,$ and $N_{iter} = 63.$ AIM grid size $\Delta x = \Delta y = \Delta z = 0.083,$ mapping parameter $\mathcal{M} = 6,$ and AIM near-field region comprises a sphere of radius of $0.5\lambda_0.$ Bistatic RCS of the structure is computed and the results in E-plane ($\phi = 0°$) and H-plane ($\phi = 90°$) are compared in Fig. 6.5 (b) and (c).

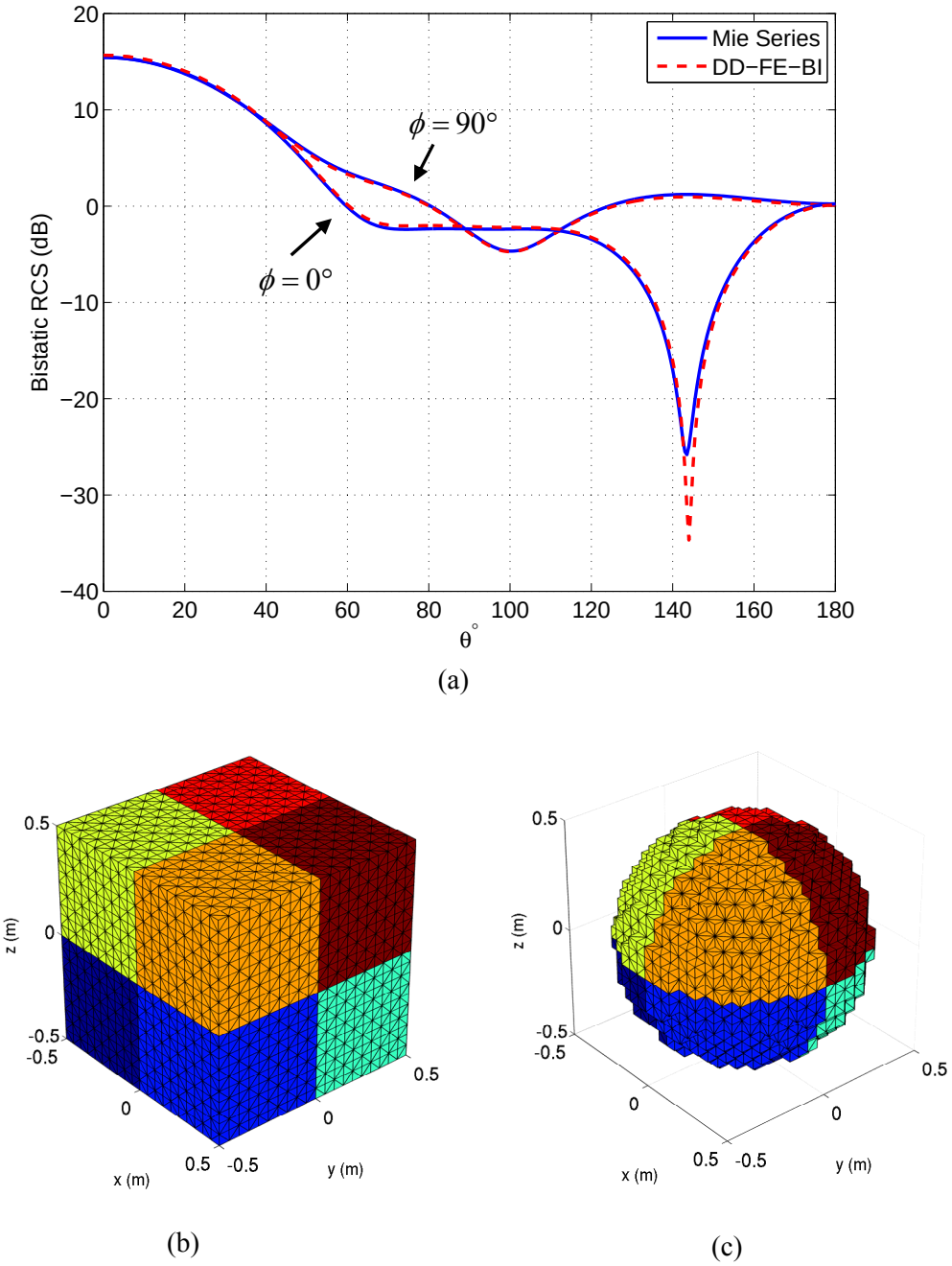

Figure 6.2: (a) Bistatic RCS of a dielectric sphere of radius 0.5 m and relative permittivity $\varepsilon_r = 2.5$. (b) Cubic 8 domain mesh. (c) Stair case approximation to the sphere embedded in (b).

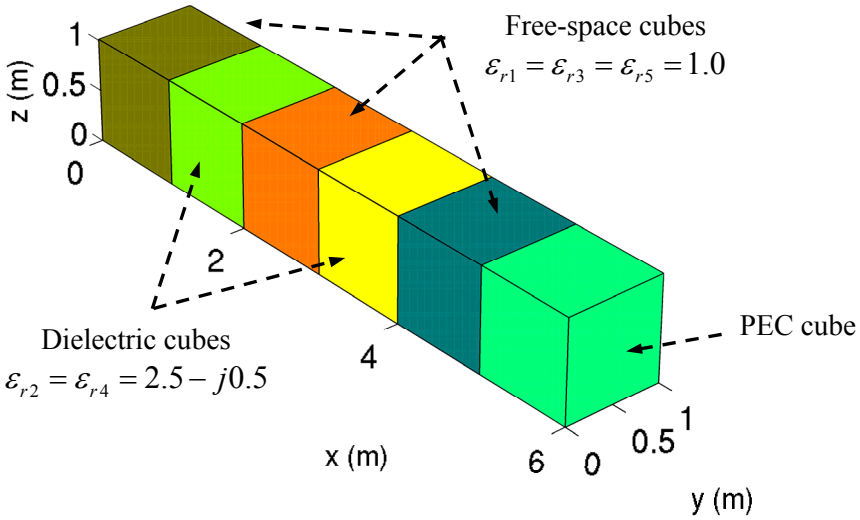

(a)

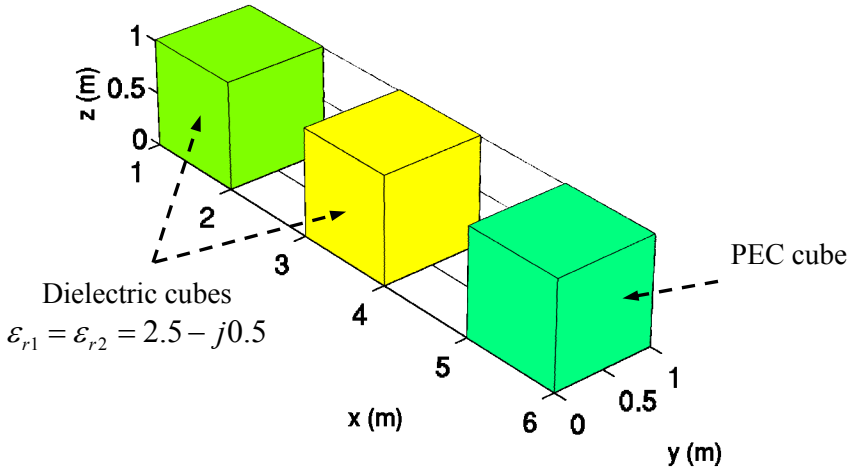

(b)

Figure 6.3: Two equivalent structures. (a) Six cube structure with two dielectric cubes, one PEC cube, and three free-space (dielectric) cubes. This structure is analyzed with an AIM-FGG accelerated FE-BI solver. (b) Three cube structure. Equivalent to since only the free-space cubes are removed. This structure is analyzed with an AIM-FGG accelerated PMCHWT based SIE solver.

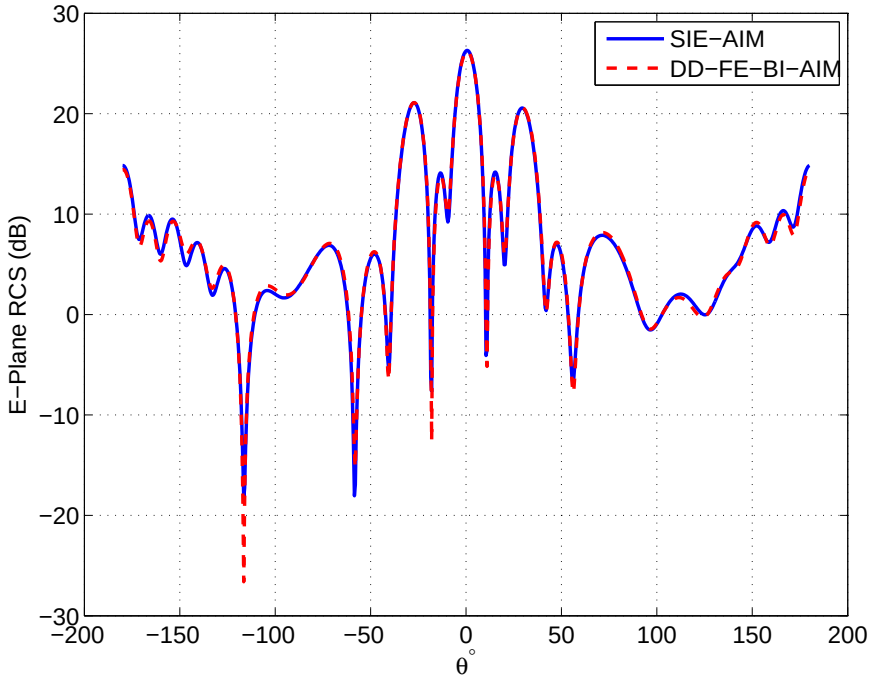

(a)

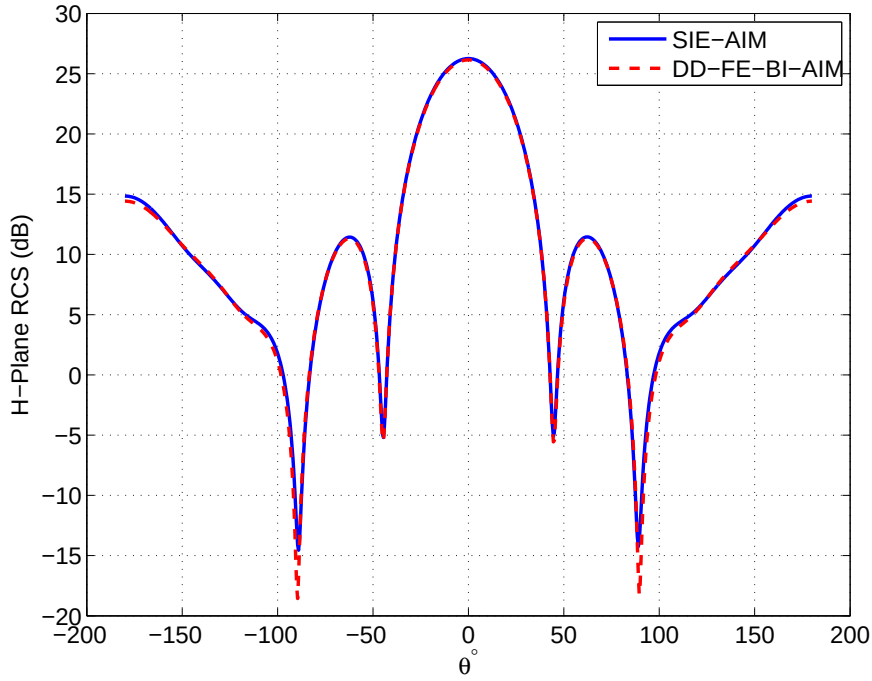

(b)

Figure 6.4: Bistatic RCS of the structure shown in Fig. 6.2 in (a) E- and (b) H- planes.

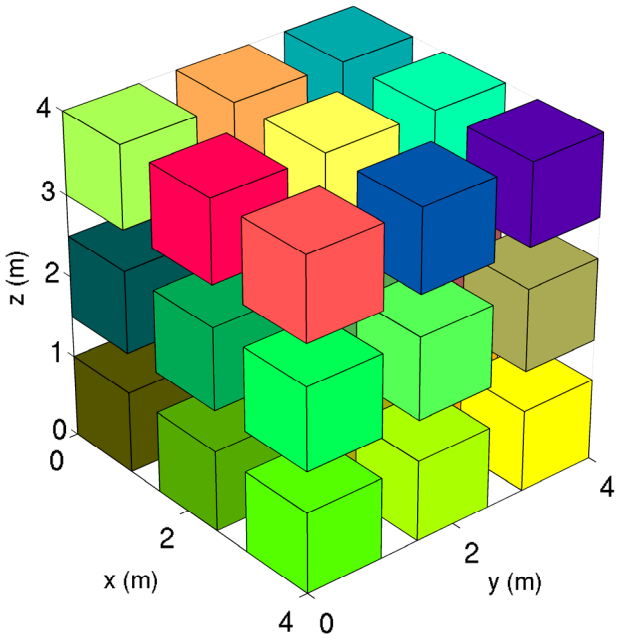
z (m)
x (m)
y (m)
0
1
2
3
4

(a)

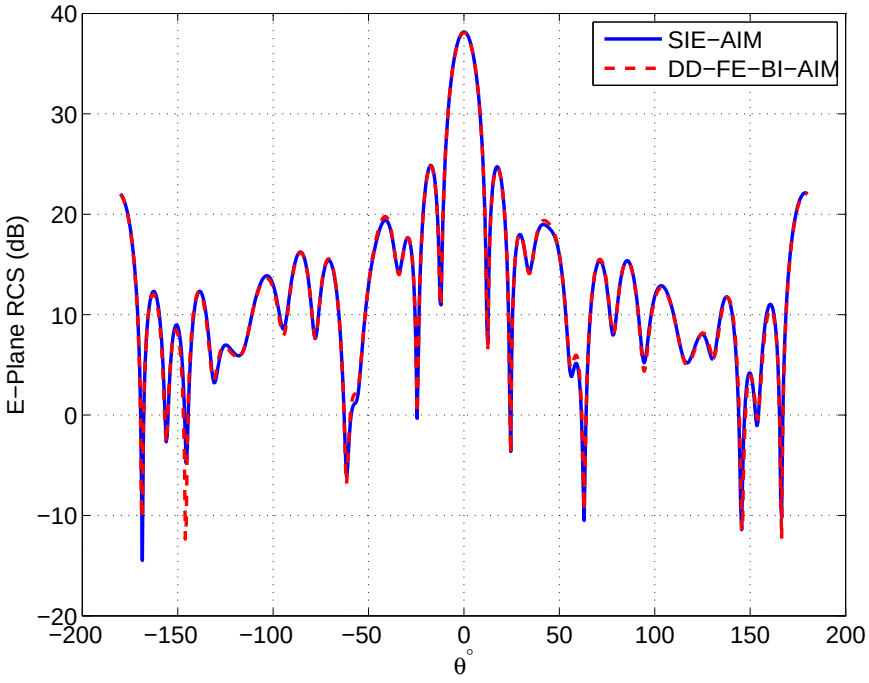
SIE−AIM
DD−FE−BI−AIM
E−Plane RCS (dB)
θ°
40
30
20
10
0
−10
−20
−200
−150
−100
−50
0
50
100
150
200

(b)

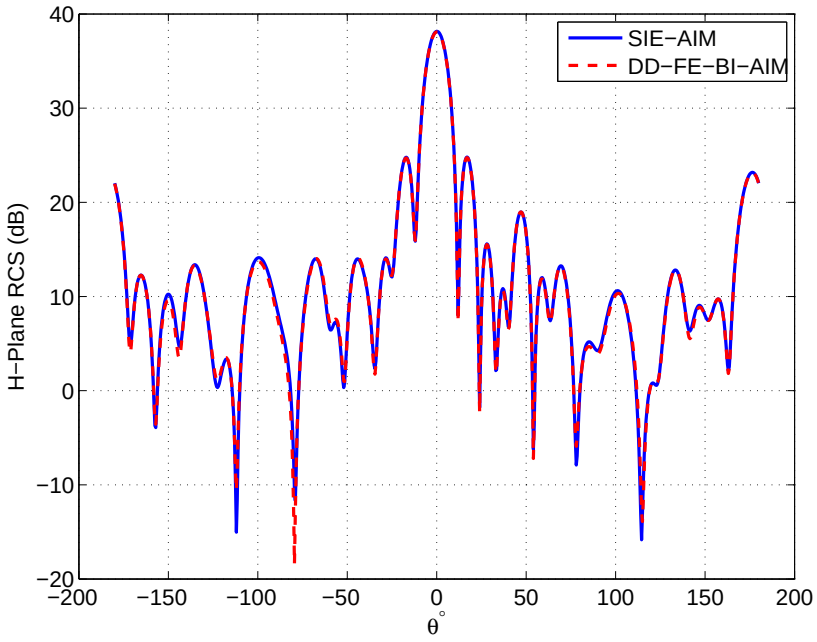

(c)

Figure 6.5: (a) 27 cube structure. Each cube is homogeneous, and the relative permittivity of the cubes is changing linearly from $\varepsilon_{r1} = 2.5$ to $\varepsilon_{r27} = 3.5 - j0.5$. Bistatic RCS of the structure shown in (b) E- and (c) H- planes.

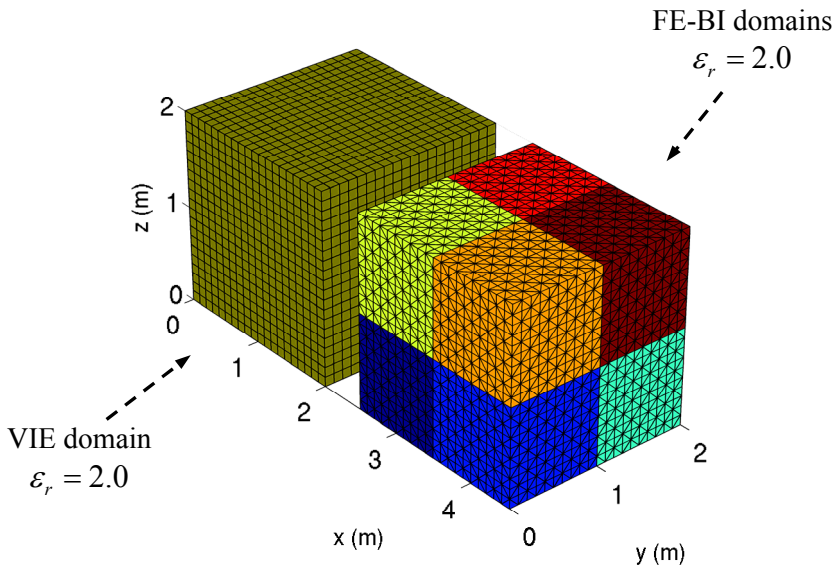

(a)

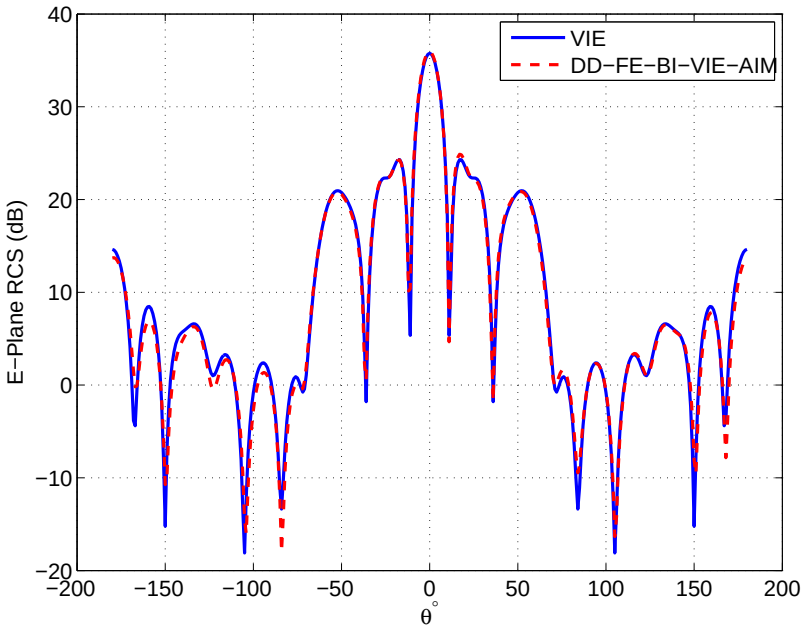

(b)

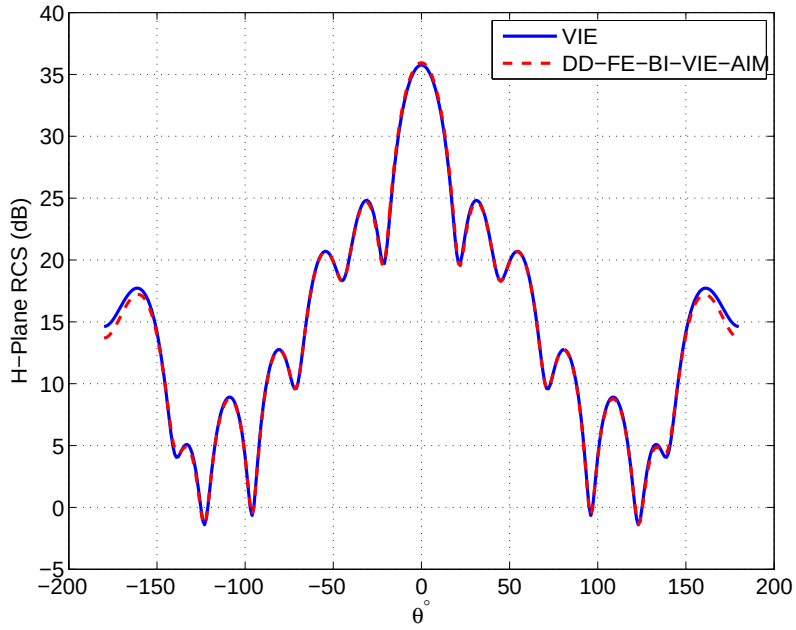

(c)

Figure 6.6: (a) A structure comprising two homogeneous dielectric cubes with $\varepsilon_r = 2.0$. First cube is handled with VIE solver, while the second one is decomposed into eight domains and handled with DD-FE-BI solver. Bistatic RCS of the structure shown in (b) E- and (c) H- planes.

CHAPTER 7
Conclusions and Future Work

7.1 Summary

A high order SIE solver is developed for the analysis of EM wave interactions with piecewise homogeneous composite dielectric and PEC structures with arbitrary surface junctions. In this solver curvilinear triangular elements and GWP basis functions are used to discretize the surfaces and expand the currents. To our knowledge a high order solver capable of simulating structures with arbitrary dielectric-PEC junctions has not been presented before, this work fills this gap in the literature.

A memory efficient extension to AIM that incorporates FGG, a fast and memory-efficient NUFFT algorithm to map surface sources onto an AIM grid, is developed. Established AIM mapping techniques, e.g. moment and far-field matching methods require pre-computing and storing M^3 coefficients for each actual source. The proposed method, in contrast, requires computing and storing only 4 exponential coefficients per source. Furthermore, after these coefficients have been computed, mapping each source using the FGG requires the same number of multiplications and additions as the established methods. Hence, without increase in CPU-time, the proposed method dramatically reduces the memory requirements of the AIM. The numerical results show that the method realizes significant memory savings but is not as accurate as MM. AIM-

FGG is successfully applied to a high order SIE solver for piecewise homogeneous, composite dielectric and PEC structures; a zeroth order DD-FE-BI solver for arbitrarily inhomogeneous, composite dielectric and PEC structures; and a VIE solver for arbitrarily inhomogeneous dielectric structures. Furthermore it is applied to a hybrid, DD-FE-BI-VIE solver combining all the aforementioned solvers. The accuracy and efficiency of the implementation is validated via various numerical examples.

An AIM-FGG accelerated DD-FE-BI-VIE solver is developed for the EM analysis of plasma engulfed re-entry vehicles. To this end, AIM-FGG accelerated FE-BI and VIE solvers are developed and validated independently. Then, FE-BI method is further improved with a DD technique. Numerical results that serve to validate the accuracy and demonstrate the efficiency of these solvers are presented in Chapter 4, 5, and 6. Finally, these solvers are combined in a hybrid DD-FE-BI-VIE solver. A preliminary result is validating the accuracy of this solver is presented in Chapter 6. The proposed hybrid solver exhibits unprecedented modeling flexibility for the solution of EM scattering and radiation from complex real life problems.

	Level of dielectric inhomogeneity	Composite metallic-dielectric	Multi-scale structures	Scalability with respect to N
High order SIE	*	***	*	**
VIE	**	-	*	***
DD-FE-BI	***	**	***	***
DD-FE-BI-VIE	****	**	***	***

Table 7.1: Computational performances of the solvers for different types of structures. The greater number of *'s represents a better grade. Each solver is assumed to be accelerated with AIM-FGG. N represents the total number of independent unknowns for each solver.

The computational performances of the aforementioned solvers for different type of structures are summarized in Table 7.1. All solvers are assumed to be accelerated with AIM-FGG and the specific formulations presented in this thesis are considered. High order SIE solver is suitable for piece-wise homogeneous composite structures with arbitrary metal-dielectric junctions. As the level of inhomogeneity increases the efficiency of this solver decreases. SIE solver has a superior ability to handle arbitrarily shaped open or closed PEC structures compare to other solvers. However convergence problems arise for structures having sub-wavelengths features and large scale features at the same time (multi-scale). VIE solver can handle inhomogeneous dielectric structures better it can not model PEC structures. Similar to the SIE solver, multi-scale structures can be problematic for the VIE solver. On the other hand, DD-FE-BI solver provides greater overall flexibility in modeling inhomogeneous and even multi-scale composite structures. However it is less accurate compared to the SIE and VIE solvers. DD-FE-BI-VIE hybrid solver takes advantage of the modeling flexibility of the DD-FE-BI and the accuracy of the VIE solvers to overcome this problem.

The first column in Table 7.1 ranks the solvers considering their computational efficiency and accuracy when simulating dielectric-only structures with different levels of inhomogeneity. The number of * in this column represent the level inhomogeneity in the structure. If the medium is piecewise homogeneous SIE must be the solver of choice since it requires only the discretization of the surfaces which will yield smaller number of unknowns compared to volumetric discretizations other solvers require. VIE and DD-FE-BI solvers can handle higher inhomogeneity, although DD-FE-BI offers less accuracy compared to VIE. The hybrid DD-FE-BI-VIE solver takes advantage of both solvers, thus earning four *'s. The second column in Table 7.1 ranks the solvers for their ability to model composite structures. SIE solver can model open and closed PEC surfaces with arbitrary junctions earning the most *'s. VIE solver can not model PEC structures. DD-

FE-BI (also DD-FE-BI-VIE) can model closed PEC structures but open PEC surfaces and junctions are not supported. Although the method can be modified to cover these structures, they are not included in the current implementation. The third column represents the performances of the solvers for multi-scale structures. SIE and VIE solvers suffer from the aforementioned convergence and computational efficiency problems for these types of structures. DD-FE-BI (also DD-FE-BI-VIE) solver overcomes these problems with DD strategy. The final column in Table 7.1 ranks the solvers for their computational efficiency when simulating bigger structures (increasing number of unknowns). All solvers have a CPU time and memory complexity of $O(N \log N)$ and $O(N)$, respectively. However, there is one exception: When SIE solvers are used for surface scatterers CPU time and memory scale as $O(N^{1.5} \log N)$ and $O(N^{1.5})$. Therefore SIE solver has two *'s in this category.

Part of the work presented in this thesis is published in [20, 26, and 80].

7.2 Future Work

In the current implementation, zeroth order volume/surface elements and field/current basis functions are used in the discretization of PDEs and IEs in the AIM-FGG accelerated FE-BI solver. The accuracy and the efficiency of this solver will benefit from high-order volume/surface discretizations and field/current expansions. GWP basis functions defined on curvilinear elements can be combined with high order FE basis functions defined on tetrahedral elements to achieve this efficiency. Improvements in this direction are under consideration.

The FE-BI solver presented in this thesis is susceptible to convergence problems in the iterative solution of system BI portion of the system when surface meshes include sub-wavelength features. These types of meshes lead to ill-conditioned system matrices,

i.e. system matrices with high condition numbers, for IE solvers. This issue is investigated extensively in the literature. One of the popular techniques to remedy this problem is to use Calderon pre-conditioners [82, 83]. The AIM-FGG accelerated DD-FE-BI solver presented in this thesis can benefit from Calderon pre-conditioners. Improvements to this end are also under consideration.

BIBLIOGRAPHY

[1] R. F. Harrington, *Field Computation by Moment Methods*: Oxford University Press, USA, 1993.

[2] R. Mittra, *Computer techniques for electromagnetics*: Hemisphere Pub. Corp., 1987.

[3] N. Morita, N. Kumagai, and J. R. Mautz, *Integral Equation Methods for Electromagnetics*: Artech House, 1990.

[4] J. J. H. Wang, *Generalized moment methods in electromagnetics: formulation and computer solution of integral equations*: J. Wiley, 1991.

[5] E. K. Miller, "A selective survey of computational electromagnetics," *IEEE Trans. Antennas Propagat.,* vol. 36, pp. 1281-1305, Sept. 1988.

[6] K. Umashankar and A. Taflove, *Computational electromagnetics*: Artech House, 1993.

[7] A. F. Peterson, S. L. Ray, and R. Mittra, *Computational Methods for Electromagnetics* New York: Wiley-IEEE Press 1997.

[8] J. M. Jin, *The finite element method in electromagnetics*: Wiley, 2002.

[9] J. M. Jin, *Theory and Computation of Electromagnetic Fields*: John Wiley & Sons.

[10] J. L. Volakis, A. Chatterjee, and L. C. Kempel, *Finite element method for electromagnetics: antennas, microwave circuits, and scattering applications*: IEEE Press, 1998.

[11] W. C. Chew, J. M. Jin, C. C. Lu, E. Michielssen, and J. M. Song, "Fast solution methods in electromagnetics," *IEEE Trans. Antennas Propagat.,* vol. 45, pp. 533-543, Mar. 1997.

[12] R. F. Harrington, *Time-harmonic electromagnetic fields*: IEEE Press, 1961.

[13] J. M. Song and W. C. Chew, "Multilevel fast-multipole algorithm for solving combined field integral equations of electromagnetic scattering," *Microwave Opt. Tech. Lett.,* vol. 10, pp. 14-19, Sep. 1995.

[14] K. Sertel and J. L. Volakis, "Multilevel fast multipole method solution of volume integral equations using parametric geometry modeling," *Antennas and Propagation, IEEE Transactions on,* vol. 52, pp. 1686-1692, 2004.

[15] M. F. Catedra, R. F. Torres, J. Basterrechea, and E. Gago, *The CG-FFT Method: Application of Signal Processing Techniques to Electromagnetics*. Norwood, MA: Artech House, 1995.

[16] J. R. Phillips and J. K. White, "A precorrected-FFT method for electrostatic analysis of complicated 3-D structures," *IEEE Trans. Computer-Aided Design,* vol. 16, pp. 1059-1072, Oct. 1997.

[17] E. Bleszynski, M. Bleszynski, and T. Jaroszewic, "AIM: Adaptive integral method for solving large-scale electromagnetic scattering and radiation problems," *Radio Sci.,* vol. 31, pp. 1225-151, Sept./Oct. 1996.

[18] C. F. Wang, F. Ling, J. Song, and J. M. Jin, "Adaptive integral solution of combined field integral equation," *Microwave Opt. Tech. Lett.,* vol. 19, pp. 321-328, 1998.

[19] Z. Zhong Qing and L. Qing Huo, "A volume adaptive integral method (VAIM) for 3-D inhomogeneous objects," *Antennas and Wireless Propagation Letters, IEEE,* vol. 1, pp. 102-105, 2002.

[20] O. Bakir, H. Bagci, and E. Michielssen, "Adaptive integral method with fast Gaussian gridding for solving combined field integral equations," *Waves in Random and Complex Media,* vol. 19, pp. 147 - 161, 2009.

[21] J.-Y. Lee and L. Greengard, "The type 3 nonuniform FFT and its applications," *J. Comput. Phys.,* vol. 206, pp. 1-5, 2005.

[22] L. Greengard and J.-Y. Lee, "Accelerating the Nonuniform Fast Fourier Transform," *SIAM Review,* vol. 46, pp. 443-454, 2004.

[23] B. M. Notaros, "Higher Order Frequency-Domain Computational Electromagnetics," *Antennas and Propagation, IEEE Transactions on,* vol. 56, pp. 2251-2276, 2008.

[24] K. A. C. Donepudi, J. M. Jin, and W. C. Chew, "A higher order multilevel fast multipole algorithm for scattering from mixed conducting/dielectric bodies," *IEEE Trans. Antennas Propagat.,* vol. 51, pp. 2814-2821, 2003.

[25] O. S. Kim and P. Meincke, "Adaptive integral method for higher order method of moments," *IEEE Trans. Antennas Propagat.,* vol. 56, pp. 2298-2305, 2008.

[26] O. Bakir, H. Bagci, and E. Michielssen, "A high-order fast Gaussian gridding AIM solver for composite structures," in *Antennas and Propagation Society International Symposium, 2009. APSURSI '09. IEEE*, 2009, pp. 1-4.

[27] G. E. Antilla and N. G. Alexopoulos, "Scattering from complex three-dimensional geometries by a curvilinear hybrid finite-element-integral equation approach," *J. Opt. Soc. Am. A,* vol. 11, pp. 1445-1457, 1994.

[28] J. L. Volakis, T. Ozdemir, and J. Gong, "Hybrid finite-element methodologies for antennas and scattering," *Antennas and Propagation, IEEE Transactions on,* vol. 45, pp. 493-507, 1997.

[29] S. Xin-Qing, J. Jian-Ming, S. Jiming, L. Cai-Cheng, and C. Weng Cho, "On the formulation of hybrid finite-element and boundary-integral methods for 3-D scattering," *Antennas and Propagation, IEEE Transactions on,* vol. 46, pp. 303-311, 1998.

[30] M. N. Vouvakis, L. Seung-Cheol, Z. Kezhong, and L. Jin-Fa, "A symmetric FEM-IE formulation with a single-level IE-QR algorithm for solving electromagnetic radiation and scattering problems," *Antennas and Propagation, IEEE Transactions on,* vol. 52, pp. 3060-3070, 2004.

[31] M. M. Ilic, M. Djordjevic, A. Z. Ilic, and B. M. Notaros, "Higher Order Hybrid FEM-MoM Technique for Analysis of Antennas and Scatterers," *Antennas and Propagation, IEEE Transactions on,* vol. 57, pp. 1452-1460, 2009.

[32] T. F. Eibert and J. L. Volakis, "Adaptive integral method for hybrid FE/BI modelling of 3-D doubly periodic structures," *IEE Proceedings - Microwaves, Antennas and Propagation,* vol. 146, pp. 17-22, 1999.

[33] P. Zhen and S. Xin-Qing, "A Flexible and Efficient Higher Order FE-BI-MLFMA for Scattering by a Large Body With Deep Cavities," *Antennas and Propagation, IEEE Transactions on,* vol. 56, pp. 2031-2042, 2008.

[34] L. Yujia and J. Jian-Ming, "A Vector Dual-Primal Finite Element Tearing and Interconnecting Method for Solving 3-D Large-Scale Electromagnetic Problems," *Antennas and Propagation, IEEE Transactions on,* vol. 54, pp. 3000-3009, 2006.

[35] L. Zhi-Qing, A. Xiang, and H. Wei, "A Fast Domain Decomposition Method for Solving Three-Dimensional Large-Scale Electromagnetic Problems," *Antennas and Propagation, IEEE Transactions on,* vol. 56, pp. 2200-2210, 2008.

[36] M. N. Vouvakis, Z. Cendes, and L. Jin-Fa, "A FEM domain decomposition method for photonic and electromagnetic band gap structures," *Antennas and Propagation, IEEE Transactions on,* vol. 54, pp. 721-733, 2006.

[37] C. T. Wolfe and S. D. Gedney, "Implementation of a Domain Decomposition Method on a High Performance Parallel Platform for the Solution of Large Electromagnetic Problems," *Electromagnetics,* vol. 27, pp. 399 - 411, 2007.

[38] S.-C. Lee, M. N. Vouvakis, and J.-F. Lee, "A non-overlapping domain decomposition method with non-matching grids for modeling large finite antenna arrays," *Journal of Computational Physics,* vol. 203, pp. 1-21, 2005.

[39] Z. Kezhong, V. Rawat, and L. Jin-Fa, "A Domain Decomposition Method for Electromagnetic Radiation and Scattering Analysis of Multi-Target Problems," *Antennas and Propagation, IEEE Transactions on,* vol. 56, pp. 2211-2221, 2008.

[40] V. Marinos, Z. Kezhong, S. Seung-Mo, and L. Jin-Fa, "A domain decomposition approach for non-conformal couplings between finite and boundary elements for unbounded electromagnetic problems in R3," *J. Comput. Phys.,* vol. 225, pp. 975-994, 2007.

[41] L. Mao-Kun and C. Weng Cho, "Multiscale Simulation of Complex Structures Using Equivalence Principle Algorithm With High-Order Field Point Sampling Scheme," *Antennas and Propagation, IEEE Transactions on,* vol. 56, pp. 2389-2397, 2008.

[42] A. M. van de Water, B. P. de Hon, M. C. van Beurden, A. G. Tijhuis, and P. de Maagt, "Linear embedding via Green's operators: A modeling technique for finite

electromagnetic band-gap structures," *Physical Review E,* vol. 72, p. 056704, 2005.

[43] M.-K. Li, W. C. Chew, and L. J. Jiang, "A domain decomposition scheme based on equivalence theorem," *Microwave and Optical Technology Letters,* vol. 48, pp. 1853-1857, 2006.

[44] M. K. Li and W. C. Chew, "Wave-Field Interaction With Complex Structures Using Equivalence Principle Algorithm," *Antennas and Propagation, IEEE Transactions on,* vol. 55, pp. 130-138, 2007.

[45] D. D. Morabito, "The Spacecraft Communications Blackout Problem Encountered during Passage or Entry of Planetary Atmospheres," IPN Progress Report, August 2002.

[46] T. H. Stix, *The theory of plasma waves*: McCraw-Hill, 1962.

[47] M. D. White, "Simulation of communications through a weakly ionized plasma for a re-entry vehicle at Mach 23.9," in *Antennas and Propagation Society International Symposium, 2005 IEEE*, 2005, pp. 418-421 vol. 4B.

[48] C. Vecchi, M. Sabbadini, R. Maggiora, and A. Siciliano, "Modelling of antenna radiation pattern of a re-entry vehicle in presence of plasma," in *Antennas and Propagation Society International Symposium, 2004. IEEE*, 2004, pp. 181-184 Vol.1.

[49] R. D. Graglia, D. R. Wilton, and A. F. Peterson, "Higher order interpolatory vector bases for computational electromagnetics," *IEEE Trans. Antennas Propagat.,* vol. 45, pp. 329-342, Mar. 1997.

[50] P. Yla-Oijala, M. Taskinen, and J. Sarvas, "Surface integral equation method for general composite metallic and dielectric structures with junctions," *Progress in Electromagnetics Research-Pier,* vol. 52, pp. 81-108, 2005.

[51] M. Carr, E. Topsakal, and J. L. Volakis, "A procedure for modeling material junctions in 3-D surface integral equation approaches," *IEEE Transactions on Antennas and Propagation,* vol. 52, pp. 1374-1379, 2004.

[52] J. R. Mautz and R. F. Harrington, "Electromagnetic scattering from a homogeneous material body of revolution," *AEU,* vol. 33, pp. 71-80, 1979.

[53] A. F. Peterson, *Mapped Vector Basis Functions for Electromagnetic Integral Equations*: Morgan & Claypool Publishers, 2006.

[54] S. M. Rao, D. R. Wilton, and A. W. Glisson, "Electromagnetic scattering by surfaces of arbitrary shape," *IEEE Trans. Antennas Propagat.,* vol. 30, pp. 409-418, May 1982.

[55] R. W. Freund, "A transpose-free quasi-minimal residual algorithm for non-hermitian linear systems," *SIAM J. Sci. Stat. Comput.,* vol. 14, pp. 470-482, Mar. 1993.

[56] F. Ling, C. F. Wang, and J. M. Jin, "Application of Adaptive Integral Method to Scattering and Radiation Analysis of Arbitrarily Shaped Planar Structures," *J. Electromagn. Waves Appl.,* vol. 12, pp. 1021-1037, 1998.

[57] G.-X. Fan and Q. H. Liu, "The CGFFT method with a discontinuous FFT algorithm," *Microwave Opt. Tech. Lett.,* vol. 29, pp. 47-49, 2001.

[58] B. J. Fasenfest, F. Capolino, D. R. Wilton, D. R. Jackson, and N. J. Champagne, "A fast MoM solution for large arrays: Green's function interpolation with FFT," *IEEE Antennas Wireless Propagat. Lett.,* vol. 3, pp. 161-164, 2004.

[59] S. Gedney, A. Zhu, W.-H. Tang, G. Liu, and P. Petre, "A fast, high-order quadrature sampled pre-corrected fast-Fourier transform for electromagnetic scattering," *Microwave Opt. Tech. Lett.,* vol. 36, pp. 343-349, 2003.

[60] S. M. Seo and J.-F. Lee, "A fast IE-FFT algorithm for solving PEC scattering problems," *IEEE Trans. Magnetics,* vol. 41, pp. 1476-1479, 2005.

[61] A. Dutt and V. Rokhlin, "Fast Fourier transforms for nonequispaced data," *SIAM J. Sci. Comput.,* vol. 14, pp. 1368-1393, 1993.

[62] G. Beylkin, "On the Fast Fourier Transform of Functions with Singularities," *Applied and Computational Harmonic Analysis,* vol. 2, pp. 363-381, 1995.

[63] Q. H. Liu, X. M. Xu, B. Tian, and Z. Q. Zhang, "Applications of nonuniform fast transform algorithms in numerical solutions of differential and integral equations," *IEEE Trans. Geosci. Remote Sensing,* vol. 38, pp. 1551-1560, 2000.

[64] X. M. Xu and Q. H. Liu, "The conjugate-gradient nonuniform fast Fourier transform (CG-NUFFT) method for one- and two-dimensional media," *Microwave Opt. Tech. Lett.,* vol. 24, pp. 385-389, 2000.

[65] G. Beylkin, J. D. Gorman, S. Li-Fliss, and M. A. Ricoy, "SAR imaging and multiresolution analysis," *Proc. SPIE,* vol. 2487, pp. 144-152, 1995.

[66] S. Matej, J. A. Fessler, and I. G. Kazantsev, "Iterative tomographic image reconstruction using Fourier-based forward and back-projectors," *IEEE Trans. Medical Imaging,* vol. 23, pp. 401-412, 2004.

[67] J. I. Jackson, C. H. Meyer, D. G. Nishimura, and A. Macovski, "Selection of a convolution function for Fourier inversion using gridding [computerised tomography application]," *IEEE Trans. Medical Imaging,* vol. 10, pp. 473-478, 1991.

[68] J. Song, Q. H. Liu, P. Torrione, and L. Collins, "Two-dimensional and three-dimensional NUFFT migration method for landmine detection using ground-penetrating Radar," *IEEE Trans. Geosci. Remote Sensing,* vol. 44, pp. 1462-1469, 2006.

[69] X. C. Nie, L. W. Li, and N. Yuan, "Precorrected-FFT Algorithm for Solving Combined Field Integral Equations in Electromagnetic Scattering," *J. Electromagn. Waves Appl.,* vol. 16, pp. 1171-1187, 2002.

[70] A. J. W. Duijndam and M. A. Schonewille, "Nonuniform fast Fourier transform," *Geophysics,* vol. 64, pp. 539-551, 1999.

[71] A. C. Woo, H. T. G. Wang, M. J. Schuh, and M. L. Sanders, "EM programmer's notebook-benchmark radar targets for the validation of computational electromagnetics programs," *IEEE Antennas Propagat. Mag.,* vol. 35, pp. 84-89, 1993.

[72] T. Ando, J. Yamauchi, and H. Nakano, "Numerical analysis of a dielectric rod antenna - Demonstration of the discontinuity-radiation concept," *IEEE Trans. Antennas Propagat.,* vol. 51, pp. 2007-2013, 2003.

[73] L. Cai-Cheng, "A fast algorithm based on volume integral equation for analysis of arbitrarily shaped dielectric radomes," *Antennas and Propagation, IEEE Transactions on,* vol. 51, pp. 606-612, 2003.

[74] G. Jing-Li, L. Jian-Ying, and L. Qi-Zhong, "Analysis of arbitrarily shaped dielectric radomes using adaptive integral method based on volume integral

equation," *Antennas and Propagation, IEEE Transactions on,* vol. 54, pp. 1910-1916, 2006.

[75] P. Zwamborn and P. M. van den Berg, "The three dimensional weak form of the conjugate gradient FFT method for solving scattering problems," *Microwave Theory and Techniques, IEEE Transactions on,* vol. 40, pp. 1757-1766, 1992.

[76] H. Gan and W. C. Chew, "A discrete BCG-FFT algorithm for solving 3d inhomogeneous scatterer problems," *Journal of Electromagnetic Waves and Applications,* vol. 9, pp. 1339-1357, 1995.

[77] M. Frigo and S. G. Johnson, "FFTW: An adaptive software architecture for the FFT," in *IEEE ICASSP*, 1998, pp. pp.1381-1384.

[78] S. Xin-Qing and E. Kai-Ning Yung, "Implementation and experiments of a hybrid algorithm of the MLFMA-enhanced FE-BI method for open-region inhomogeneous electromagnetic problems," *Antennas and Propagation, IEEE Transactions on,* vol. 50, pp. 163-167, 2002.

[79] J. Song, L. Cai-Cheng, and C. Weng Cho, "Multilevel fast multipole algorithm for electromagnetic scattering by large complex objects," *IEEE Trans. Antennas Propagat.,* vol. 45, pp. 1488-1493, 1997.

[80] O. Bakir, H. Bagci, and E. Michielssen, "Adaptive integral method with fast Gaussian gridding," in *Antennas and Propagation Society International Symposium, 2008. AP-S 2008. IEEE*, 2008, pp. 1-4.

[81] J. De Zaeytijd, I. Bogaert, and A. Franchois, "An efficient hybrid MLFMA-FFT solver for the volume integral equation in case of sparse 3D inhomogeneous dielectric scatterers," *Journal of Computational Physics,* vol. 227, pp. 7052-7068, 2008.

[82] F. P. Andriulli, K. Cools, H. Bagci, F. Olyslager, A. Buffa, S. Christiansen, and E. Michielssen, "A Multiplicative Calderon Preconditioner for the Electric Field Integral Equation," *Antennas and Propagation, IEEE Transactions on,* vol. 56, pp. 2398-2412, 2008.

[83] P. Yla-Oijala, S. P. Kiminki, and S. Jarvenpaa, "Calderon Preconditioned Surface Integral Equations for Composite Objects With Junctions," *Antennas and Propagation, IEEE Transactions on,* vol. 59, pp. 546-554.